FLASH CALCINATION OF LIMESTONE IN A BENCH-SCALE SORBENT ACTIVATION PROCESS (SAP) UNIT

BY

IVAN SUGIYONO

THESIS

Submitted in partial fulfillment of the requirements
for the degree of Master of Science in Environmental Engineering in Civil Engineering
in the Graduate College of the
University of Illinois at Urbana-Champaign, 2012

Urbana, Illinois

Adviser:

Dr. Massoud Rostam-Abadi
Professor Mark J. Rood

ABSTRACT

Coal-fired power plants produce 40 % of the total electricity in the United States. The flue gas generated from burning coal contains air pollutants including sulfur oxides (SO_x), hydrochloric acid (HCl) and elemental and ionic mercury (Hg^o and Hg^{2+}). A process option to remove these pollutants from the flue gas is by injection of sorbents downstream of a boiler and up-stream of a particulate control device. Activated carbon (AC) is a suitable sorbent to capture vapor-phase mercury and calcium-based sorbents such as quicklime (CaO) and hydrated lime ($Ca(OH)_2$) are suitable sorbents to capture SO_x and HCl. This research addresses producing quicklime by a novel process to remove SO_x and HCl from flue gas streams. Quicklime is commercially prepared by thermal decomposition of limestone ($CaCO_3$) in a rotary kiln. The surface area of commercial quicklime, a key parameter of reactivity, is typically < 2 m^2/g. Therefore, increasing the surface area of quicklime in a cost-effective process would enhance its effectiveness as a sorbent for control of combustion-generated air pollutants.

Illinois State Geological Survey (ISGS), a division of the Prairie Research Institute at the University of Illinois at Urbana Champaign (UIUC), and Electric Power Research Institute (EPRI), Palo Alto, CA, have developed a patent-pending Sorbent Activation Process (SAP) technology for on-site production and direct injection of quicklime into flue gas generated by coal fired power plants (US Patent Application 20,110,223,088). This process is an extension of a similar patented process for on-site production of activated carbon (AC) to remove vapor-phase mercury emissions in the flue gas (US Patents 6, 451, 094 and 6,558,454). SAP utilizes an entrained-flow reactor in which sorbent (AC or quicklime) particles are subjected to a < 5 second residence time during their production. On-site production of quicklime could help lower the production cost of quicklime sorbent for dry sorbent injection (DSI) applications.

In this research, a bench-scale SAP unit (2 kg/hr limestone feed rate) was used to prepare quicklime from two limestone samples. The impacts of particle size, surface morphologies of limestone, and operating parameters of SAP including temperature profile, and residence time on the product quicklime were investigated. SAP experiments were designed to provide engineering data and guidelines for operating a pilot-scale (20 kg/hr limestone feed rate) and designing a full-scale SAP units (135 kg/hr limestone feed rate) currently being tested at a coal-fired power plant in the United States. Additionally, kinetic information about calcination of the two limestone

samples was obtained from the analysis of non-isothermal decomposition measured by thermogravimetric analysis (TGA) method. Furthermore, the kinetic information was used to predict limestone calcination in SAP.

Lime sorbents prepared in SAP contained between 20 and 80 wt % calcium oxide (balance calcium carbonate) and had surface areas ranging between 5 and 12 m^2/g depending on operation conditions employed. Non-isothermal TGA experiments were analyzed by several data analysis approaches including Coats-Redfern, Criado linearization and DTG-curve fitting method using DTG-SIM software to obtain the kinetic parameters (activation energy, frequency factor, and reaction order) for thermal decomposition (calcination) of the two limestone samples. The values of the kinetic parameters were in good agreement with those previously reported in the literature. The kinetic models predicted the experimental TGA calcination in N_2 with less than 10% deviation. However, only the Coats-Redfern-based kinetic model predicted the TGA calcinations in CO_2 data with less than 10 % deviation. The kinetic parameters were used to predict limestone conversions in an ideal flash calciner and in SAP. Ideal flash calciner assumed isothermal condition throughout the reactor while the later one used the actual temperature profiles in SAP to predict limestone conversion at different CO_2 partial pressures. The impact of mass and heat transfer limitation, lime sintering phenomenon, and particle size distribution of limestone/lime were not included in the model. The experimental limestone conversions were higher than those predicted by the models.

Based on the results from SAP experiments and model predictions, it was concluded that the actual temperature of limestone particle was likely much higher than the gas temperature measured in SAP. Future work should include: 1) installation of additional thermocouples to continuously monitor both axial and radial temperature profiles in the SAP, 2) an understanding of the flow pattern and hydrodynamic inside the SAP to better estimate gas-gas and gas-solid mixing, 3) testing several size-graded limestone samples to evaluate the impact of particle size on limestone calcination, 4) calibrating the propane and combustion air flow rates to obtain more accurate readings, 5) quantify the extent of particle deposition in SAP, 6) measure gas phase concentrations of CO, CO_2, O_2, NO_x, and hydrocarbons (HCs), and verify those measured values, and 7) incorporate mass and heat transports effects in the model to better predict calcination performance of limestone in bench-, pilot-, and full-scale SAPs.

To my parents, brother and friends whose support and prayers are simply never-ending.

ACKNOWLEDGEMENTS

I thank my advisors Dr. Massoud Rostam-Abadi and Dr. Mark J. Rood for providing guidance and support throughout my graduate study. All of the technical discussion and casual interaction with them have honed my technical and social skills. Their life-time advices will always be invaluable for my future endeavors.

I am truly privileged to be part of two amazing research groups, Advanced Energy Technology Initiative (AETI) and Air Quality Engineering and Sciences (AQES). Special thanks are reserved for Dr. Yonqi Lu, Dr. Seyed A. Dastgheib, Dr. Hong Lu, and David Ruhter whose opinions, recommendations, and helps have always been significant for my research. I am also grateful to all AQES research group members for providing friendship and insight. Their presence in the past two years has made my journey very enjoyable. Last but not least, I would like to thank my God, parents, brother, and friends for their never-ending encouragement, support, and faith on me which always keep me motivated and confident.

Characterization work, including SEM and some of the TGA, was performed at the Frederick Seitz Material Research Laboratory Central Facilities, University of Illinois, which are partially supported by the U.S. Department of Energy under grants DE-FG02-07ER46453 and DE-FG02-07ER46471.

This work is supported by grants from Electric Power Research Institute (EPRI C6220, C5150), University of Illinois at Urbana Champaign (D7355, D7155), and Illinois Clean Coal Institute (ICCI-A2322).

TABLE OF CONTENTS

LIST OF TABLES

LIST OF FIGURES

1 INTRODUCTION

1.1 Background

Limestone (calcium carbonate, $CaCO_3$) is an abundant natural resource and a low-cost material (US$ 10 – 20/ metric ton) for producing limes [Smith, 2001]. When heated, limestone will decompose and release its CO_2 content and this process is known as limestone calcination. The product of limestone calcination is mainly quicklime (CaO). However, depending on the relative humidity (RH) and temperature of the calcination gas the produced CaO can react with H_2O and form hydrated lime ($Ca(OH)_2$),. Both quicklime and hydrated lime are effective sorbents for capturing gaseous pollutants, such as sulfur oxides (SO_x including SO_2 and SO_3) and hydrochloric acid (HCl), in coal combustion flue gases [Morris, 2011]. SO_x are the precursors for acid rain, which can acidify lakes and streams, accelerate the decay of building materials and paints, and jeopardize public health [Likens, 2010]. HCl is acidic and corrosive. Surface area of quicklime and hydrated lime impacts its reactivity with sulfur oxides and hydrochloric acid gases [Borgwardt, 1985]. This study focused on producing high-surface-area quicklime as a product of limestone calcination using a novel process concept.

Commercial quicklime is conventionally produced in a rotary kiln where limestone particles (1 – 5 cm particle size) are heated for several hours at above 1,173 K [British Lime Association, 2011]. Otherwise noted, the size of any particle in this thesis always refers to the widest straight edge-to-edge distance in a particle. Exposing quicklime to high temperature in the kiln for a long residence time results in surface area < 2 m^2/g due to sintering of reactive sites [Oates, 1998]. Increasing the surface area and porosity and decreasing the particle size of lime increases its chemical reactivity with SO_2 [Borgwardt and Harvey, 1972] and HCl [Yan, et al., 2003]. An alternative method, flash calcination process, uses an entrained-flow reactor (residence time in seconds) to decompose pulverized limestone particles (< 100 μm particle size) limes that have higher surface area (up to 60 m^2/g) and porosity (void fraction of 0.5) than those prepared in conventional kilns [Silcox, et al., 1989].

Researchers at the Illinois State Geological Survey (ISGS), a division of Prairie Research Institute at the University of Illinois at Urbana Champaign (UIUC), and Electric Power Research Institute (EPRI) have developed a Sorbent Activation Process (SAP) for on-site production of

activated carbon (AC) for mercury emission control from coal combustion flue gases (US Patents 6,451,094 and 6,558,454). A full-scale demonstration of this technology was recently completed at a utility site in Illinois. SAP technology consists of a proprietary entrained-flow reactor. SAP has also been proposed for on-site production of quicklime (US Patent 20,110,223,088) to capture SO_x and HCl in coal combustion flue gases. Successful development of on-site sorbent production with SAP could potentially reduce the cost of gaseous pollutant emissions controls at coal power plants. In this study, a bench-scale SAP unit, designed and fabricated in 1995 and now located at the Applied Research Laboratory (ARL) of ISGS, was used to evaluate the impacts of operating conditions of SAP on physical and chemical properties of quicklime produced from two limestone samples. The bench-scale SAP unit has a capacity of 2 kg/hr limestone feed rate. Furthermore, non-isothermal thermogravimetric analysis (TGA) experiments were performed to determine the kinetics of calcination of limestone samples in N_2 and CO_2. TGA-derived reaction rates were employed to develop models to predict extent of calcination (EC) or conversion (α) of limestone in SAP.

1.2 Limestone Decomposition

1.2.1 General Limestone Calcination

Calcium carbonate, or limestone, thermally decomposes, or calcines, to calcium oxide by releasing carbon dioxide (Equation 1). The calcination reaction is reversible and endothermic (4.6 MJ heat required/kg of quicklime produced) [Oates, 1996]. Some limestone may contain minor amounts of calcium hydroxide which also decomposes to quicklime during the calcination reaction (Equation 2). In this study, limestone decomposition, or calcination, always refers to the decomposition of calcium carbonate to quicklime (Equation 1).

Equation 1 $$CaCO_{3\,(s)} \leftrightarrow CaO_{(s)} + CO_{2\,(g)} \;;\; K_{eq} = P_{CO_2}$$

Equation 2 $$Ca(OH)_{2\,(s)} \leftrightarrow CaO_{(s)} + H_2O_{(g)} \;;\; K_{eq} = P_{H_2O}$$

1.2.2 Mass and Heat Transport Processes in Limestone Decomposition

Limestone decomposition is a gas-solid reaction in which the solid is the reactant. The reaction involves mass- and heat-transfer processes between a solid limestone particle and the

calcination gas. The sequence of steps to convert limestone to quicklime includes five sub-processes as shown in Figure 1:

1. Transport of heat from the bulk gas at temperature T_A by radiation and convection to the solid surface (at radius, r_s) at temperature T_s (symbolized by α).
2. Transport of heat by conduction into the limestone particle to the reaction front (at radius of r_F) at temperature T_F through a porous layer of lime (symbolized by λ).
3. Dissociation reaction of $CaCO_3$ to CaO and CO_2 at the reaction interface (symbolized with k). The difference between the equilibrium partial pressure of CO_2, $P^*_{CO_2}$, (Figure 2), and the partial pressure of CO_2 at the reaction interface, P_F, is the driving force of limestone calcination reaction (Equation 1). The enthalpy of the calcination reaction is considered much larger than the internal energy; hence, the heat transport into limestone particle is negligible and the core temperature, T_M, is only slightly lower than T_S [Cheng, 2006]. P_F is higher than the partial pressure of CO_2 at the gas-solid interface, P_S, and in the bulk gas, $P_{A,}$ because CO_2 is generated in-situ during the calcination reaction.
4. Transport of generated CO_2 at the reaction interface through the porous lime layer to the outer surface of the particle (symbolized with $Dp_{,eff}$) to maintain the continuity of calcination reaction at the reaction interface.
5. Transport of CO_2 by a convection transport from the outer surface of the particle to the bulk gas with a partial pressure of CO_2 of P_A (symbolized by β) [Cheng, 2006].

Figure 1. Temperature and Partial Pressure of CO_2 Profiles during the Five Sub-Processed of Limestone Calcination [Cheng, 2006].

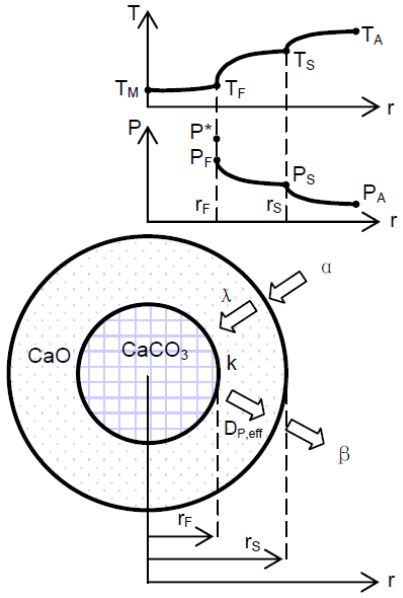

Figure 2. Equilibrium Curve of Limestone Decomposition [Baker, 1962].

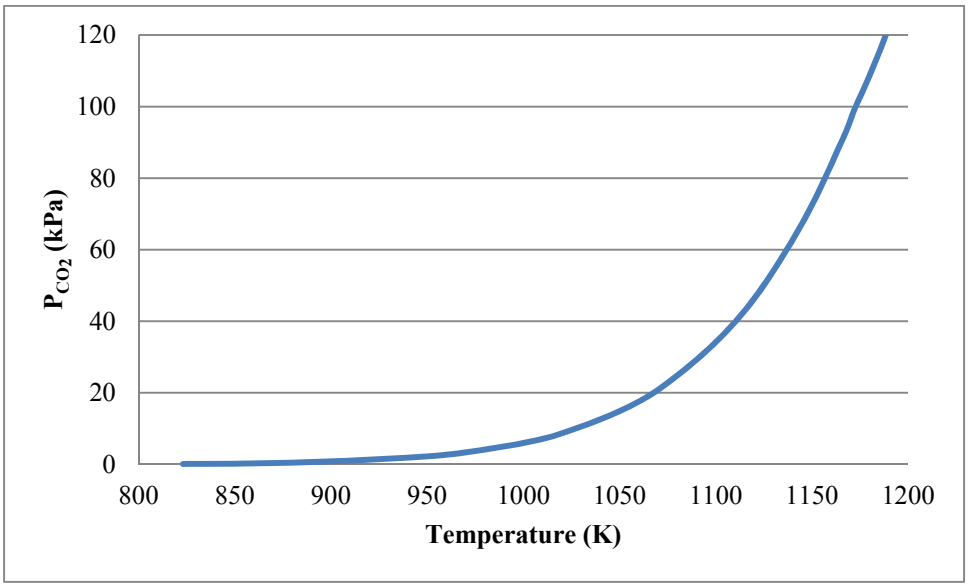

A shrinking core reaction model has been widely employed to describe thermal decomposition of a limestone particle [Ingraham and Marier, 1963; Beruto and Searcy, 1974; Elder and Reddy, 1986; Zhong and Bjerle, 1993; Fonseca, et al., 1998; Eversen, et al., 2006]. This reaction model describes conversion of a nonporous limestone solid particle in which the

reaction occurs at the outer surface and progresses into the interior of the limestone. With the progress of the calcination reaction, a layer of porous lime product is developed around the unreacted core of limestone.

1.2.3 Difficulties in Postulating a Unified Limestone Calcination Model

Modeling limestone calcination is a complex process. This complication is caused by uncertainties in identifying the rate limiting steps amongst the aforementioned five sub-processes, unique micro-structures and crystallography in different types of limestone, and changes in structures of the surface layers of lime by sintering [Oates, 1998].

1.2.3.1 Rate Limiting Step of Limestone Calcination

Satterfield and Feakes (1959) reported three different rate controlling steps of limestone calcination which included steps 1, 3, and 4 described in section 1.2.2. Hyatt, et al. obtained calcination data using a TGA method and developed a calcination model based on chemical kinetics limitation (step 3) [Hyatt, et al., 1958]. Beruto and Searcy observed a constant rate of reaction until 80% of a 1 mm outer slice of a limestone particle had decomposed [Beruto and Searcy, 1974]. Beyond this conversion, the rate decreased because a 30-μm-thick metastable CaO layer separating the unreacted $CaCO_3$ and the stable-oriented CaO layer was formed. Ohme et al. reported that below 1,273 K, limestone decomposition in an entrained-flow reactor was kinetically limited. Borgwardt used an entrained-flow reactor and reported that for particle diameter < 90 μm, limestone decomposition was kinetically controlled except during the final stages of decomposition where the diffusion of CO_2 through the product layer also became rate limiting [Borgwardt, 1985]. Khinast, et al. utilized a one-dimensional mathematical particle model that included mass transfer and diffusion in lime and limestone pore structures, diffusion through the lime product layer, heat transfer and heat conduction in the particle, reaction at the $CaO/CaCO_3$ interface and evolution of the pore structure in the particle during the calcination reaction [Khinast, et al., 1995]. They reported that heat transfer and product layer diffusion are of minor importance compared to the chemical reaction and particle diffusion resistance. On the other hand, both Hills and Campbell, et al. reported that heat transfer and product layer diffusion were the rate limiting steps [Hills, 1968; Campbell, et al., 1970]. Ingraham and Marier as well as Thompson found that only mass transfer through the product layer was the rate-limiting step

[Ingraham and Marier, 1963; Thompson, 1979]. As a conclusion, there is not a general agreement about the mechanism of limestone calcination in part because porosity, grain size, particle size, and chemical composition of limestone and calcination process conditions impact the mechanism. [Borgwardt, 1989a and b; Oates, 1998].

1.2.3.2 Sintering Phenomena in Limestone Calcination

Sintering of lime occurs because freshly generated grains grow in size and coalesce upon exposure to temperatures > 1,000 K. A direct impact of sintering is lowering the surface area and thus chemical reactivity of lime. Scanning Electron Microscopy (SEM) images of lime at different sintering levels (Figure **3**) reveal higher sintering levels in denser quicklime [Oates, 1998]. The mechanism of sintering involves transfer of lime grains during neck growth and grain fusion [Borgwardt, 1989a]. Figure 4 illustrates the neck-growth in sintering phenomena between two lime grains [German and Munir, 1976]. Keener and Kuang (1992) reported that sintering rate of lime was accelerated with increasing calcination temperature. Rapid surface area and logarithmic porosity decreases were consequences of sintering during the calcination reaction [Borgwardt, 1989a]. Borgwardt prepared a 104 m^2/g calcium oxide by calcining a 25 mg of high-purity limestone in 6 L/min N_2 flow using a differential reactor at 973 K for < 90 seconds [Borgwardt, 1989a]. He concluded that: 1) increasing particle size of limestone decreased the rate of sintering; however, the rate of sintering was independent of particle diameter between 2 – 20 μm, and 2) CO_2 and water vapors in calcination gas tended to promote sintering [Borgwardt, 1989b]. Boynton reported that the presence of high levels of sodium in limestone reduced sintering of quicklime while finely dispersed silica, alumina and iron oxide increased sintering [Boynton, 1980].

Figure 3. SEM Images of Lime at Various Sintering Levels [Oates, 1998].

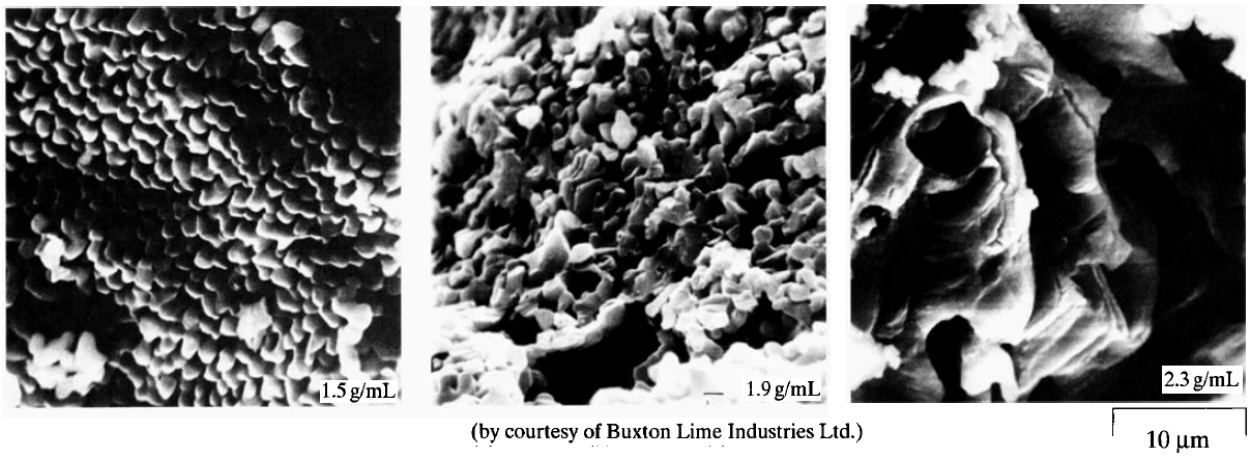

Figure 4. Neck-Growth Mechanism between Two Lime Grains [German and Munir, 1976].

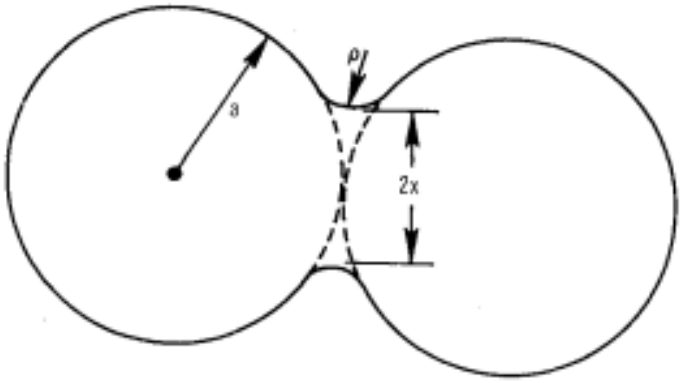

1.3 Lime Production Methods

Nowadays quicklime can be produced by either slow heating in a rotary kiln or fast heating in an entrained-flow reactor known as flash calcination [Oates, 1998].

1.3.1 Slow Heating Calcination

In commercial practice, the calcination process uses a direct-fired rotary kiln that uses coal or natural gas as its fuel. The particle size of the feed limestone is ≤ 10 cm and has a specific surface area of ≤ 1 m^2/g. The calcination temperature is generally above 1,173 K and the calcination time ranges between 2 and 4 hours. Quicklime produced commercially under such conditions have a low surface area (< 2 m^2/g) [Oates, 1998].

The time-temperature history during calcination reactions greatly impacts the conversion of the raw limestone to quicklime and the surface area of the formed quicklime. Partial pressure of CO_2 in the calcination gas determines the decomposition temperature of limestone and the rate at which the calcination reaction proceeds. The high calcination temperature and the long residence time in the kiln are the main reasons for the low surface area of the lime products. These factors contribute to grain growth by sintering, whereby the individual lime grains in a particle adhere to each other resulting in grain growth and a lower surface area per mass of particle [Oates, 1998].

1.3.2 Flash Calcination

In a flash calcination process, pulverized limestone particles (< 100 μm) are rapidly calcined in an entrained-flow reactor operating at temperature between 823 and 1,023 K and < 3 second residence time [Dinsdale, et al., 2011]. Grain growth by sintering and, therefore, surface area deactivation are much less pronounced when pulverized limestone is calcined under rapid heating and short residence time process conditions. For example, the specific surface area of CaO formed by calcination of limestone or dolomite with particle size between 10 and 90 μm particles at 1,123 to 1,348 K and < 1-second residence time ranged between 50 and 63 m^2/g [Borgwardt, 1985]. Flash calcined limes had little internal porosity, smaller grain size and plate-like grain shape [Zhong and Bjerle, 1993], while limes produced by slow heating and flash calcination processes displayed non-uniform grains which were jointed together by necks to form a continuous porous matrix [Milne, et al., 1990].

1.4 Environmental Applications of Calcium-Based Sorbents

1.4.1 Gaseous Pollutants Removal

Utility industry is among the top emitters of gaseous pollutants such as Hg, SO_x, and HCl to the atmosphere. On December 16, 2011, the United States Environmental Protection Agency (USEPA) announced the latest Mercury and Air Toxins Standards (MATS), Table 1, for new and existing coal- and oil-fired electric utility steam generating units (EGUs) [USEPA, 2012a]. The MATS rule will be implemented by 2014. Some coal-fired power plants utilize wet limestone scrubbing for SO_x control. The removal efficiency of SO_x by wet absorption technique range between 90 and 98% [Schenelle and Brown, 2002]; however, this technique is relatively

expensive (US$200 – 500/metric ton pollutant for a power plant with > 400-MW capacity and US$500 – 5,000/metric ton pollutant for a power plant with < 400-MW) and not suitable for smaller and older coal power plants [USEPA, 2012b]. Dry Sorbent Injection (DSI) processes are considered as an alternative option for some power plants to remove SO_x and HCl in the flue gas due to their lower capital and overall emissions control costs than a wet scrubbing system [EPA-452/F-03-034, 2012b]. In DSI processes, a sorbent such as lime, or hydrated lime, or Trona, or sodium bicarbonate is injected into the flue gas upstream of a particulate control device (PCD). Targeted gaseous pollutants are adsorbed onto the sorbent through chemical bonds. The spent sorbent is collected in the PCD and disposed of along with coal ash in an environmentally acceptable manner.

Table 1. USEPA MATS Limits for Coal- and Oil-Fired Power Plants [USEPA, 2012a].

Component	Generation Rate (g/MWh)
Hg	0.006 – 0.05
SO_2	680
HCl	9

1.4.1.1 Coal-Fired Power Plants

40% of the total electricity production in the U.S. is supplied by coal-fired power plants [USEPA, 2012a]. Coal combustion is an exothermic reaction and the amount of heat generated from it varies depending on the rank of coal burned (Table 2) [EIA, 1993]. Coal combustion produces CO_2 and water (main reaction products), various pollutants such as nitrogen oxides (NO_x), SO_2, SO_3, HCl (in ppm_v concentrations) and various trace metal species such as mercury and selenium, in ionic and elemental forms (in ppb_v concentrations). Table 3 shows the typical composition of a bituminous coal combustion flue gas.

Table 2. Heat Content of Various Ranks of Coal [EIA, 1993]

Rank of Coal	Heat Content (MJ/kg)
Bituminous	21 – 27
Sub-bituminous	16 – 21
Lignite	< 16

Table 3. Typical Compositions of Bituminous Coal Combustion Flue Gas [Chen, 2007].

Component	Amount
N_2 (mol %)	76 – 77
O_2 (mol %)	4.4
H_2O (mol %)	6.2
CO_2 (mol %)	12.5 – 12.8
SO_2 (ppm_v)	1500
CO (ppm_v)	50
NO_x (ppm_v)	420
HCl (ppm_v)	3
Hg ($\mu g/m^3$)	5 – 10

1.4.1.2 Control of Gaseous Pollutants by Quicklime

Chemical reactions of quicklime with SO_x and HCl are as described below.

Equation 3 $$CaO_{(s)} + SO_{2\,(g)} + 0.5\ O_{2\,(g)} \rightarrow CaSO_{4\,(s)}$$

Equation 4 $$CaO_{(s)} + SO_{3\,(g)} \rightarrow CaSO_{4\,(s)}$$

Equation 5 $$CaO_{(s)} + 2\ HCl_{(g)} \leftrightarrow CaCl_{2\,(s)} + H_2O_{(g)}$$

1.4.1.2.1 Sulfur Oxides Reactions with Calcium-Based Sorbent

Studies of sulfur oxides reaction with calcium-based sorbents were conducted extensively in 1970s and 1980s. Borgwardt used a differential reactor to measure the rate of SO_2 reaction (Equation 3) with calcium oxide particles < 500 µm in diameter [Borgwardt, 1970]. He found that the reaction rate is first order with respect to SO_2 concentration. Borgwardt and Harvey showed that the reaction is chemically controlled up to 1,253 K, and < 50% calcium conversion (conversion of CaO to $CaSO_4$) was obtained when pores in the < 100 µm CaO particles were > 0.1 µm. At conversions > 50%, the pores became completely filled with $CaSO_4$ and the rate-limiting mechanism shifted from chemical reaction to solid diffusion [Borgwardt and Harvey, 1972]. The concentration of oxygen also affected the structure of the product layer, $CaSO_4$ [Allen and Hayhurst, 1996; Dennis and Hayhurst, 1990]. They claimed that increasing

concentration of oxygen when the temperature was > 923 K produced a large number of cracks in the sorbent which helped the diffusion of CO_2 through the product layer; thus increasing conversion of CaO to $CaSO_4$.

At temperatures below 800 K, carbonation and hydration of CaO impact the rate of sulfation reaction. Hartman and Trnka (1993), Klingspor, et al. (1983), and Liu and Shih (2008) investigated the reactions of different Ca-based sorbents with SO_2 at temperatures below 775 K. Relative humidity of the reaction gas was determined to be a key parameter for SO_2 reaction with CaO. At least 20 % RH was required to obtain > 50 % SO_2 removal [Klingspor et al., 1983]. Increasing RH from 20 to 70 % improved SO_2 removal by 4 times at 340 K [Khinast, 1995 and Irabien, et al., 1992]. Carbonation reaction in a 10 – 40 % by volume CO_2 gas did not interfere with the sulfation of CaO when the concentration of SO_2 was > 2,000 ppm_v [Rochelle, et al., 1990]. This conclusion was also confirmed by Harman and Trnka [Harman and Trnka, 1993]. The presence of NO_x, O_2 and CO_2 in the flue gas doubled the rate of sulfation of calcium oxide to $CaSO_4$ at 330 K [Liu and Shih, 2008].

Kocaefe, et al. investigated the sulfation rate of a reagent-grade CaO with SO_2 and SO_3 using a TGA and showed that below 600 K, CaO only reacted with SO_3 [Kocaefe, et al., 1985]. Benson et al. confirmed this conclusion by showing that SO_2 did not react at an appreciable rate with $Ca(OH)_2$ between 422 and 450 K; however, SO_3 reacted efficiently with $Ca(OH)_2$ [Benson, et al., 1998. The reaction rate of CaO with SO_3 was faster than SO_2 at all temperatures at comparable concentrations of SO_2 and SO_3 [Kocaefe, et al., 1985]. It was shown that the initial reaction rate was first order with respect to SO_3 concentration. Thibault, et al. studied the kinetics of SO_3 reaction with calcium oxide samples in a fixed bed reactor and concluded that for < 170 µm CaO particles, the reaction rate was independent of particle size because the diffusional resistance associated with individual grains was dominant [Thibault, et al., 1982].

1.4.1.2.2 HCl Reaction with Calcium-Based Sorbents

Reactions of HCl with calcium-based sorbents are similar to those of the sulfur oxides described in section 1.4.1.2.1. The rate of reaction of CaO with HCl is first order with respect to the concentration of HCl under a reaction controlled region [Yan, et al., 1993]. The HCl reaction with CaO was more favorable than SO_2 at 923 K [Daoudi and Walters, 1991]. Above this

temperature, the HCl reaction rate remained unchanged. Similar to SO_2 and SO_3 reactions with basic oxides, HCl reaction with CaO was kinetically controlled at conversions < 10 % and > 10 %, it was controlled by reaction kinetics and product layer diffusion [Fonseca, et al., 2003]. To achieve conversions > 98 %, the presence of moisture was required and in the absence of moisture, only 5 % conversion was achieved [Fonseca, et al., 1998].

1.4.2 Impact of SO_3 on Mercury Removal in Activated Carbon Injection (ACI) Processes

1.4.2.1 Mercury Regulation

Mercury is a bio-accumulative toxin which can cause deformities on fetus, impair nervous system and lead to lethality at high concentrations [USEPA, 2012c]. Coal-fired power plants are the largest source of mercury emission in the U.S. (45 metric ton/year), generating 45 % of the U.S. total emissions [USEPA, 2012a]. To date, 19 states, including Illinois, require mercury reduction standards for coal- and oil-fired power plants. In December 2011, USEPA finalized MATS rule which limit the toxic pollutants from coal-power plant including mercury. When implemented, coal fired power plants are required to practice the MACT standards and meet 0.006-0.05 g/MWh mercury emission by 2014 [USEPA, 2012a].

1.4.2.2 Mercury Removal from Combustion Gases with Activated Carbon Injection

Activated carbon injection (ACI) process is emerging as an affective low cost technology for removal of vapor-phase mercury from coal combustion flue gases [Hoffmann and Ratafia-Brown, 2003 and Zhuang, 2011]. In ACI, powdered activated carbon (PAC) is injected into the flue gas ductwork of a coal-fired power plant, downstream of boiler and up-stream of PCD such as a baghouse or an electrostatic precipitator (ESP). PAC adsorbs the vapor-phase mercury in the flue gas and is collected with the fly ash in the PCD. Depending on the type of coal burned and PCD installed on the plant, ACI can reduce mercury emissions by > 90 % [Hoffmann and Ratafia-Brown, 2003]. The schematic diagram of the ACI process in coal-fired power plants is shown in Figure 5.

Figure 5. Schematic Diagram of ACI Process in Coal-Fired Power Plants.

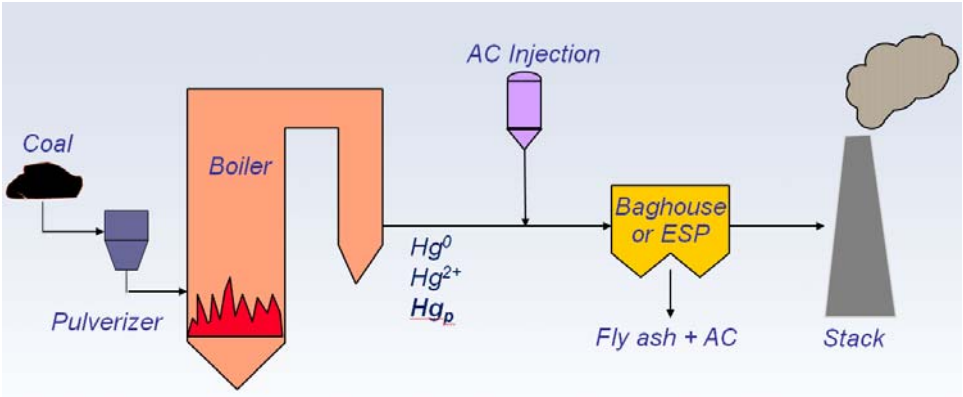

1.4.2.3 Sorbent Activation Process (SAP)

SAP is a technology for on-site production of PAC at power plants using the same coal burned for electricity generation. This technology was developed by ISGS and EPRI and is currently being demonstrated at full-scale (US Patents 6, 451, 094 and 6,558,454). PAC produced in bench, pilot, and full-scale SAP units from different types of coal had comparable mercury-removal performances to the commercial Darco-Hg activated carbon (manufactured by Norit Americas) as shown in Figure 6 [Rostam-Abadi, et al., 2009].

In SAP, pulverized coal is injected into an entrained-flow reactor in which coal devolatilization and coal char activation reactions occur in < 3 seconds. The heat of reactions in SAP is provided by burning the volatile matters released during the initial devolatilization stage of the coal, or by burning an auxiliary fuel (propane). PAC produced in SAP is directly injected in to the flue gas duct upstream of an existing ESP or a baghouse. Figure 7 shows the schematic diagram of the implementation of SAP technology in an ACI process in coal-fired power plants. EPRI has estimated that SAP technology would reduce the cost of ACI for mercury control by at least 50 % [EPRI, 2010].

Figure 6. Impact of Surface Area of SAP-Derived AC on Hg-Removal Efficiencies Normalized to the Commercial PAC (Darco-Hg) [Rostam-Abadi, et al., 2009].

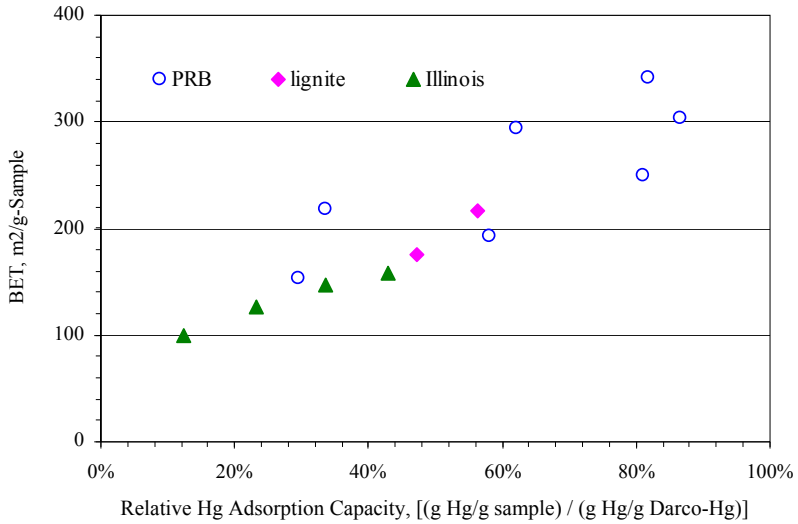

Figure 7. SAP-Enhanced ACI Schematic Diagram.

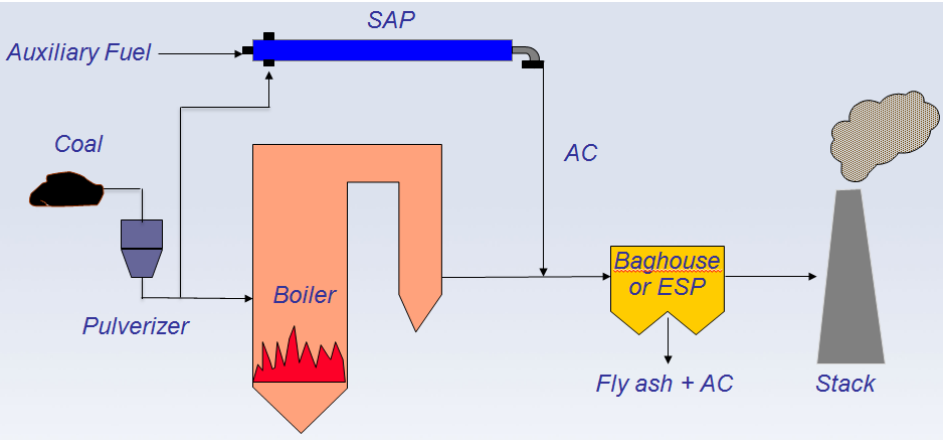

1.4.2.4 Impact of SO_3 on Hg Removal by AC

Mechanisms of mercury adsorption onto AC are very complex. Contributing parameters include pore-size distribution, carbon surface chemistry, flue gas constituents (HCl, SO_x, NO_x), temperature, and concentrations of mercury species (elemental or oxidized) in the flue gas [Zhuang, 2011; Hsi, et al., 2001]. Results from pilot-scale and full-scale ACI tests have shown total mercury removal up to 95 % for low-sulfur flue gas [Lee, 2003, 2004]. However, the presence of SO_3 in the flue gas, even at concentration as low as 10 part per million (ppm_v),

significantly reduce the ACI's Hg removal because SO_3 and Hg compete to bind onto AC sites, Figure 8 [Feeley, et al., 2009].

Figure 8. Impact of SO_3 on Mercury Removal Efficiency by ACI [Feeley, et al., 2009].

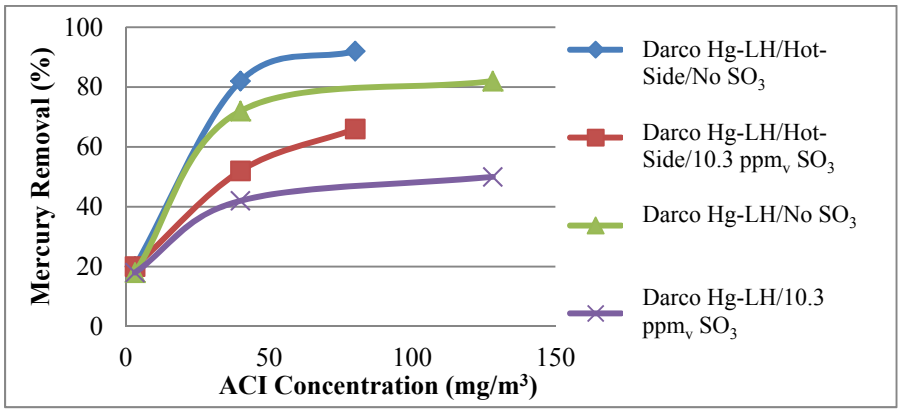

To enhance mercury removal in a high-sulfur flue gas, either a carbon that inhibits SO_3 adsorption should be used or SO_3 in the flue gas should to be removed. Injection of quicklime or hydrated lime into flue gas is one option to remove SO_3. SAP is being considered for co-production of AC and quicklime for control of mercury emissions from high-sulfur flue gas (US Patent 20,110,223,088). Figure **9** shows the implementation of SAP technology in a DSI process for on-site co-production of AC and quicklime at coal-fired power plants.

Figure 9. Schematic Diagram of On-Site Co-Production of AC and Lime by SAP at Power Plant.

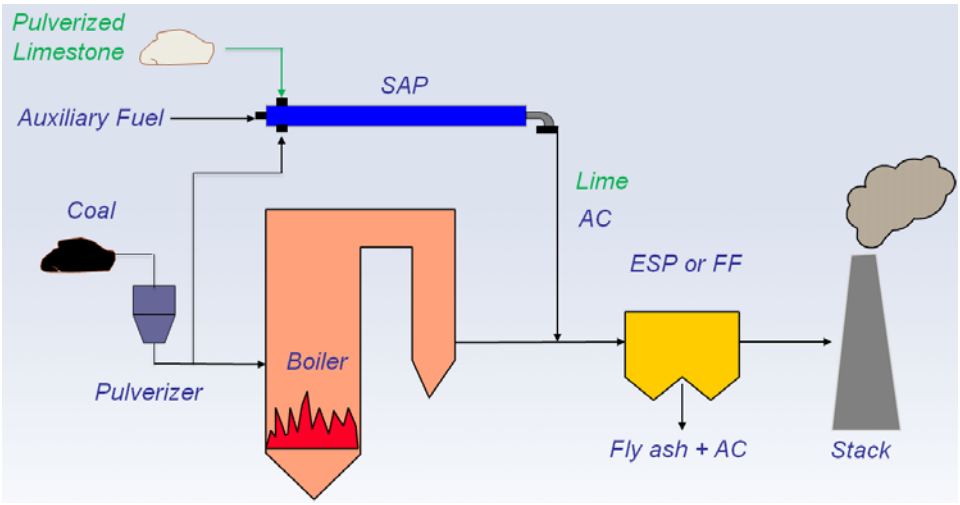

1.5 Benefits of SAP Sorbents to Pollutants Control Technique Utilizing DSI

Lime production in SAP is a flash calcination process because pulverized limestone particles (< 100 µm) are exposed to a hot flue gas in a few seconds (< 5 seconds). Figure 10 and Figure 11 show the step-by-step processes of limestone utilization in DSI application without and with SAP. On-site production of lime via SAP clearly simplifies the DSI process at a utility site. It shortens the production time of the sorbent and also increases the availability of the sorbent at the plant. Storing a reactive sorbent and maintaining its reactivity can be costly. Thus, DSI-SAP technique can reduce the storage cost by stocking limestone instead of lime sorbent. A large amount of limestone fine (particle size < 45 µm) is often produced during grinding and sieving operations at limestone and lime companies. It is commonly disposed of in quarries because commercial demand for limestone fine is not large; hence it can be purchased at a lower cost than size-graded limestone and used as a feedstock in SAP, further reducing the cost of producing quicklime. Lime sorbent produced in SAP has a high surface area (between 5 to 12 m^2/g) and fresh active sites to enhance its reactivity. Hence, DSI-SAP represents an innovative approach to reduce emission control costs in coal-fired power plants.

Figure 10. Limestone Utilization in DSI without SAP.

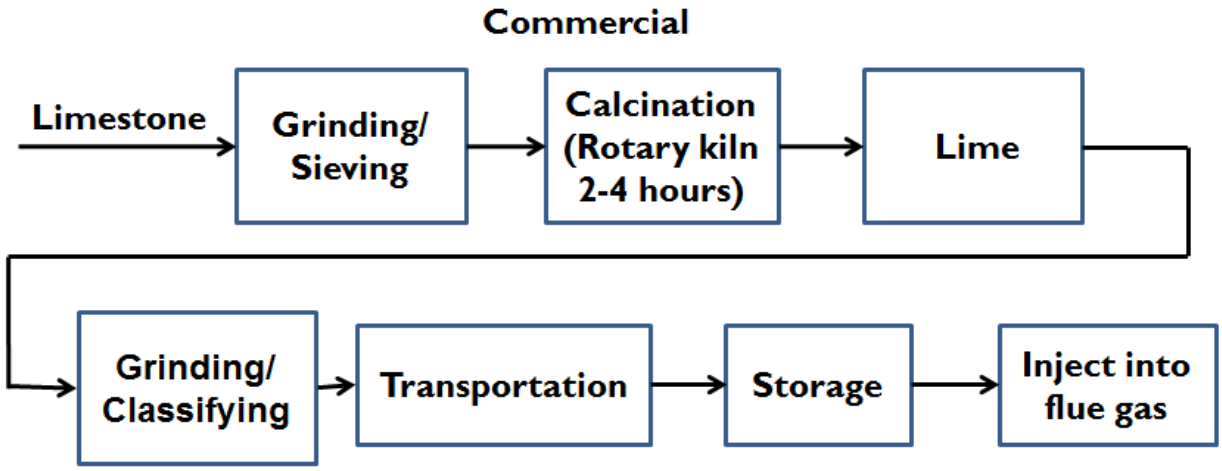

Figure 11. Limestone Utilization in DSI with SAP.

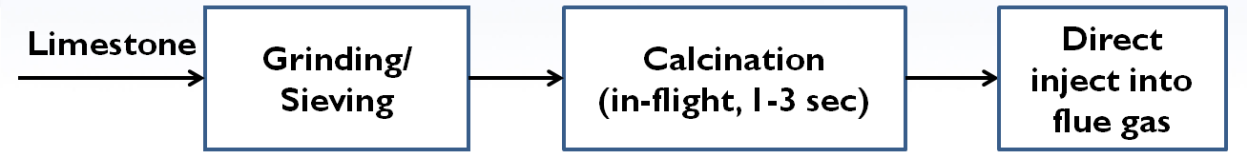

1.6 Objectives and Contributions of This Research

The main objective of this research is to study the feasibility of producing quicklime for DSI application using a bench-scale SAP and to determine the impacts of SAP's operating conditions such as temperature profile, residence time, and gaseous composition on the percentage of $CaCO_3$ decomposed to CaO and surface area of product quicklime. The second objective is to investigate the kinetics of limestone calcination using non-isothermal TGA technique and to develop models to predict thermal decomposition of limestone in SAP. Achieving these engineering objectives is very important to help provide design data for scale up of SAP and predict limestone calcination behavior in pilot-scale and full-scale SAP studies.

2 MATERIAL AND METHODS

2.1 Experimental

Experimental work performed in this research included limestone calcination tests to determine the impact of operating conditions of bench-scale SAP on the physical and chemical properties of lime products, characterization of limestone samples and product limes produced in the SAP, non-isothermal TGA calcination experiments to determine kinetic parameters of thermal decomposition of limestone samples, and developing reaction models to predict limestone calcination in SAP. Research flow diagram of this study is described in Figure 12.

Figure 12. Research Flow Diagram.

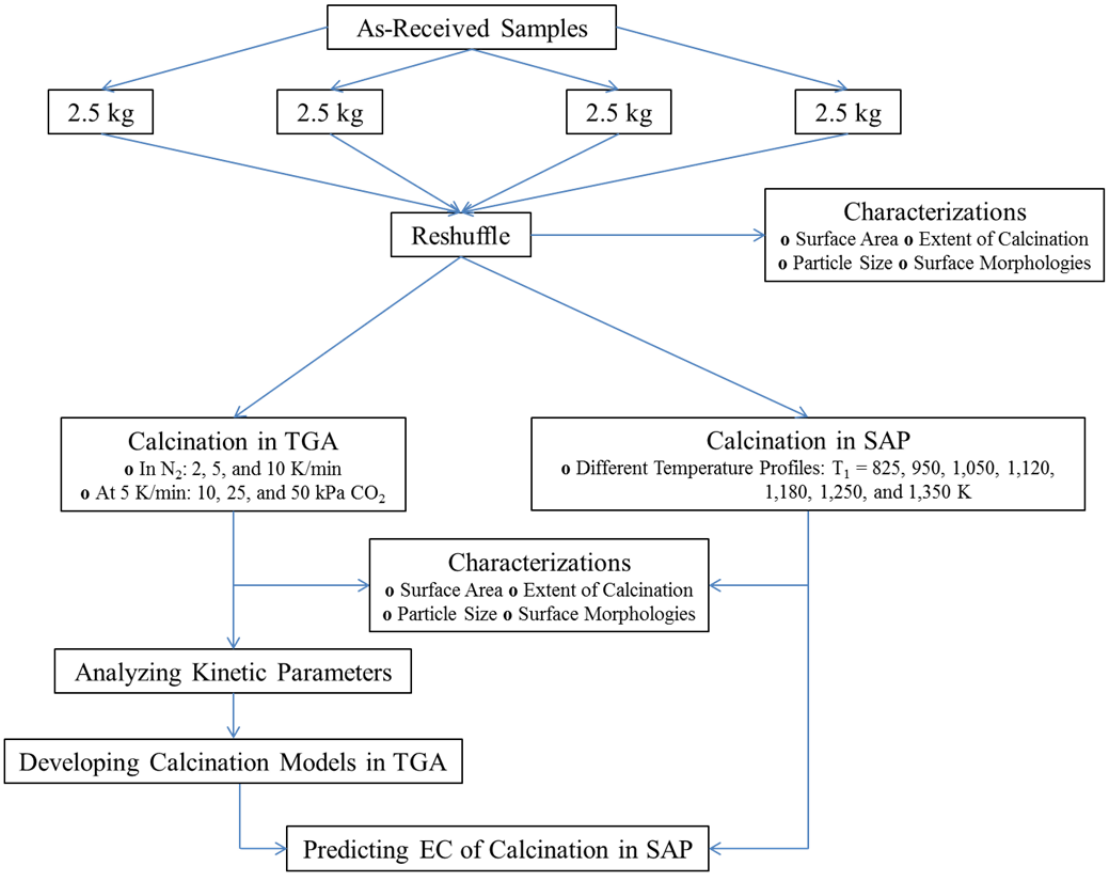

2.1.1 Sample Preparation

Two limestone samples were tested. Sample MSS-LS was obtained from Mississippi Lime Company and sample MRC-LS was obtained from Mercury Research Center (MRC) at

Gulf Utility in Pensacola, Florida. The latter sample was used in several pilot-scale SAP tests at MRC. Two 10 kg buckets of each pulverized limestone were shipped to ISGS. As-received pulverized limestone samples were dried overnight at 333 K at atmospheric pressure. Each 10 kg limestone bucket was riffled into four 2.5 kg to obtain uniform and representative samples for characterization and calcination experiments. These 2.5 kg portions of limestone were stored in closed plastic buckets at ambient air temperature and pressure.

2.1.2 Material Characterizations

Material characterizations included analysis of particle size distribution, surface area, surface morphology, and CaO content or EC or conversion of a sample using TGA.

2.1.2.1 Particle Size Distribution

As previously mentioned, the term "particle size" used here refers to the widest straight edge-to-edge distance in a solid limestone particle. Particle size analysis was performed using a HORIBA's LA-300 Laser Diffraction Particle Size Distribution Analyzer (Figure 13). The LA-300 uses Mie Scattering Theory (laser diffraction) to measure particle size in the range of 0.1 - 600 μm. A 650 nm solid-state, diode laser is focused by an automatic alignment system through the measurement cell. Light is scattered by sample particles to a 42-element detector system including high-angle and backscatter detectors, for a full angular light intensity distribution [HORIBA, 2011]. The highly-refined optical design and algorithm provides measurements in 20-second intervals with high accuracy. In a typical test, 10 mg of a sample was added to the liquid dispersing medium. The recommended dispersing medium for the limestone/lime samples is isopropyl alcohol (IPA). In this study, each limestone particle size distribution analysis was performed twice and the results were consistent and reproducible.

Figure 13. HORIBA's LA-300 Laser Diffraction Particle Size Distribution Analyzer.

2.1.2.2 Surface Area Measurement

Surface areas of samples were measured using a Quantachrome Monosorb B.E.T. Surface Area Analyzer, Figure 14. This instrument uses a rapid dynamic nitrogen flow method and provides a single-point B.E.T surface area at a relative pressure P/Po = 0.30. The reproducibility of measurement in this equipment is > 0.5 % [Quantachrome, 2011]. This instrument operates at atmospheric pressure and uses 70 cc/min of N_2/He (70 / 30 %) flow rate, as specified by the manufacturer. In a typical test, the glass sample cell was filled with < 0.5 g of sample. The sample in the cell was then degassed using a heating mantel at 400 K for 20 minutes to remove moisture and other trapped gases in the sample prior to the N_2 adsorption/desorption experiment. After degassing, the cell was placed into the adsorption port for surface area measurement. Two containers filled with liquid N_2 were used as cold traps to ensure a rapid dynamic flow of the N_2 gas in the system. N_2 was chosen as the adsorbed gas because it is inert and would not react with the sample. During the adsorption process, sample cell was submerged into the liquid N_2 to increase the adsorption rate. The adsorbed N_2 was desorbed when the cell was taken out of the liquid N_2 bath which also increased the sample's temperature. A built-in detector measured the volume of N_2 gas adsorbed/desorbed, translated the data into the total surface area data, and displayed it on the measurement display screen. Specific surface area of sample (m^2/g) was calculated by dividing this number by the mass of the sample.

Figure 14. Monosorb B.E.T. Surface Area Analyzer.

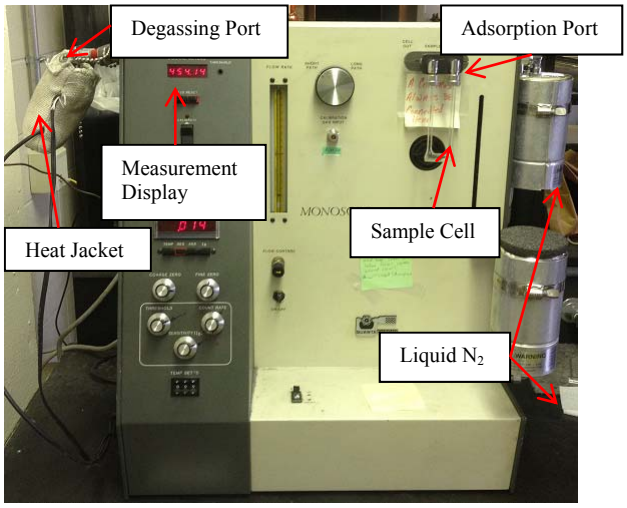

2.1.2.3 Surface Morphology Analysis

Surface morphology analysis was performed using a Hitachi S-4700 Scanning Electron Microscope (SEM) at UIUC's Center for Microanalysis of Materials, Figure 15. In a typical test, the sample was loaded on a piece of carbon tape located at the top of an aluminum sample holder. The lime/limestone sample was gold-coated using an Emitech 575 Sputter Coater, Figure 16, to eliminate any electron discharges that could reduce the resolution of the sample's image. The sample was analyzed at < 1 Pa with an accelerating voltage of 15kV.

Figure 15. Hitachi S-4700 SEM.

Figure 16. Emitech 575 Sputter Coater.

2.1.2.4 Non-Isothermal TGA Calcination

Calcination profiles of samples were measured using a Thermo Scientific Versatherm TGA, Figure 17. The data were used to calculate the concentrations of limestone and quicklime lime in SAP products. In a non-isothermal TGA test, a sample is heated at a linear heating rate from ambient to a pre-determined temperature in a flowing purge gas. During the experiment, the weight of the sample and the temperature of the gas phase in the vicinity of the sample pan are continuously measured. Versatherm's mass-temperature analysis software simultaneously generates thermogravimetric-differential thermal analysis (DTGA), which corresponds to the rate of weight change at a given reaction temperature. In each calcination test, N_2 at a total flow rate of 100 mL/min purged the TGA tube where the sample pan was located.

Figure 17. Schematic Diagram of Thermo Scientific Versatherm TGA (Thermo Scientific, 2011).

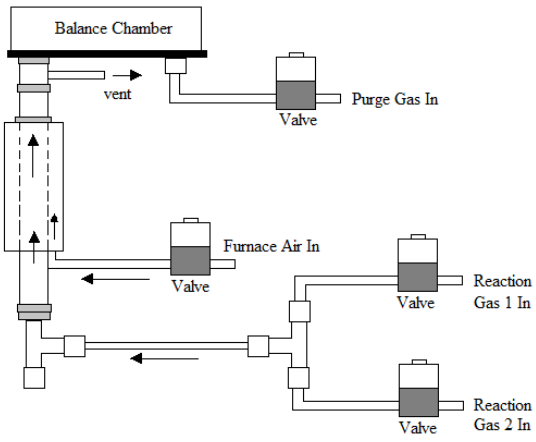

There are three possible stages in a non-isothermal TGA calcination experiment. The first stage comprises of water/moisture release from the sample indicated by weight changes < 473 K. Second stage consists of dehydration of any $Ca(OH)_2$ present in the sample indicated by weight change between 673 and 823 K. The last stage represents decomposition of calcium carbonate indicated by weight change above 825 K. In this study EC, defined as the mass conversion of $CaCO_3$ to CaO or simply the percentage of CaO present in a sample, or conversion, was determined by the amounts of weight changes measured during the third stage of non-isothermal TGA experiment of a sample. Equation 6 was used to calculate EC of a sample. The numerator in Equation 6 represents the actual % wt. loss of the analyzed sample, while the denominator indicates the theoretical % wt. loss (44 %) for decomposition of a pure $CaCO_3$.

Equation 6

$$\% \, \mathbf{EC} = \frac{\% \, \mathbf{Wt \, Sample_{at \, 825 \, K}} - \% \, \mathbf{Wt \, Sample_{at \, 1,180 \, K}}}{\% \, \mathbf{Wt \, Change_{CO_2 \, release}}} \times \mathbf{100} \, \%$$

2.1.3 Calcination in Bench-Scale SAP

SAP experiments were performed by injecting as-received pulverized limestone samples at different temperatures. Product samples were collected on regular time intervals for characterization studies.

2.1.3.1 Bench-Scale SAP

The bench-scale SAP is essentially a L-shaped entrained-flow reactor with 13.4 cm inside diameter, 94 cm outside diameter, and 410 cm total length. It has several ports for injecting either coal or limestone into the reactor or measuring gas-phase temperature at various locations in the SAP, Figure 18. The green arrows indicate the direction of gas and particle flow, starting from the injection port to the SAP's gas exhaust and sampling port. A Krom Schroder BIC-65 burner, a pre-mix burner with the maximum capacity of 70 kW is located 55 cm upstream of the injection port and used to burn propane as the main heat source in this unit.

Figure 18. Front View of the Bench-Scale SAP Reactor.

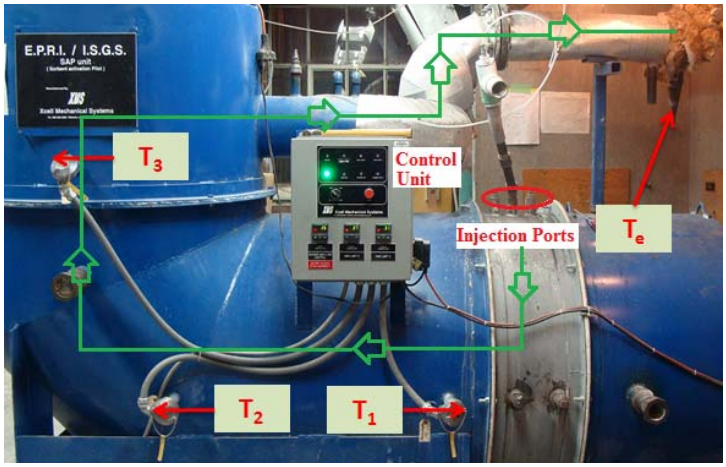

High-pressure propane cylinders, supplied by S.J Smith (Champaign, IL), and compressed air available at ARL were used as fuel and air sources in this research. Both gases entered the reactor from the front end of the SAP (Figure 19). Pressure regulators controlled the pressure in the propane line at 30 psig or 207 kPa and the air line at 90 psig or 621 kPa to prevent over-pressurizing the line and tubing connections. Three desiccators were used to remove moisture from the air line before entering the burner. A U-tube connected the propane and air lines to monitor the air to propane flow ratio. This ratio is transmitted as a signal to the SAP's control unit. SAP would not ignite if this ratio was not monitored appropriately. A CO alarm manufactured by Kidde was installed immediately outside of the SAP to alert when the concentration of CO in the room exceeded 50 ppm_v as shown in Figure 19 [Kidde, 2012].

Figure 19. Propane and Air Supply Lines into the Bench-Scale SAP Reactor.

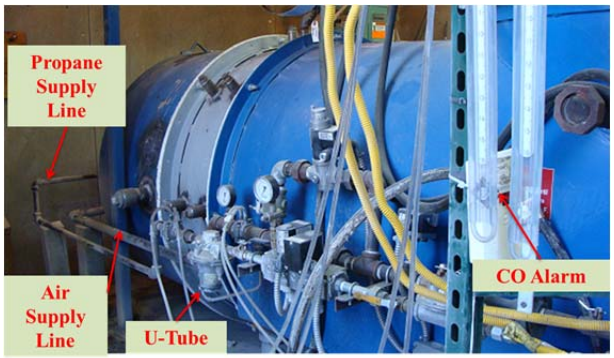

Type-K thermocouples were installed at T_1 = 112 cm, T_2 = 237 cm T_3 = 252 cm locations downstream of the burner to continuously monitor temperatures along the reactor path (Figure 18). A hand-held digital thermocouple [Fluke, 2012] was placed at the exit of the SAP to read the exhaust temperature (T_e). Signals from T_1, T_2, and T_3 thermocouples were monitored by a control unit. If any of the thermocouples at these locations read above 1,750 K, the SAP automatically shut off for safety. There was no thermocouple at the injection port. Therefore, in separate experiments, the hand-held digital thermocouple was used to measure the temperature at the injection port at different SAP operating conditions. On average, the temperature measured at the injection port was 10 % higher than the temperature at location T_1. T_1 location is about 35 cm downstream of the injection port. An involute cyclone, described in section 2.1.3.4, equipped with a gas analyzer probe was used to collect the solid products at the exit of the SAP Figure 20. The flue gas exited SAP through a main flue gas exit (Figure 20) to a hood.

Figure 20. Sample Collection Unit at the Exit of the Bench-Scale SAP.

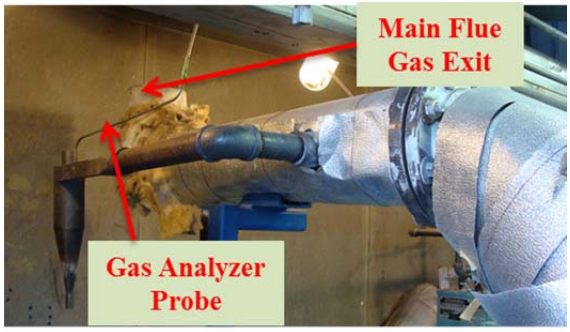

2.1.3.2 Limestone Feeder

An AccuRate Dry Material Feeder 300, shown in Figure 21, was used to feed limestone into SAP [AccuRate, 2012]. During several initial shakedown SAP tests, the limestone feed line gradually became clogged with fine limestone particles in < 3 minutes. This issue disturbed the limestone feed rate into the SAP and resulted in aborting a test. The feed line set-up used a polyvinyl chloride (PVC) T-tube extended with a 25 cm plastic hose as shown in the Figure 22A. The main reason for clogging was because some of the hot and humid flue gas inside SAP entered the feed line and caused agglomerated limestone particles at several locations around the auger and causing the auger to halt. A revised design (Figure 22B) of the feeder tube

significantly reduced the clogging and overcame the plugging problem. In the new design, a N_2 flow was introduced in the limestone feed line to prevent the SAP flue gas entering the feed line.

Figure 21: AccuRate Dry Material Feeder 300.

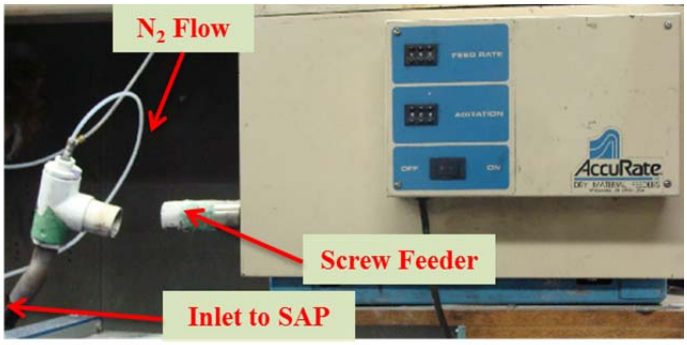

Figure 22: Limestone Feed Line Set-Up Designs. A) Initial Design. B) Modified Design.

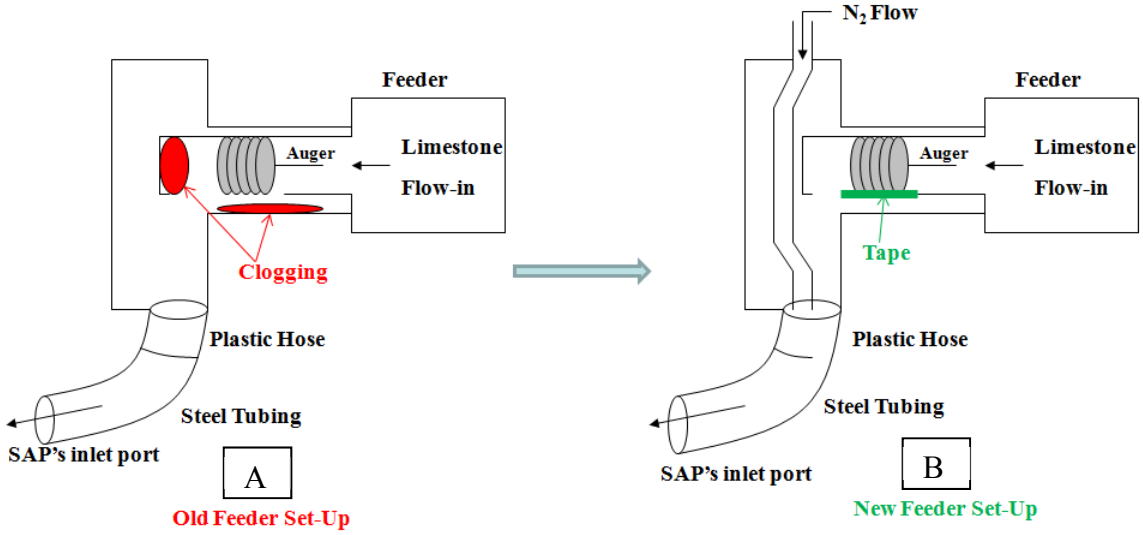

2.1.3.3 Calibration Curves (Feeder, Air, Propane, and Nitrogen)

Limestone feed rate, propane, combustion air, and nitrogen flow rates were calibrated to assure desired SAP operating conditions were achieved and mass and energy balances were accurately conducted. Calibration of limestone mass feed rate was performed by measuring the weight of limestone collected in a bucket in 15 minute periods. The calibration curve of the feeder is shown in Figure 23. In this research, SAP tests were performed at a limestone feed rate of 1 kg/hr, corresponding to the AccuRate's feed rate dial 60. Calibration curve for the feeder's nitrogen flow rate was obtained using a Bios DryCal ® ML-500 Primary Gas Flow Calibrator

(Figure 24). A nitrogen flow rate of 44 L/min was used in all experiments. Xcell Inc, Pekin, IL, the company who manufactured SAP, provided the calibration curves for propane and combustion air flow rates, Figure 25 and Figure 26. These calibration curves provide correlations between pressure drops measured across each line (kPa) and flow rate (L/min).

Figure 23. Calibration Curve of Limestone Feed Rate.

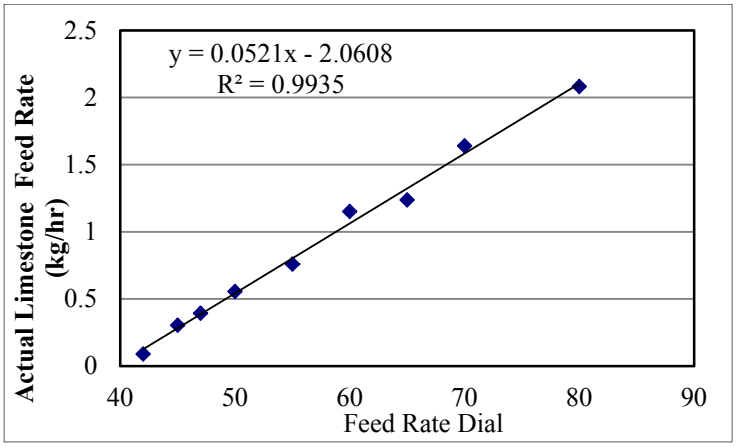

Figure 24. Calibration Curve of Feeder's Nitrogen Flow Rate.

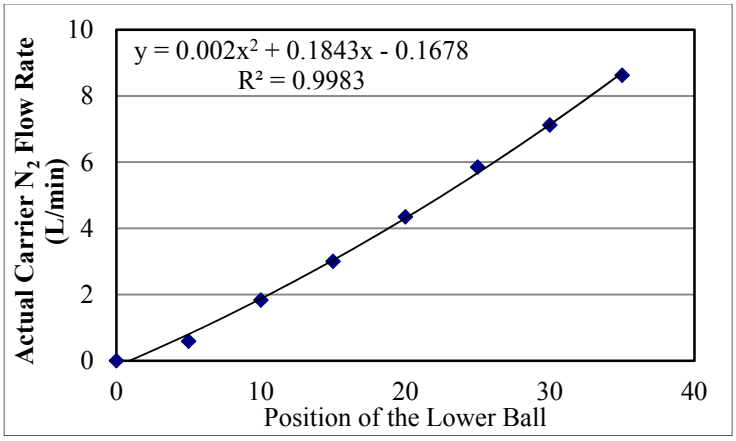

Figure 25. Calibration Curve of Propane Flow Rate.

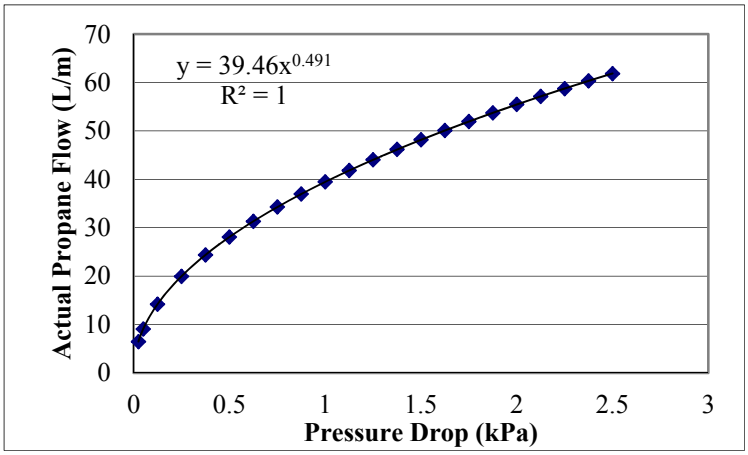

Figure 26. Calibration Curve of Combustion Air Flow Rate.

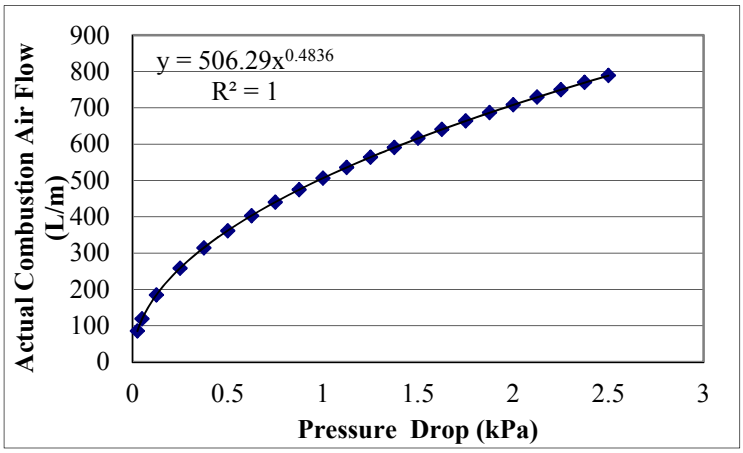

2.1.3.4 Product Sampling with an Involute Cyclone

Quicklime product particles exiting the SAP were collected using an involute cyclone with an inlet perpendicular to the gas flow direction. An involute cyclone with standard proportions was designed and custom fabricated at Silver Machine Shop, Urbana, IL, from a 16-gauge-rolled-steel material according to the design specifications shown in Figure 27 [Wark, et al., 1998]. The cyclone was designed to collect 90 % of 10 µm particles consisting of 75 % CaO and 25 % $CaCO_3$ exiting the SAP at an outlet temperature between 656 and 1,087 K. The cyclone has a rectangular aerosol inlet with an inner wall tangential to the cylinder. The inlet bends gradually within the cylinder over the 180^o involute.

Figure 27. Schematic of Design of Cyclone.

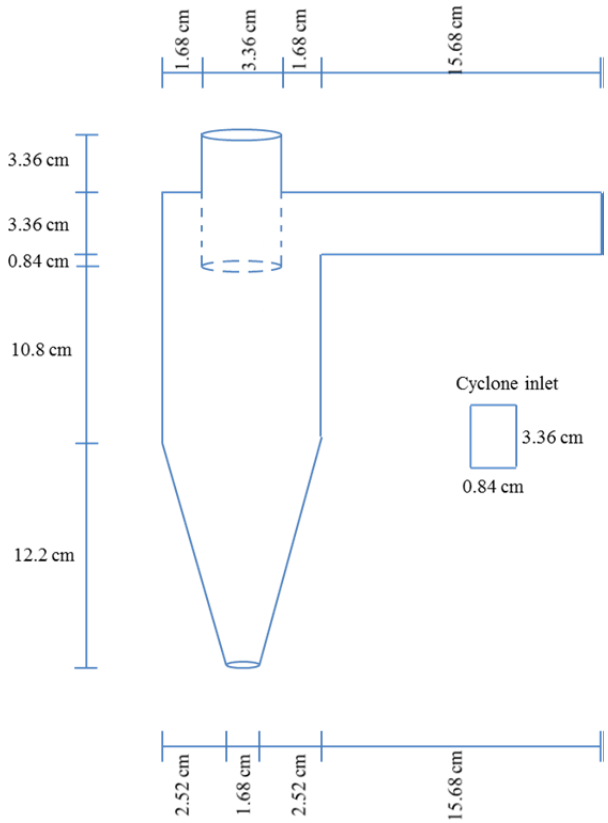

2.1.3.5 Flue Gas Composition Measurement

Because limestone calcination is a reversible reaction, the EC is directly affected by the CO_2 partial pressure in the calcination gas. CO_2 and moisture slow down the rate of calcination and promote the rate of sintering of lime grains. Both of these phenomena lower the development of surface area during calcination [Borgwardt, 1989b]. Therefore, measuring the concentration of CO_2 in the calcination gas can help explain the surface area development and EC of the SAP product. Measuring the flue gas composition also helps obtain consistent fuel-lean conditions (complete propane combustion) in SAP experiments.

In this study, the composition of SAP flue gas was monitored using a Ferret 16 GasLink II gas analyzer, Figure 28. According to the specifications provided by the manufacturer, this instrument measures the concentrations of CO (0 – 15.00 % vol.), CO_2 (0 – 20 % vol.), O_2 (0 – 25 %), NO_x (0 – 5,000 ppm_v), and total hydrocarbons (HCs) (0 – 15,000 ppm_v). The detection limits for CO, CO_2, O_2, NO_x, and HCs are 100 ppm_v, 1,000 ppm_v, 1,000 ppm_v, 1 ppm_v, and 1

ppm_v [GXT, Inc, 2012]. The probe of the gas analyzer was inserted either at the outlet of the SAP where the flue gas exited or at the outlet of the cyclone. A built-in vacuum pump drew SAP flue gas into a water trap before entering the detector. The water trap consisted of a glass bottle to condense any water vapor in the flue gas followed by several desiccants. The partial pressure of water in SAP flue gas was estimated by calculating the amount of water produced by burning the known volume of propane gas.

Figure 28. Ferret 16 GasLink II Emission Analyzer.

2.1.3.6 Terminal Settling Velocity of Spherical Limestone Particles

Terminal settling velocities of the limestone particles were calculated to determine the minimum flue gas velocity required to prevent limestone / lime particles from settling in SAP. When the flue gas velocity is higher than the terminal settling velocity, particles could be entrained and transported in the gas flow because the drag and buoyancy forces are higher than the gravitational force which prevents particle from settling. However, this velocity does not solely determine the fate of particle settlement in SAP. Residence time of particles and the flow restrictions around the two 90-degree elbows of SAP also impact particle settling.

The terminal settling velocity was calculated by using iterations method. Initially, a random yet reasonable settling velocity was assumed and Reynolds number (Re) of the particle at this assumed velocity was calculated using Equation 7, where ρ_F and μ are the density (kg/m^3) and viscosity ($kg\ m^{-1}\ s^{-1}$) of the gas, U (m/s) is the terminal velocity, and L (m) is the particle size of the injected limestone. Drag coefficient (C_D) was then determined using Equation 8

[Morrison, 2010], and a calculated settling velocity was determined by Equation 9 , where g (m/s^2) is the gravitational acceleration and ρ_S (kg/m^3) is the particle density of limestone. Iterations were performed until the assumed and the calculated settling velocities agreed to within 1 % deviation. The densities and viscosities of the flue gas in the SAP were determined using CHEMCAD 6.4 software (Chemstations^{TM}). Particle size distribution analysis of as-received limestone samples (provided in Section 3.2.1) revealed that the largest particle in the sample was 80 µm and majority of these samples was < 40 µm (> 95 wt % for MRC-LS and > 98 wt % for MSS-LS). Therefore, settling velocity calculations were made for a limestone particle with diameter of 40 µm. The density of limestone used in this calculation was 2,700 kg/m^3 higher than the density information (961 kg/m^3) provided by Mississippi Lime, the supplier of MS-LS sample [Oates, 1998]. A larger and denser particle will have a higher terminal settling velocity.

Equation 7

$$\mathbf{Re} = \frac{\rho_F . U . L}{\mu}$$

Equation 8 for Re < 2

$$\mathbf{C_D} = \frac{24}{\mathbf{Re}}$$

for Re > 2

$$\mathbf{C_D} = \frac{24}{\mathbf{Re}} + \frac{2.6\left(\frac{\mathbf{Re}}{5}\right)}{1+\left(\frac{\mathbf{Re}}{5}\right)^{1.52}} + \frac{0.411\left(\frac{\mathbf{Re}}{5}\right)^{-7.94}}{1+\left(\frac{\mathbf{Re}}{263{,}000}\right)^{-8}} + \left(\frac{\mathbf{Re}^{0.8}}{461{,}000}\right)$$

Equation 9

$$\mathbf{V_T} = \sqrt{\frac{4\,g\,L}{3\,C_D}\left(\frac{\rho_S - \rho_F}{\rho_F}\right)}$$

2.1.3.7 Recarbonation in SAP

Recarbonation of quicklime (Equation 10) occurs when the partial pressure of CO_2 in the calcinations gas is larger than the equilibrium CO_2 pressure (P_{CO_2} > Keq, Figure 2) at a given reaction temperature. The rate of decomposition and recarbonation; thus, EC in SAP are influenced by the reaction temperature and partial pressure of CO_2 in the calcination gas. Therefore, knowing the temperature profiles and partial pressure of CO_2 inside the SAP will help determine calcination and recarbonation zones. Table 4 shows the calculated compositions of the propane combustion flue gas at different levels of excess air by assuming ideal conditions

including perfect gas mixing, complete combustion (no CO and HCs in the flue gas) and excluding NO_x formation (no NO_x in the flue gas).

Equation 10 $$CO_{2\,(g)} + CaO_{\,(s)} \leftrightarrow CaCO_{3\,(s)}$$

Table 4. Predicted Compositions of SAP's Flue Gas at Various Levels of Excess Air.

Excess Air (%)	CO (ppm_v)	CO_2 (%)	O_2 (%)	HCs (ppm_v)	NO_x (ppm_v)
50	0	7.59	6.33	0	0
28	0	8.82	4.12	0	0
20	0	9.38	3.13	0	0
14	0	9.84	2.30	0	0
0	0	11.11	0.00	0	0

These calculations were made to estimate partial pressure of CO_2 in the combustion gas in SAP. Realistically, NO_x is also formed during the combustion of propane in air. NO_x and CO formations were neglected because their concentrations are smaller (in ppm_v) than the concentration of CO_2 and do not affect the recarbonation reaction of CaO in SAP. Comparisons between more realistic predicted and measured concentrations of NO_x, CO and HCs when burning propane in air are discussed in section 3.1.

2.1.3.8 Gas Velocity and Particle Residence time in SAP

Gas velocity and particle residence time are equally important parameters to calculate the EC of limestone in SAP. In the bench-scale SAP, they are indirectly controlled by adjusting the temperature at T_1 location. Gas velocity (u_{gas}) in SAP was calculated using Equation 11, where Q and A represent the volumetric flow rate of flue gas (m^3/s) and cross sectional area of SAP's inner tube (0.018 m^2). The total Q generated by burning propane with house air (21% O_2 and 79 % N_2) was calculated by assuming complete combustion of propane (no CO formation), non-

reactive N_2 (no NO_x formation), and ideal gas conditions (Equation 12), where ṅ is the total molar flow rate of air (mol/s). Calculation of Q was challenging because the flue gas temperature varied at different locations of SAP. To simplify the calculation, average temperatures (T_{av1}, T_{av2}, and T_{av3}) at three segments (L_1, L_2, L_3) of SAP were calculated using Equation 13(Figure 29). Total residence time was calculated using Equation 14, where u_{gas} was obtained by dividing the Q with the cross sectional area of the SAP's inner tube (00182 m).

Equation 11 $$\mathbf{u_{gas_n}} = \frac{\mathbf{Q}}{\mathbf{A}}$$

Equation 12 $$\mathbf{Q} = \frac{\dot{\mathbf{n}} \times \mathbf{R} \times \mathbf{T}}{\mathbf{P}}$$

Equation 13 $$\mathbf{Tav_n} = \frac{\mathbf{T_n} + \mathbf{T_{n+1}}}{\mathbf{2}}$$

Equation 14 $$\mathbf{t} = \frac{\mathbf{L_1}}{\mathbf{u_{gas_1}}} + \frac{\mathbf{L_2}}{\mathbf{u_{gas_2}}} + \frac{\mathbf{L_3}}{\mathbf{u_{gas_3}}}$$

Figure 29. Three Different Segments of SAP.

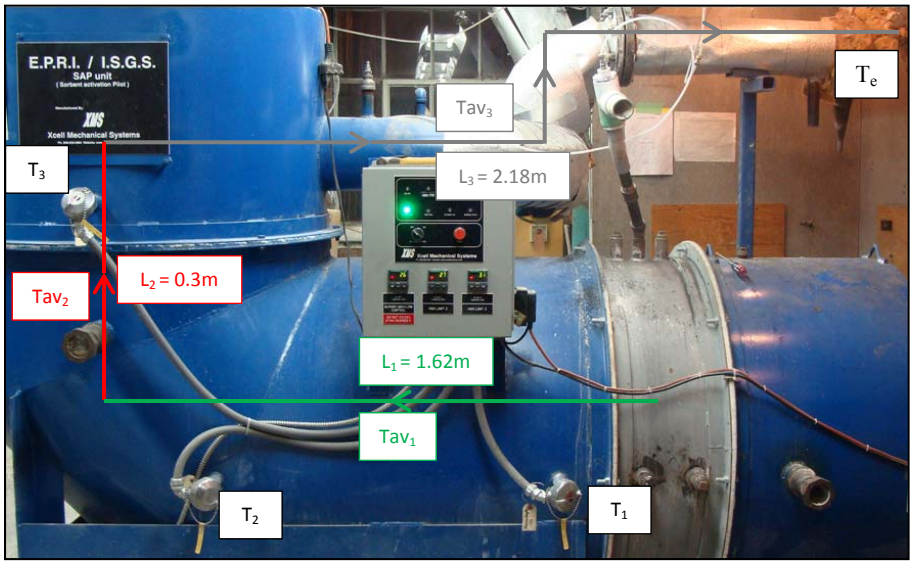

2.2 Kinetics of Thermal Decomposition of Limestone

2.2.1 Non-Isothermal TGA Calcination

The kinetics of thermal decomposition of limestone was determined using non-isothermal TGA data. Kinetic information of a gas-solid reaction can be evaluated either by an isothermal

method or by a non-isothermal TGA technique. In the isothermal technique, conversion-time data are measured at several temperatures. The rate data are interpreted by employing conventional kinetic models (e.g., reversible or irreversible reaction, first or second or n order mechanism) to determine the kinetic parameters (order of the reaction (n), activation energy (Ea), and frequency factor (A)). In the non-isothermal technique, the sample is heated at several linear heating rates in an inert or reactive gas and the weights of the sample (TG) at different reaction temperatures are measured. The weight loss data is numerically differentiated to obtain the rate of weight loss (DTG). The rate data are interpreted by various non-isothermal reaction analysis methods to obtain the kinetic parameters. The non-isothermal technique has several advantages over the isothermal method when determining kinetic information of thermal decomposition of limestone. They include:

a. A wide range of temperature can be covered with a single experiment; thus enabling a rapid calculation of kinetic parameters [Everson, 2006].
b. Reaction data are collected from the onset to the determination of the calcination reaction.
c. The reliability and accuracy of the kinetic model can be evaluated at various heating rates.

In this study, mass and heat transfer limitations during the thermal decomposition of limestone in TGA experiments were not considered. In this research: (i) a small sample mass (<15 mg), (ii) a sufficiently high total purge gas flow rate (100 mL/min), (iii) small limestone particles (particle size < 90 μm) and, (iv) multiple linear heating rates (2, 5, 10 K/min) were used to minimize the impact of mass and heat transfer resistances and heating rate on kinetic parameters [Chan, et al., 1970].

2.2.1.1 Kinetic Analysis of Non-isothermal TGA Data

Thermal decomposition of limestone was assumed to follow a power law kinetic model. When calcination is performed in the presence of CO_2, the recarbonation of lime also occurs (Equation 1). Equation 15 describes the kinetics of this reversible reaction.

Equation 15
$$-\frac{dX_{CaCO_3}}{dt} = k_1 S a_{CaCO_3} - k_{-1} S a_{CaO} P_{CO_2}$$

Where X_{CaCO_3} is the fraction of $CaCO_3$ remaining in the sample (Equation 16) at reaction time t, S is the area at reaction interface (Figure 1); a_{CaCO_3} and a_{CaO} are the activities of $CaCO_3$ and CaO; k_1, and k_{-1} are forward and reverse reaction rate constants (min^{-1}); t is reaction time (minute), P_{CO_2} is the partial pressure of CO_2 in the calcination gas (kPa). X_{CaCO_3} is defined by Equation 16 where M_i and M_f are the initial sample mass and final mass at the termination of reaction, M is the mass remaining at reaction time t; and α is the mass conversion.

Equation 16 $$\mathbf{X_{CaCO_3} = 1 - \frac{Mi - M}{Mi - Mf} = 1 - \frac{Mi - M}{Mi - Mf} = 1 - \alpha}$$

The pressure attributed by solid CaO and $CaCO_3$ is very small and negligible compared to the pressure of CO_2 gas; hence, activities of solid compounds are assumed unity (a_{CaCO_3} and a_{CaO} = 1). By substituting $k_1/k_{-1} = K_{eq} = P_{CO_2}^*$ in Equation 15 and rearranging it, Equation 17 is obtained [Criado, et al., 1995].

Equation 17 for $P_{CO_2} \leq P_{CO_2}^*$ $$\mathbf{-\frac{dX_{CaCO_3}}{dt} = k_1 S \left(1 - \frac{P_{CO_2}}{P_{CO_2}^*}\right)}$$

In limestone calcination, the reaction interface is not well defined and thus the area of reaction interface is neither easily identified nor can be measured. Consequently, it can be assumed that the interface area, S, in Equation 17 is proportional to the mass fraction of $CaCO_3$ remaining, X_{CaCO_3}, at reaction time t [Campbell, 1978]. This proportionality is a variable and is expressed as X^n in Equation 18 where n is the reaction order with respect to X. For simplification, k_1 is rewritten as k. Substituting Equation 16 into Equation 18 would result in Equation 19.

Equation 18 for $P_{CO_2} \leq P_{CO_2}^*$ $$\mathbf{-\frac{dX_{CaCO_3}}{dt} = k X_{CaCO_3}^{\ n} \left(1 - \frac{P_{CO_2}}{P_{CO_2}^*}\right)}$$

Equation 19 for $P_{CO_2} \leq P_{CO_2}^*$ $$\mathbf{\frac{d\alpha}{dt} = k (1 - \alpha)^{n} \left(1 - \frac{P_{CO_2}}{P_{CO_2}^*}\right)}$$

In a CO_2-free environment (P_{CO_2} = 0), the calcination reaction involves only the forward reaction of Equation 1, and Equation 15 reduces to Equation 20.

Equation 20 for $P_{CO_2} \leq P_{CO_2}^*$ $$\frac{d\alpha}{dt} = k\,(1-\alpha)^{n}$$

In a non-isothermal calcination condition, Equation 20 can be described as Equation 21, where β = dT/dt is the constant linear heating rate (K/min). Equation 20 describes thermal decomposition reaction of limestone in absence of mass and heat transfer limitations.

Equation 21 $$\frac{d\alpha}{dt} = \frac{d\alpha}{dT} \times \frac{dT}{dt} = \frac{d\alpha}{dT} \times \beta = k(1-\alpha)^{n}$$

The reaction rate constant (k) in Equation 21 is commonly described by the Arrhenius expression, Equation 22, where A is the frequency factor (min^{-1}), Ea is the activation energy (kJ/mol), T is the reaction temperature (K) and R is the gas constant (8.3136 J mol^{-1} K^{-1}). Ea, A, and n are generally referred to as triplet kinetic parameters and their values are determined from the experimental reaction rate data. By substituting Equation 22 in Equation 21, Equation 23 is obtained.

Equation 22 $$k = A.e^{-\frac{Ea}{RT}}$$

Equation 23 $$\frac{d\alpha}{dT} = \frac{A}{\beta}.e^{-\frac{Ea}{RT}}.(1-\alpha)^{n}$$

Equation 23 is rearranged and integrated with boundary conditions α = 0 at T = T_o and α = α at T = T to obtain Equation 24. T_o is the ambient temperature at the beginning of a TGA experiment and in most cases, it is assumed that the reaction rate is slow at this temperature and, therefore, it can be eliminated (T_o = 0). The right-hand side of Equation 24 does not have an exact analytical solution. Equation 25 is an approximate solution of this equation [Campbell, 1978]. Equation 26 and Equation 27 represent the integral and differential forms of Equation 23 and can be used to determine the kinetic parameters of irreversible calcium carbonate decomposition in a CO_2-free environment using non-isothermal TGA data [Campbell, 1978].

Equation 24 $$\int_0^{\alpha} \frac{d\alpha}{dT}.\frac{\beta}{A}.(1-\alpha)^{-n} = \int_0^{T} e^{-\frac{Ea}{RT}}$$

Equation 25 $$\int_0^{T} e^{-\frac{Ea}{RT}} \cong \frac{RT^2}{Ea}.e^{-\frac{Ea}{RT}}$$

Equation 26 $$\alpha = 1 - \left[\left((n-1).\frac{ART^2}{\beta Ea}.e^{-\frac{Ea}{RT}}\right)+1\right]^{\frac{1}{1-n}}$$

Equation 27 $$\frac{d\alpha}{dT} = \frac{A}{\beta}.e^{-\frac{Ea}{RT}}.\left[\left((n-1).\frac{ART^2}{\beta Ea}.e^{-\frac{Ea}{RT}}\right)+1\right]^{\frac{n}{1-n}}$$

When the calcination is performed in a mixture of N_2 and CO_2 (P_{CO_2} = constant), the thermal decomposition reaction of limestone is reversible (Equation 15). The equilibrium pressure of CO_2, $P_{CO_2}^*$ in Equation 21 is replaced by a temperature-dependent expression presented in Equation 28, where B (kPa) and F (kJ/mol) are constants [Campbell, 1978]. In this study, values of B = 1.87 E+9 kPa and F = 163,760 J/mol were used [Criado, 1995]. Equation 29 and Equation 30 represent general mathematical expressions describing the thermal decomposition of $CaCO_3$ in a CO_2 gas environment.

Equation 28 $$P_{CO_2}^*(kPa) = B \times e^{-\frac{F}{RT}}$$

Equation 29 $$\alpha = 1 - \left[1 + \left((n-1).\frac{ART^2}{\beta}.\left(\frac{e^{-\frac{Ea}{RT}}}{Ea} - \frac{P_{CO_2}\, e^{-\frac{Ea-F}{RT}}}{B(Ea-F)}\right)\right)\right]^{\frac{1}{1-n}}$$

Equation 30 $$\frac{d\alpha}{dT} = \frac{A}{\beta}.e^{-\frac{Ea}{RT}}.\left(1-\frac{P_{CO_2}}{P_{CO_2}^*}\right).\left[1+(n-1).\frac{ART^2}{\beta}.\left(\frac{e^{-\frac{Ea}{RT}}}{Ea} - \frac{P_{CO_2}\, e^{-\frac{Ea-F}{RT}}}{B\,(Ea-F)}\right)\right]^{\frac{n}{1-n}}$$

Equation 30 predicts that the rate of limestone decomposition decreases with increasing the CO_2 partial pressure in the calcination gas at a given reaction temperature. Physically, this can be interpreted as an increase in CO_2 diffusion resistance between the reaction front and the bulk gas. Limestone is thermally decomposed only when the local CO_2 concentration is less than the equilibrium CO_2 partial pressure at a given reaction temperature. Therefore, a higher activation energy and a lower frequency factor are expected when calcination occurs in CO_2.

2.2.2 Determination of Kinetic Parameters

Several non-isothermal TGA kinetic analysis methods including Coats-Redfern (CR), Criado-Linearization, and DTG-curve fitting were employed to determine the kinetic parameters for thermal decomposition of limestone samples.

2.2.2.1 Coats-Redfern Linearization Technique

Coats-Redfern method employs Equation 31 and Equation 32 to determine the kinetic parameters. These two equations are obtained by integrating Equation 23 for n = 1 or n ≠ 1 and rearranging the equations into their linear forms. In the Coats-Redfern method, a reaction order is initially assumed and the experimental data are plotted according to the dictate of either Equation 31 or Equation 32. Iteration of the value of n is performed until the highest correlation coefficient (R^2) of the plot is obtained. A log-log plot of the left hand side of either Equation 31 or Equation 32 against 1/T in the major decomposition stage of limestone (in this study the range was between 10 % and 75 %) is then prepared. The value of (1- 2RT/Ea) in Equation 31 and Equation 32 is relatively constant in most temperature ranges and is substituted by an average temperature representing the temperature range where data are being analyzed.

Equation 31 for n≠1 $$\ln\left[\frac{(1-\alpha)^{1-n}-1}{(n-1)\,T^2}\right]=\ln\left[\frac{A\,R}{\beta\,Ea}\left(1-\frac{2RT}{Ea}\right)\right]-\frac{Ea}{RT}$$

Equation 32 for n=1 $$\ln\left[-\frac{\ln(1-\alpha)}{T^2}\right]=\ln\left[\frac{A\,R}{\beta\,Ea}\left(1-\frac{2RT}{Ea}\right)\right]-\frac{Ea}{RT}$$

From the slope and intercept of these plots, Equation 33 and Equation 34, activation energy and frequency factor are calculated based on Equation 35 and Equation 36.

Equation 33 $$\mathbf{Slope}=\frac{Ea}{RT}$$

Equation 34 $$\mathbf{Intercept}=\ln\left[\frac{A\,R}{\beta\,Ea}\left(1-\frac{2RT}{Ea}\right)\right]$$

Equation 35 $$Ea=Slope\times R\times T$$

Equation 36 $$A=\frac{\exp(\text{Intercept})\times\beta\times Ea}{R\times\left(1-2\frac{RT}{Ea}\right)}$$

One disadvantage of Coats-Redfern method is that it does not utilize rate of weight loss (DTG) data, which is more sensitive kinetic data than TG data, in the data analysis. In addition, when the calcination is performed in CO_2, kinetic parameters calculated by this method incorporate the CO_2 partial pressure effect. Therefore, they represent the apparent kinetic parameters.

2.2.2.2 Criado Linearization Method

Criado linearization method is selected to verify the kinetic parameters obtained by the Coats-Redfern method. It is relatively similar to CR Linearization method. Equation 21 is rearranged and natural logarithms are applied on both sides of the equation to obtain Equation 37. Iteration of the value of n is performed until the highest R^2 value is obtained. The main advantage of Criado-Linearization method is that it utilizes both DTG and TG data in determining the kinetic parameters. In addition, kinetic parameters of limestone decomposition in CO_2 can be investigated by including the (1- P_{CO_2}/ $P_{CO_2}^*$), the recarbonation reaction-term. Therefore, theoretically, intrinsic kinetic parameters of limestone decomposition in CO_2 can be obtained.

Equation 37

$$\ln\left[\frac{\frac{d\alpha}{dt}\quad(1-\alpha)^{-n}}{\left(1-\frac{P_{CO_2}}{P_{CO_2}^*}\right)}\right] = \ln[A] - \frac{Ea}{RT}$$

2.2.2.3 DTG Curve Fitting Method

DTG curve fitting method involves iterating triplet kinetic parameters to minimize the deviations between predicted and experimental results. Rate data described in Equation 27 are generated by assuming a combination of triplet kinetic parameters. The kinetic parameters that minimize deviations (ε) between the predicted and experimental data in Equation 38 are selected. The iteration process is performed using DTG-SIM software developed at Pyrovac Institute, Toronto, Canada [Yang, et al., 2001]. DTG curve fitting is considered a better method than TG curve-fitting method because DTG data are more parameter-sensitive than TG data. As shown in Figure 30, small changes in kinetic parameters can impact the DTG data but not the TG data. The algorithm of DTG-SIM is presented in Figure 31.

Equation 38

$$\varepsilon = \left[\left(\frac{d\alpha}{dt}\right)_{experiment} - \left(\frac{d\alpha}{dt}\right)_{model}\right]^2$$

Figure 30. Impacts of Kinetic Parameters on TG (Equation 26) and DTG (Equation 27) Models.

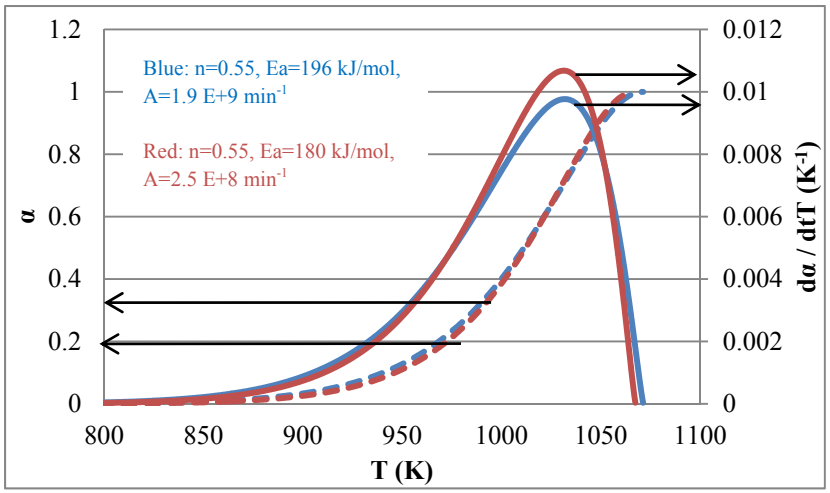

Figure 31. DTG-SIM's Algorithm to Determine the Best Kinetic Parameters [Yang, et al., 2001].

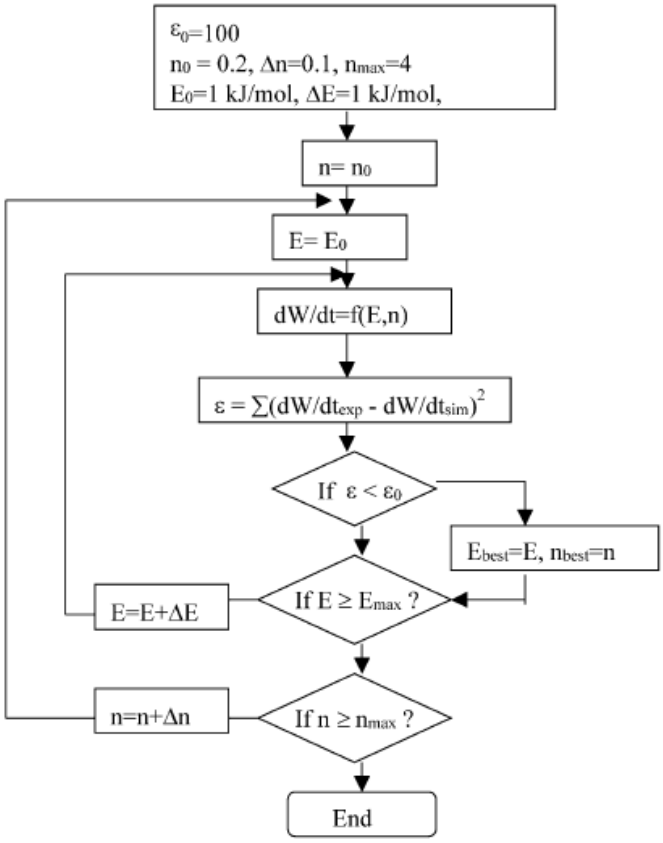

DTG curve fitting has not been used widely because the kinetic parameters obtained with this method are merely curve fitting and may not have meaningful physical interpretation. DTG curve fitting is; however, an adequate and quick technique to predict kinetic parameters that are applicable to this research.

2.2.3 Quantification of Deviation between Predicted and Experimental Data

Equation 39 was used to quantify the deviation between the predicted and the experimental data [Cooper and Alley, 2002], where N is the number of comparable sets of data points used for deviation analysis. In this study, N represents the number of data points collected between EC of 0.15 and 0.75 at each TGA heating rate. The EC range was selected based on values measured in SAP experiments. This deviation represents the inaccuracy of the model predicting the experimental data.

Equation 39

$$\% \text{ Deviation} = \frac{1}{N}\sum \left|\frac{\text{Experimental data} - \text{Model prediction}}{\text{Experimental data}}\right| \times 100\ \%$$

3 RESULTS AND DISCUSSIONS

3.1 Bench-Scale SAP Experiment

Limestone feed rate and carrier nitrogen flow rate, used to feed the limestone particles from AccuRate feeder into the SAP's injection port, were controlled and adjusted, if necessary, during an experiment to minimize fluctuations in the temperature profile inside SAP. The temperature profile and resident time in SAP were controlled by adjusting the propane and air flow rates. SAP was heated to a desired calcination temperature by burning predetermined flows of propane and air. Propane and combustion air flow rates were adjusted to achieve and maintain a desired calcination temperature profile and residence time. Pulverized limestone was fed into SAP through the injecting port at various SAP conditions corresponding to the following temperatures at location T_1: 825, 950, 1,050, 1,120, 1,180, 1,250, and 1,350 K. Temperature at the injection location was typically 10 % higher than at T_1 location which was a distance of 35 cm downstream of the injection port.

The term "equivalence ratio" or ϕ defined by Equation 40 is often used to describe whether the combustion is performed in stoichiometric ($\phi = 1$), or fuel-lean ($\phi < 1$), or fuel-rich condition ($\phi > 1$). It is desired to operate SAP at a fuel-lean condition to completely burn the propane gas; thus, minimize the formation of CO and HCs in the flue gas (Figure 32). For example, in combustion of kerosene ($CH_{1.8}$), formation of NO_x decreases at $\phi < 0.75$, or excess air > 33 % (Figure 33). However, the amount of excess air has to be carefully controlled to maintain the efficiency of the combustion (Figure 32). According to the measured flow rates of propane and combustion air, propane combustion in SAP occurred in fuel-lean conditions at $T_1 <$ 1,250 K and in fuel-rich conditions at $T_1 \geq$ 1,250 K.

Equation 40:

$$\boldsymbol{\phi} = \frac{\left(\frac{\mathbf{n_{fuel}}}{\mathbf{n_{O_2}}}\right)_{\mathbf{actual}}}{\left(\frac{\mathbf{n_{fuel}}}{\mathbf{n_{O_2}}}\right)_{\mathbf{stoichiometry}}}$$

Figure 32. Combustion Efficiency, CO and HCs Concentrations in the Flue Gas at Different O_2 Concentrations in the Flue Gas [Biarnes, 2012].

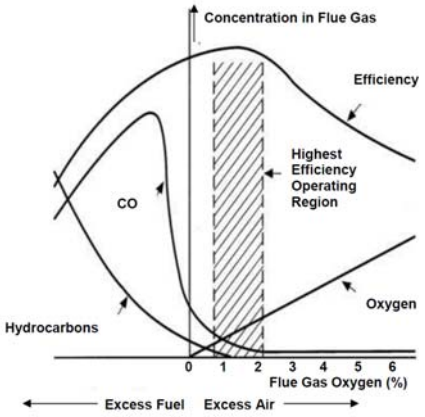

Figure 33. Equilibrium Composition and Temperature of Adiabatic Combustion of kerosene $CH_{1.8}$ at Different Equivalent Ratios [Flagan and Seinfeld, 1988].

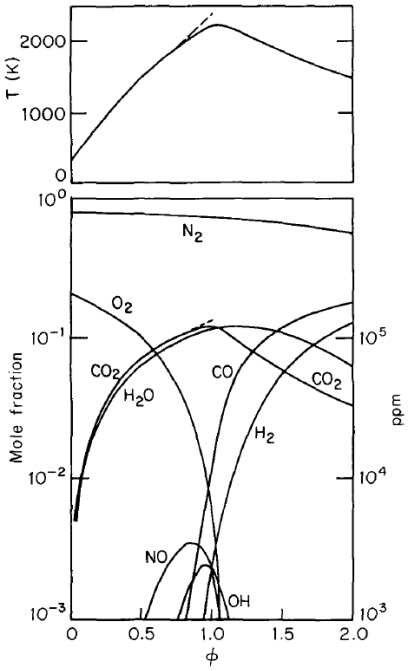

The equilibrium concentrations of NO at different ϕs were calculated at different adiabatic propane flame temperatures and ϕs. By visual observation, the length of the propane flame in SAP was estimated to be 40 cm (the length of combustion chamber where the SAP's burner and flame are located). SAP was assumed to be an adiabatic system. As mentioned before,CHEMCAD 6.4, chemical process simulation software, was employed to predict the total

equilibrium concentrations of NO_x in SAP flue gas at various ϕs. Figure 34 shows the predicted equilibrium concentrations and the measured concentration of NO_x. The gas analyzer was calibrated by the manufacturer prior to its use in this study. Hence, the measured concentrations should be reliable. The measured concentrations were smaller than the calculated equilibrium concentrations at ϕ between 0.6 and 1.3.

Figure 34. Comparisons between Predicted Equilibrium Concentrations and Measured Concentrations of NO_x in SAP Flue Gas at Different ϕs.

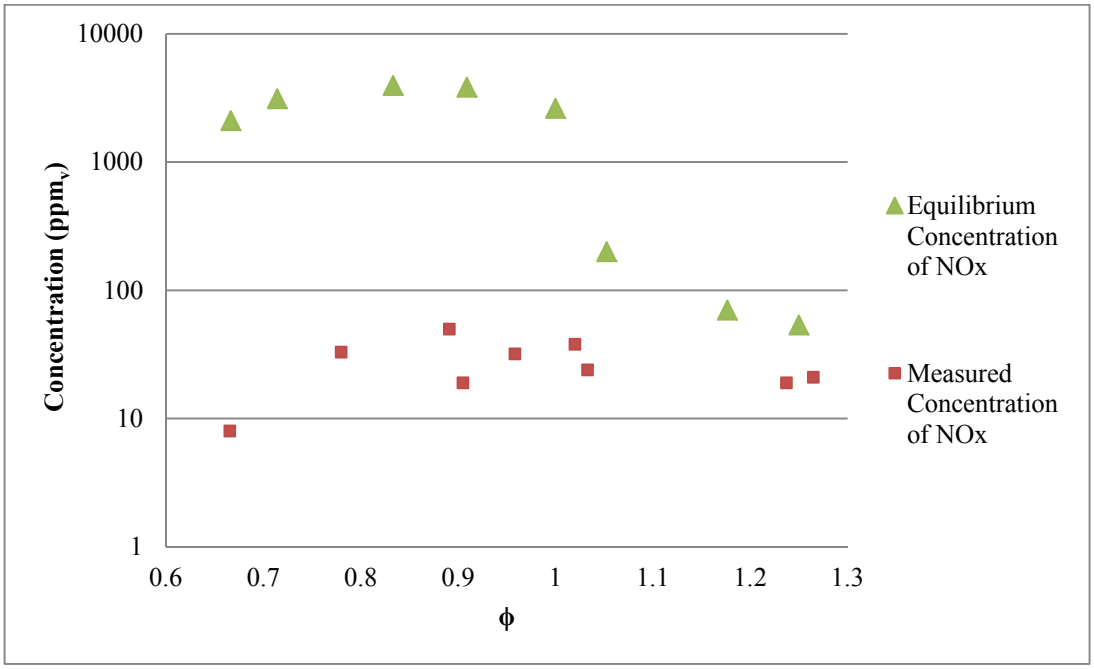

The equilibrium and measured concentrations of CO at various ϕs are presented in Figure 35. The measured concentrations of HCs in the SAP flue gas are also presented in Figure 35. CO was not detected in the flue gas by the gas analyzer used in this study at $\phi < 1$. The measured concentrations of CO were lower than the equilibrium concentration of CO at ϕ between 0.6 and 1.3. HCs were not detected in the flue gas by the gas analyzer used in this study even at $\phi > 1$. CHEMCAD could not be used to model the concentration of HCs because of the complexity of HC radical formation during the combustion process.

The measured concentrations of NO_x and CO were lower than their predicted equilibrium concentrations at ϕ between 0.6 and 1.3. These observations suggest that: 1) SAP is not an

adiabatic system, 2) gas mixing in SAP is not ideal, and 3) the measured concentration values are not realistically characterizing the actual values in the SAP.

Figure 35. Comparisons between Predicted Equilibrium Concentrations of CO and Measured Concentrations of CO and HCs at Different ϕs.

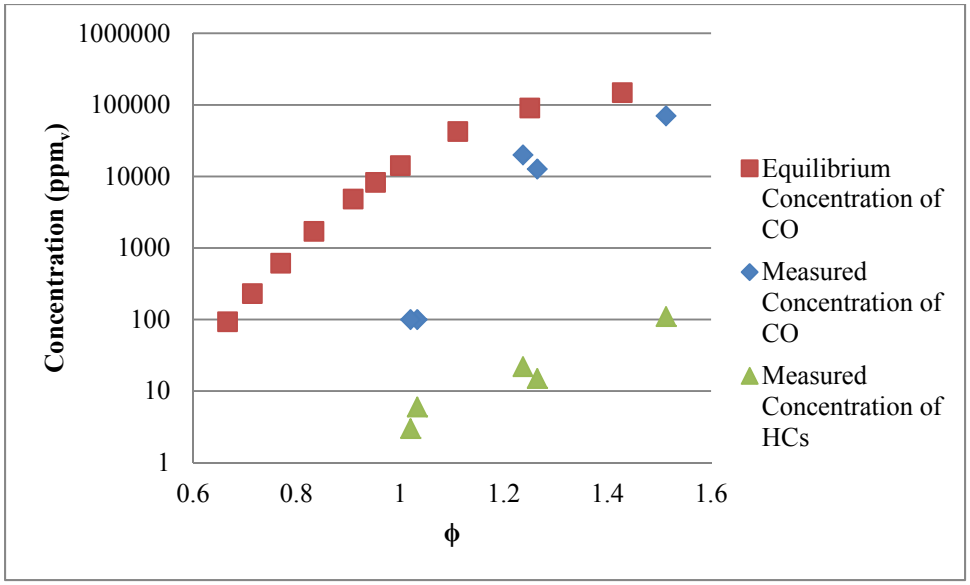

Based on the flow rates of propane and combustion air, the average and standard deviation of ϕ was calculated to be 0.876 ± 0.157 for all SAP tests, corresponding to an average excess air of 14 % (Equation 42). On the other hand, the average concentration of CO_2 in the flue gas detected by the gas analyzer in SAP tests was 8.8 % which corresponded to 28 % excess air (Equation 43) according to Table 4. CO_2 concentration was used to determine the average excess air instead of O_2 concentration because it was considered to be more accurate parameter since air leaks in the gas sampling line could have impacted O_2 measurements. This discrepancy might be due to the fluctuations or inaccuracy in measuring air and propane flow rates. The complete propane combustion did not very likely to occur because at fuel-rich condition (ϕ = 1.05 and 1.25), 11 and 1.2 % O_2 were detected in the SAP flue gas.

Equation 41: $C_3H_{8\,(g)} + 5\,(O_{2\,(g)} + 3.76\,N_{2\,(g)}) \rightarrow 3\,CO_{2\,(g)} + 4\,H_2O_{\,(g)} + 18.8\,N_{2\,(g)}$

Equation 42: $C_3H_{8\,(g)} + 5.7\,(O_{2\,(g)} + 3.76\,N_{2\,(g)}) \rightarrow 3\,CO_{2\,(g)} + 4\,H_2O_{\,(g)} + 0.7\,O_{2\,(g)} + 21.4\,N_{2\,(g)}$

Equation 43: $C_3H_{8\,(g)} + 6.4\,(O_{2\,(g)} + 3.76\,N_{2\,(g)}) \rightarrow 3\,CO_{2\,(g)} + 4\,H_2O_{\,(g)} + 0.7\,O_{2\,(g)} + 24\,N_{2\,(g)}$

Gas-phase residence time and limestone particle terminal settling velocity were calculated based on the flow rates of gaseous products from complete combustion of propane to CO_2 and H_2O. Table 5 includes the properties of the flue gas and residence times based on 14 % excess air as determined by the propane and combustion air flow rates. The gas phase residence times when propane was combusted with 28 % excess air as determined by the concentration of CO_2 in the propane combustion flue gas, were calculated by assuming constant propane flow rate and temperature profile and found to be 10 % shorter than the values in Table 5.

Velocities of the combustion gas and Reynolds numbers, calculated using Equation 12 and Equation 7 at T_1 for different SAP conditions tested, are also provided in Table 5. The flow is considered laminar when the Re is below 2,300; transitional if it is between 2,300 and 4,000; and turbulent if it is above 4,000 [Cooper and Alley, 2002]. The flow in SAP was laminar when T_1 was above 1,050 K. Limestone/lime particle residence time in SAP was calculated using Equation 14 and ranged between 2 and 5 seconds depending on the operating conditions of SAP. Typically a shorter residence time was resulted when the SAP was operated at a higher temperature.

Table 5. Flow Variations in Bench-Scale SAP Reactor at Different Temperature Profiles.

T_1 (K)	u_{gas} (m/s)	Viscosity (kg m^{-1} s^{-1})	Density (kg/m^3)	Reynolds Number	Residence Time (s)	Type of Flow
840	1.41	3.69E-05	0.412	2,399	4.86	Transitional
950	1.74	4.00E-05	0.364	2,413	4.01	Transitional
1,050	1.89	4.32E-05	0.329	2,194	3.73	Laminar
1,120	1.67	4.46E-05	0.313	1,786	3.57	Laminar
1,180	2.02	4.62E-05	0.294	1,959	3.27	Laminar
1,250	2.24	4.81E-05	0.275	1,952	3.04	Laminar
1,350	2.44	5.01E-05	0.257	1,908	2.60	Laminar

Terminal settling velocity of a 40 μm limestone particle at different T_1 was calculated and compared to the gas velocity during all SAP tests (Figure 36). This terminal settling velocity was calculated based on the gas composition obtained when burning propane with 14 % excess of air. According to the particle size distribution data shown in the next section, only < 5 % of sample MSS-LS and < 2 % of sample MRC-LS are > 40 μm. The gas velocity in SAP (1 – 3 m/s) was always an order magnitude higher than the terminal settling velocity (0.1 – 0.4 m/s) of 40 μm limestone particle in all SAP tests. However, experimental observations revealed that some limestone/lime particles settled in some SAP tests. The amount of particles settled during SAP tests could not be quantified experimentally.

Theoretical calculations were made to quantify the extent of particle settling in SAP. An estimate of particle settling was obtained by assuming the 3 sections of SAP (the 1st 1.5 m horizontal section from injection location to the 1st 90° elbow, the 1 m vertical section between the 1st and 2nd 90° elbows, the 2nd 2.71 m horizontal section from the 2nd 90° elbow to the sampling location) as 3 equal-cross-sectional-area laminar gravitational settling chambers (height and width of 15.24) in series (Figure 29). Calculations were made for particle size of 10, 20, 30, and 40 μm and SAP's T_1 temperature between 800 and 1,300 K (Figure 34). In most SAP tests, the gas flow was laminar.

Theoretically, limestone particles ≥ 40 μm would settle in SAP. Furthermore, for particle < 40 μm, the extent of particle settling decreased with increasing SAP's T_1 temperature. As will be discussed in Section 3.2.1, particle size distributions of the feed limestone and lime products collected in the SAP's cyclone were comparable by author's visual observation, suggesting that: 1) particles collected in cyclone for EC analysis were representative of the injected limestone particles, and 2) the theoretical calculations of particle settling in a gravitational chamber overestimated the extent of particle settling. Future work is required to more accurately quantify the extent of particle settling in SAP.

Figure 36. Comparisons of Terminal Settling Velocity of a Limestone Particle with 60 µm Particle Size and Gas Velocity at Different Temperatures.

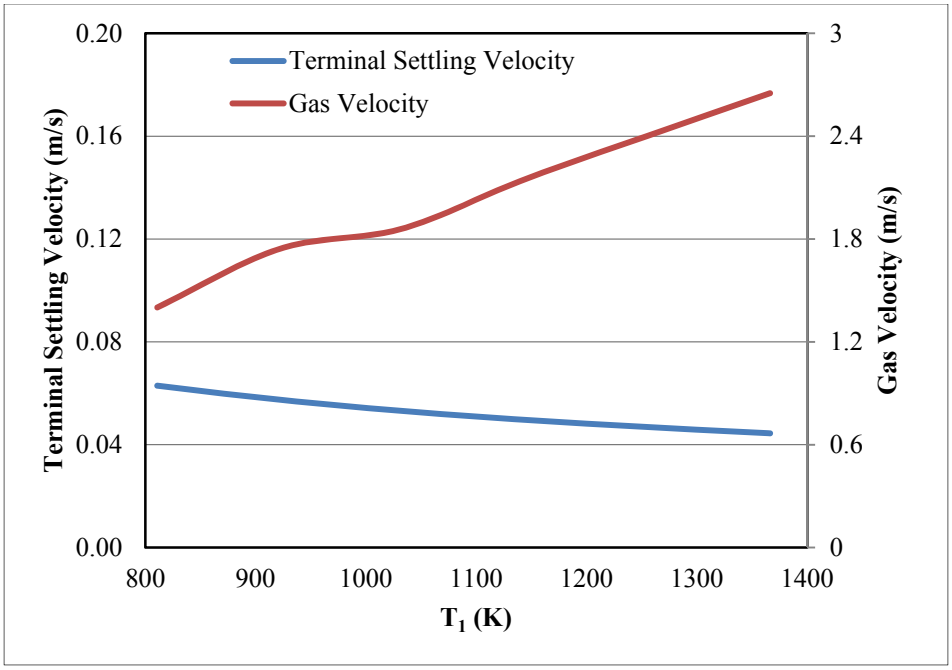

Figure 37. Extent of Particle Settling at Different Temperature Profiles in SAP.

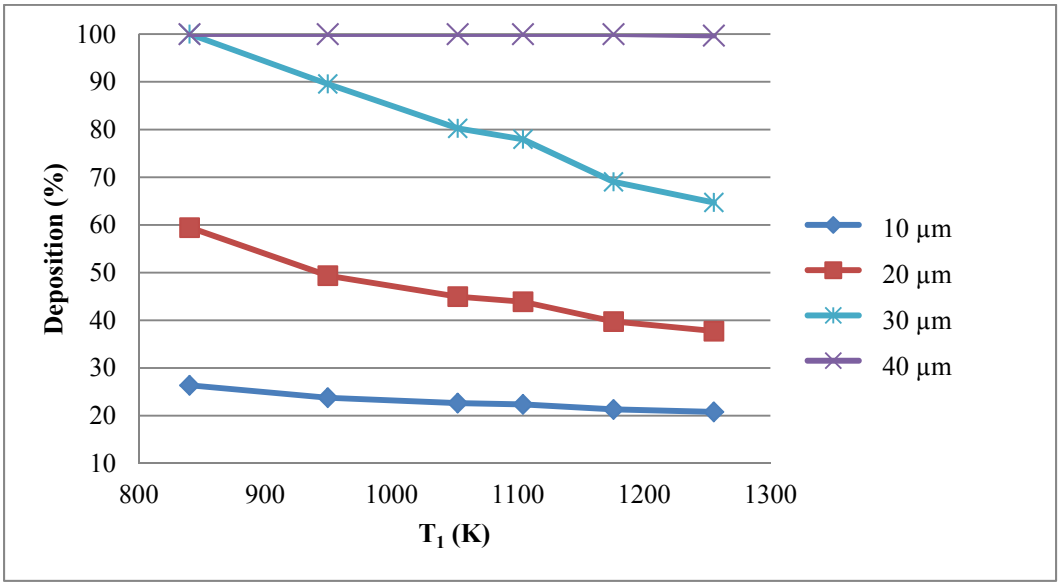

Temperature and partial pressure of CO_2 in the calcination gas impact the rate and EC of limestone and recarbonation of lime. Temperature profile in SAP will help determine calcination and recarbonation zones. As was mentioned earlier, the average partial pressure of CO_2 in the

SAP gas was calculated to be 10 kPa (at 14 % excess of air). According to the equilibrium curve of limestone calcination (Figure 2), when CO_2 pressure is 10 kPa, the calcination reaction will take place at above 1,025 K. Figure 38 shows temperature profiles at different locations in SAP. A higher temperature profile could be achieved either by burning more propane at constant air flow rate (in fuel-lean combustion case) or decreasing the amount of excess air at constant propane flow rate (in fuel-rich combustion case). As previously mentioned, the temperature at the injection port was only measured occasionally using portable thermocouple. Typically, it was 10% higher than the temperature at T_1 location. The intersections of the horizontal red line with the temperature profile plots in Figure 38 mark the locations (or particle residence time) in SAP during which calcination of $CaCO_3$ and recarbonation of CaO occured. The calcination reaction thermodynamically could only occured at SAP conditions above the red line while at conditions below the red line, the recarbonation reaction occured.

Figure 38. Temperature Profiles in Bench-Scale SAP at Various Operating Conditions.

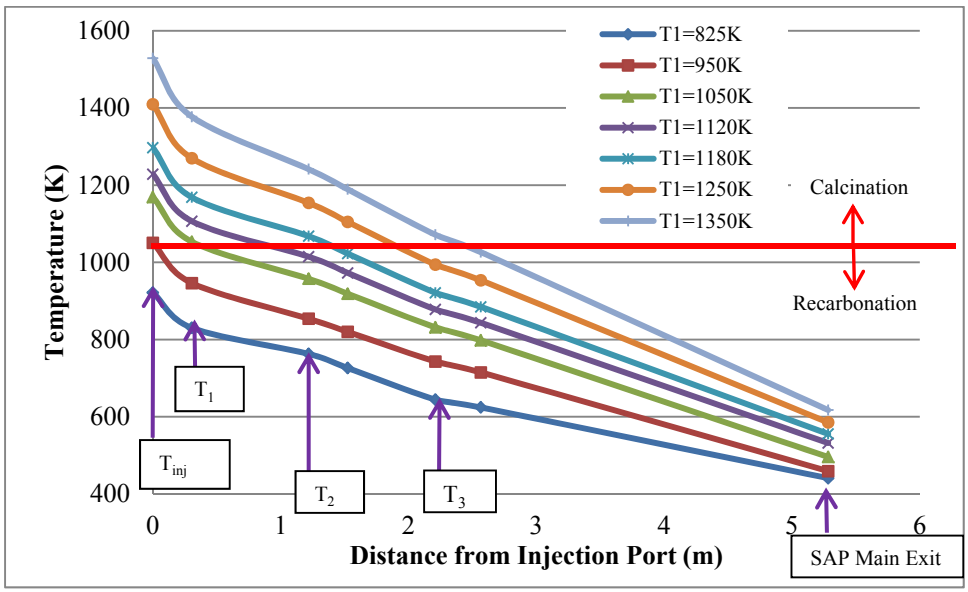

Lime products were collected using the involute cyclone at the exit of SAP. The particle collection efficiency of this particle collection system could not be experimentally determined. The inlet gas flow into the cyclone was perpendicular to the direction of the exit gas flow. Increasing temperature drop as going downstream of SAP caused the temperature at the outlet of SAP to be higher than the temperature at the cyclone. Hence the sampling velocity was higher than the SAP gas velocity which makes the sampling was not isokinetic. In this case,

theoretically, a larger weight fraction of heavier particles than the lighter particles would be collected in the cyclone [SIGRIST, 2012].

Lime samples collected in the cyclone were tested with the TGA to measure the EC of a sample. The EC was correlated with temperatures at T_1 location at each SAP test conditions (Figure 39). The value of T_1 was used mainly because the temperature at this location was monitored continuously during SAP experiments and was more stable than the temperature at the limestone injection port. Figure 39 reveals that limestone calcination occurred at test conditions T_1 = 825 and 950 K. These temperatures are lower than the equilibrium temperatures for thermal decomposition of limestone at 10 kPa CO_2 (Figure 2). This observation indicates that either limestone particles were exposed to a higher temperature than measured at the injection port, due to the heat radiation effect from the propane flame or the inner walls of SAP, or the possibility that CO_2 concentration inside SAP was non uniform and in some locations below 10 kPa due to non-ideal gas-gas and gas-solid mixing.

Figure 39. EC of Lime Sorbents Produced from MSS-LS (Blue) and MRC-LS (Orange) at Different T_1.

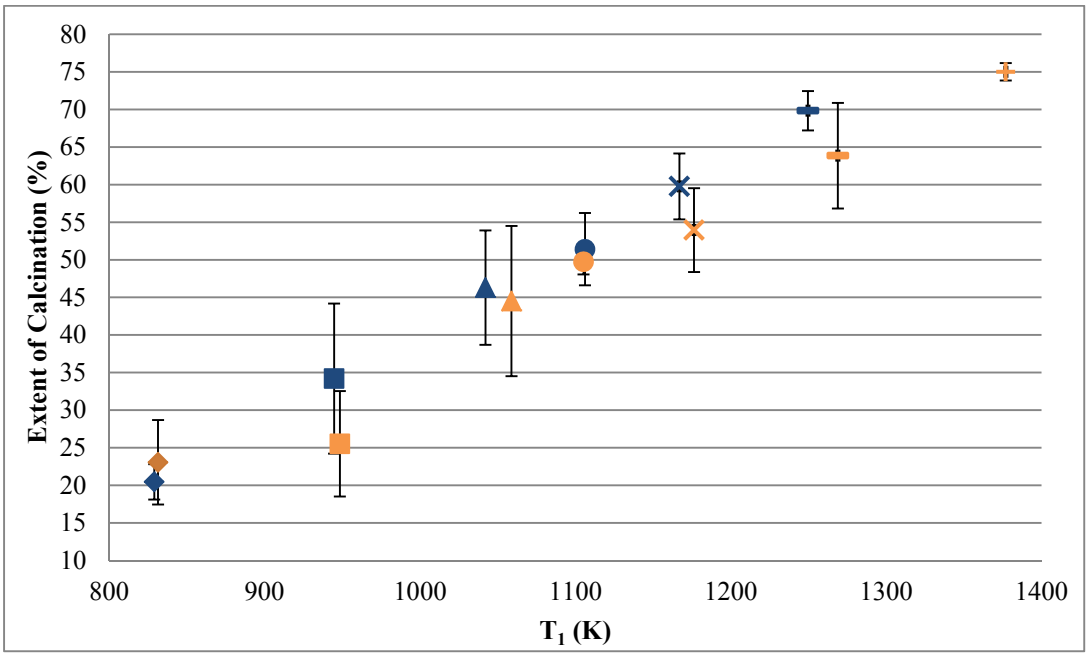

Adiabatic flame temperatures of propane combustion at various levels of excess air were also predicted using CHEMCAD 6.4 software and manual calculation and the results are

presented in Figure 40. The blue triangles represent the predicted adiabatic propane flame temperatures based on the assumptions of complete propane combustion and ideal gas mixing with no CO, NO_x, or HCs formation. The red squares represent the predicted adiabatic flame temperatures by considering CO and NO_x formations using CHEMCAD 6.4. The calculated temperatures using CHEMCAD are more representative of adiabatic flame temperatures in SAP due to the consideration of CO and NO_x generated during the propane combustion. Adiabatic flame temperatures increased from 1,500 to 2,275 K with increasing ϕ increased between 0.5 and 1. When ϕ > 1, they decreased from 2,275 to 1,900 K as ϕ increased from 1 to 1.7. The average and standard deviation ϕ in all SAP tests were 0.876 ± 0.157 corresponding to adiabatic flame temperatures between 1,825 and 2,225 K at ϕ between 0.62 and 1.03. The temperatures at the injection port in all SAP tests were between 860 and 1,540 K. Hence, the temperature difference between the two locations (the combustion chamber where the flame was located and the injection port) could have created a thermal radiation effect, causing the injected limestone particles to have higher temperatures than the measured gas temperatures (T_{inj}, T_1, T_2, T_3, and T_{exh}). A computational flow dynamic (CFD) simulation modeling will be necessary to gain more insight on gas-solid flow patterns and temperature fields in SAP to better address this phenomenon.

Figure 40. Predicted Adiabatic Propane Flame Temperature at Different ϕs.

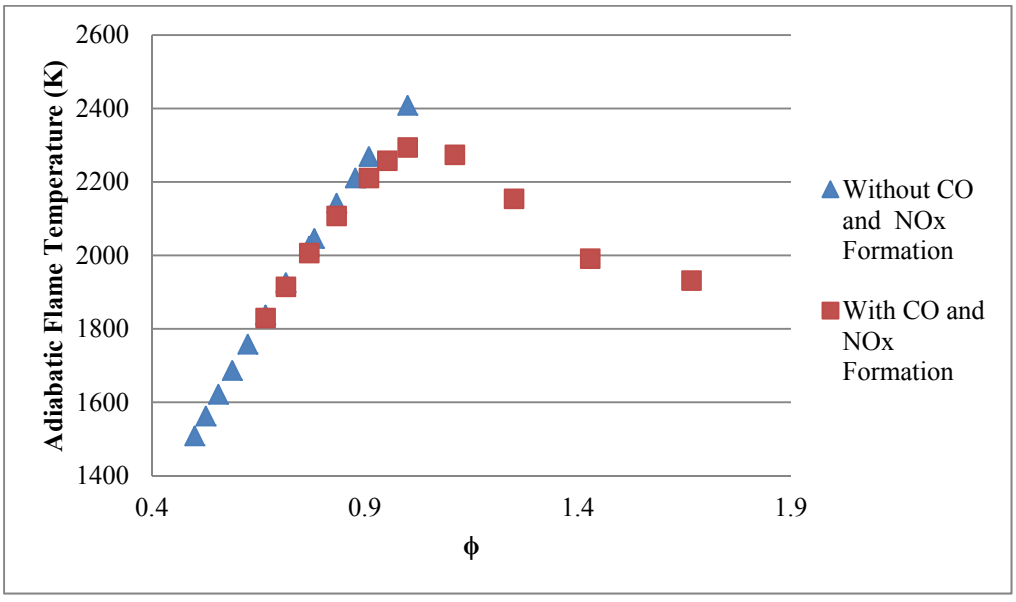

As shown in Figure 39, the temperature profile in SAP impacted the EC. Each data point in Figure 39 represents at least the average value of three SAP tests with the error bar showing the range of the measured values. The variability in the EC is below 25 %. The EC increased from 20 to 75 % with increasing T_1 temperature between 540 and 1,350 K. Theoretically, a higher calcination temperature and a longer residence time should result in a higher EC. However, higher ECs were obtained at higher T_1 even though at $T_1 < 1{,}250$ K (fuel-lean combustion), the gas residence time decreased with increasing T_1 while at $T_1 > 1{,}250$ K (fuel-rich combustion) the gas residence time increased with increasing T_1. Hence, it can be concluded that temperature had a stronger impact than residence time on EC. The temperature profile and particle residence time in SAP could not be controlled independently because obtaining a desired temperature profile was only possible by adjusting the propane and combustion air flow rates. As was previously noted, a shift to a higher temperature profile was obtained either by burning more propane, which consequently increased the gas-phase velocity and reduced particle residence time (fuel-rich combustion), or by reducing the amount of excess air (fuel-lean combustion) which resulted in increasing the gas residence time.

The variability in the EC generally decreased at higher T_1. According to the data of Figure 39, lime samples prepared from MSS-LS and MRC-LS at T_1 of 825, 950, and 1,050 K have standard deviations between 19 and 25% compared to an average standard deviation of 7-8% for the remaining samples. This variability could be explained by the manner in which SAP tests were performed. A calcination test involved: 1) heating the SAP initially to the lowest T_1 test conditions, 2) performing the calcination test at this temperature, 3) increasing the T_1 to the next set point, and 4) performing another calcination test. This procedure was repeated until the calcination test was performed at the highest T_1 test conditions. The variability in the EC observed at the lower T_1s suggests that the SAP system had not reached thermal equilibrium when these tests were performed; thus, causing fluctuations in the temperature profile. The temperature profile became more stable as SAP was heated for a longer period of time to a higher T_1.

The surface area of the lime produced from sample MSS-LS increased from 3 to 6 m^2/g with increasing T_1 between 840 and 1,200 K and decreased to 4 m^2/g at 1,277 K (Figure 41, blue symbols). A similar trend in surface area development was observed for sample MRC-LS;

however, the surface area of this lime was two times higher than the one developed from the calcination of sample MSS-LS (Figure 41, orange symbols). Results presented in Figure 41 indicate that both the calcination temperature and properties of limestone influenced the surface area development in quicklime with the former parameter having a stronger impact.

It is likely that the observed decrease in the surface area at T_1 above 1,200 K cannot be attributed to insufficient residence time of calcination because as was shown in Figure 39, the EC increased with increasing T_1. It is likely; however, that sintering phenomenon occurred during limestone calcination above 1,200 K and the rate of sintering of lime exceeded the rate of surface area development. This conclusion is in agreement with Borgwardt's experimental results which indicate that the rate of sintering of CaO becomes significant above 1,013 K [Borgwardt, 1989b]. Surface area of quicklime derived from both limestone samples at T_1 above 1,250 K were between 25 to 33 % lower than the maximum surface areas.

Figure 41. Total Surface Area of Lime Produced from MSS-LS (Blue) and MRC-LS (Orange).

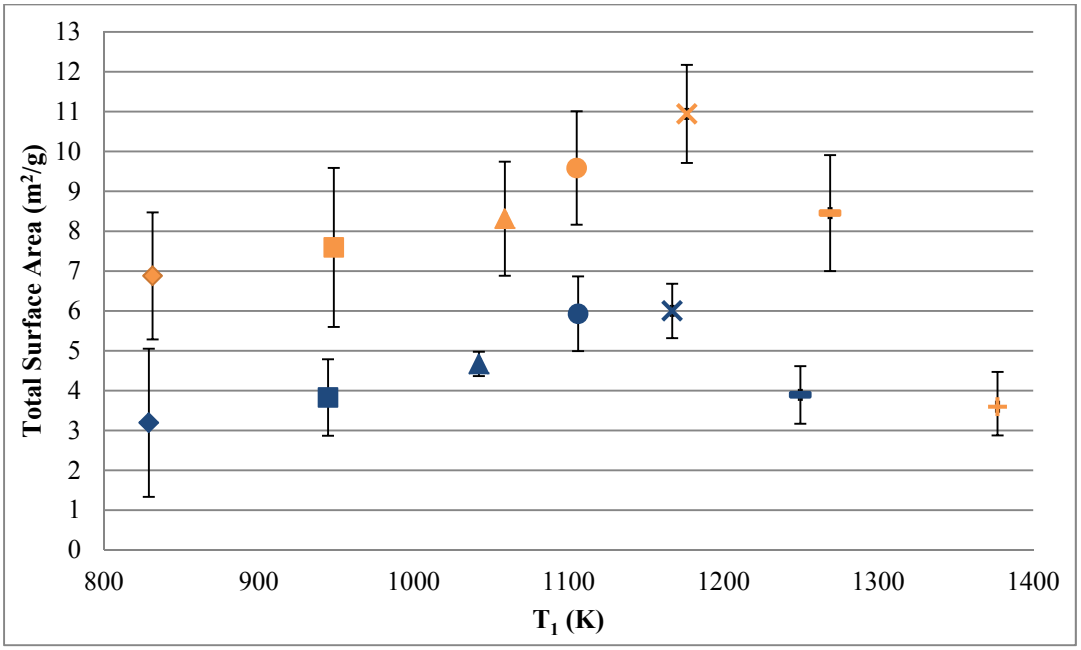

Commercial lime samples (Standard Quicklime and Pulverized Quicklime) were obtained from Mississippi Lime Company. The ECs and surface areas of these samples were tested and found to be > 95 %, if not 100 %, and < 2.74 m^2/g. Hence, the surface area of these quicklime samples represents the surface area of only the CaO. Therefore, to equally compare the SAP

quicklime to these commercial quicklime samples, the surface area of the SAP quicklime was reported on the basis of its calcium oxide content. The surface area of carbonate-free SAP limes were calculated using Equation 44 and are shown in Figure 42. The average surface area of a carbonate-free lime generated from calcination of sample MSS-LS was between 5 and 17 m^2/g and that of sample MLC-LS was between 5 and 37 m^2/g (Figure 42).

Equation 44:
$$\textbf{Carbonate} - \textbf{Free Surface Area} = \frac{\textbf{Total Surface Area}}{\textbf{Extent of Calcination}}$$

Figure 41 shows that the highest total surface area was obtained for the products of both limestone samples when T_1 was between 1,100 and 1,200 K, while the highest carbonate-free CaO surface area was obtained at lower temperature profiles when T_1 ranged between 800 and 1,000 K. According to Powel and Searcy, CaO formed at temperatures below and above 1,000 K exhibited different surface areas and morphologies [Powell and Searcy, 1982].

Figure 42. Carbonate-Free Surface Area of Carbonate-Free Limes Produced from MSS-LS (Blue Symbols) and MRC-LS (Orange Symbols).

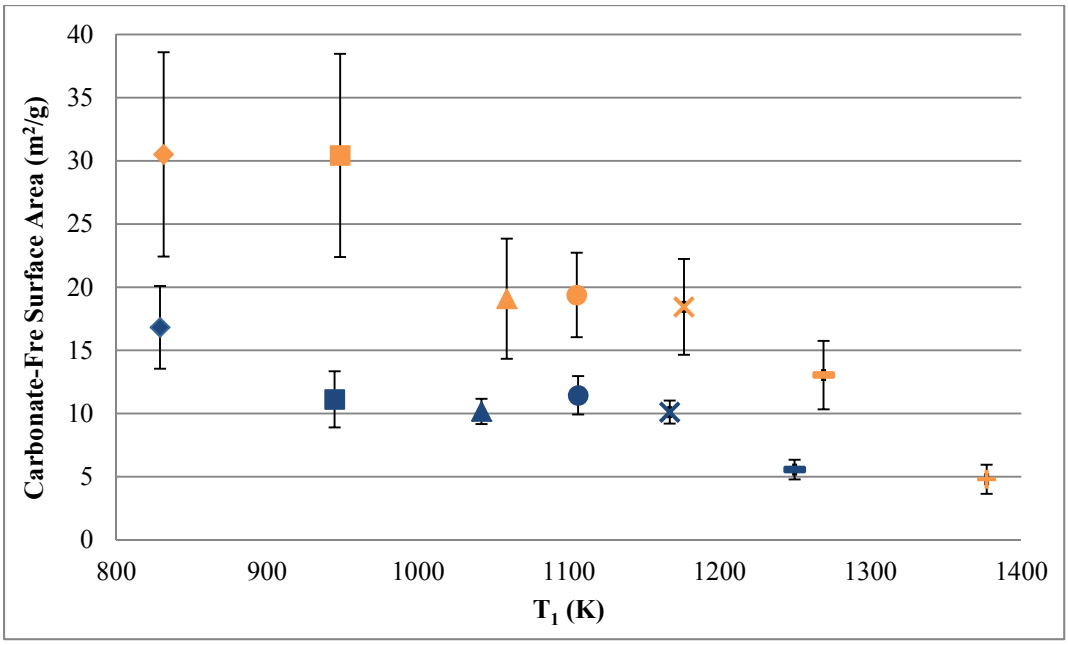

Data presented in Figure 39 to Figure 42 should be interpreted with caution because the hydrodynamics of the flow, gas-gas and gas-solid mixing, particle agglomeration, gas-phase temperature distribution, lime grain sintering, and particle settling in SAP were neither

considered nor quantified to assess their impacts on the EC of limestone and surface area development in lime. Future work with the SAP should address these issues.

3.2 Characterization of Limestone and Lime Products

3.2.1 Particle Size

As previously mentioned, particle size of limestone impacts the calcination performance. A smaller particle tends to produce a larger surface area and a higher EC, but also experiences more sintering [Borgwardt, 1985]. Results from a series of SAP screening experiments with Z7 limestone (properties not listed here) obtained from Chemical Lime Company in St. Genevieve, MO, showed that the EC and surface area of the product lime were not affected by the limestone particle size between 9 and 42 µm (Figure 43).

Figure 43. (a) Extent of Calcination and (b) Surface Area of lime produced from Z7 Limestone.

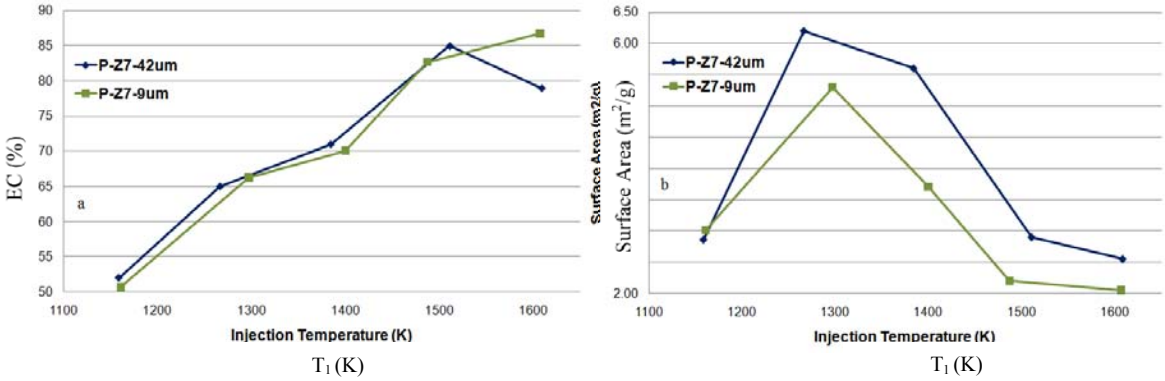

Figure 44 and Figure 45 represent the particle size distributions of sample MSS-LS and sample MRC-LS. The particle size distributions are bimodal with a minor peak at 0.8 µm, a major peak at 15 µm, and comparable particle size distributions between 0.3 and 80 µm size ranges. > 95 wt % of sample MSS-LS and > 98 wt % of sample MRC-LS were < 40 µm. Figure 46 to Figure 49 show the particle size distributions of the lime products produced at different T_1 conditions from sample MRC-LS. They are nearly comparable to those of the feed limestone. According to the particle size distribution data, the minor peak observed for the limestone at 0.8 µm was replaced with a minor peak at 0.3 µm and the peak at 15 µm was shifted to 10-12 µm. In addition, particles between 1 and 3µm in the raw limestone samples were shifted to smaller sizes in the lime products, partially because limestone particles were subjected to some degree of

grinding during feeding into the SAP. Moreover, it is possible that flash release of CO_2 from limestone particle during the calcination created void spaces in particles which made them more vulnerable to fragmentation when they collided with other particles or the interior wall of SAP.

Figure 44. Particle Size Distribution of Sample MSS-LS before Injection to SAP.

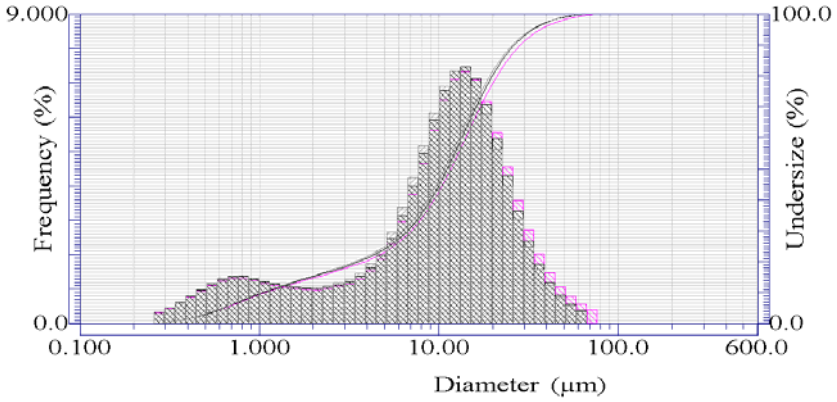

Figure 45. Particle Size Distribution of Sample MRC-LS before Injection to SAP.

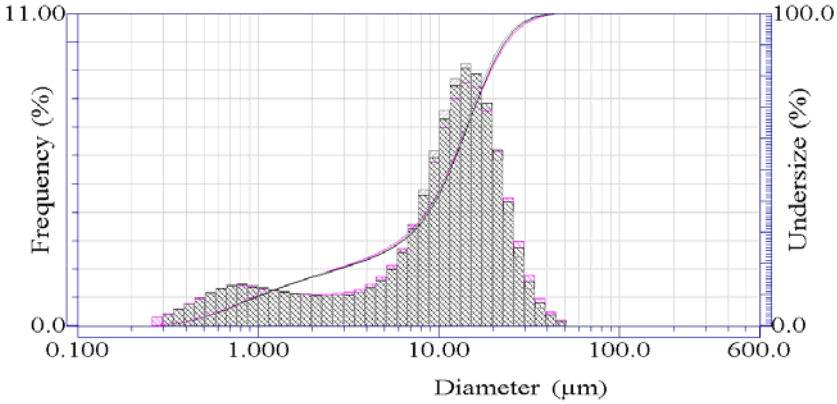

Figure 46. Particle Size Distribution of Sample MRC-LS Calcined in the SAP at 825 K.

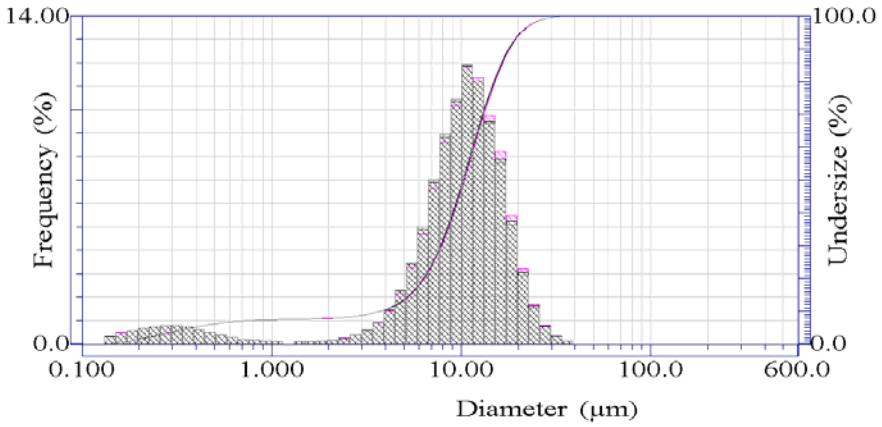

Figure 47. Particle Size Distribution of Sample MRC-LS Calcined in the SAP at 950 K.

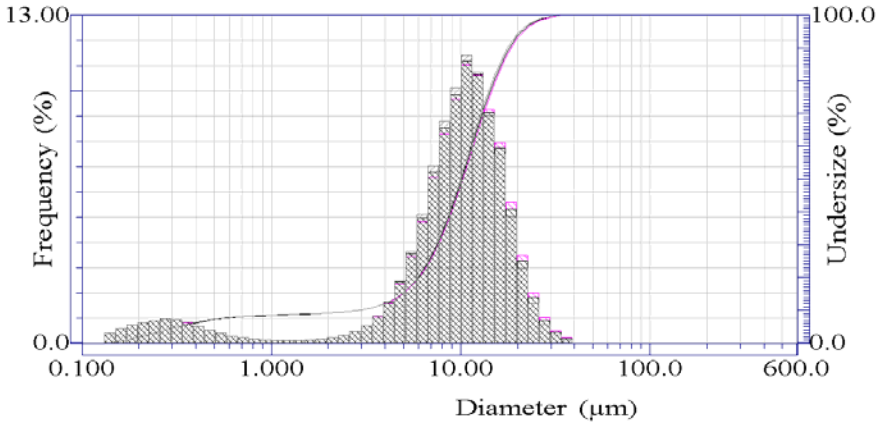

Figure 48. Particle Size Distribution of Sample MRC-LS Calcined in the SAP at 1,050 K.

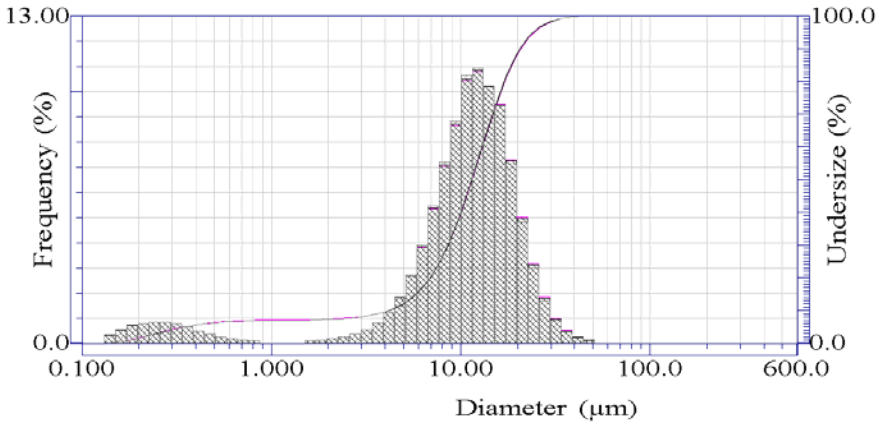

Figure 49. Particle Size Distribution of Sample MRC-LS Calcined in the SAP at 1,120 K.

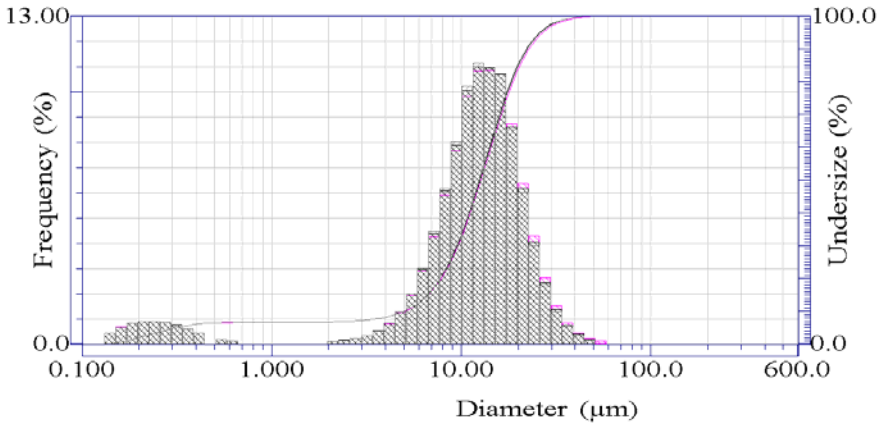

3.2.2 Surface Morphologies

As previously mentioned, calcination conditions including temperature, residence time, and gas environment significantly impact the surface morphology of lime [Borgwardt, 1989a, 1989b, Oates, 1998, and Silcox, et al., 1989]. SEM images were obtained for samples MRC-LS and MSS-LS (Figure 50) and their corresponding lime products calcined at 1,180 K in SAP (Figure 51), at 1,550 K in SAP (Figure 52a) and at 1,273 K for 12 hours using N_2 in an electric furnace (Figure 52b). The morphologies of limestone and quicklime shown in Figure 50 to Figure 52 are visually similar to those reported in the literature (Yu, et al., 2010; Singh and Singh, 2007). In Figure 50, sample MRC-LS appears to have a rougher surface than sample MSS-LS. Lime products produced from sample MRC-LS were more porous and sparser than those prepared from sample MSS-LS (Figure 51). Lime produced after 2 hours calcination in N_2 in the electric furnace at 1,273 K was less porous and had a smoother surface than the lime produced in the SAP at T_1 = 1,550 K, P_{CO_2} = 10 kPa and residence time of < 5 seconds (Figure 52). The lime prepared in the electric furnace was more sintered and its surface area (1.91 m^2/g) was smaller than the lime prepared in SAP (4.15 m^2/g).

Figure 50. SEM Images of a) Raw MSS-LS and b) Raw MRC-LS.

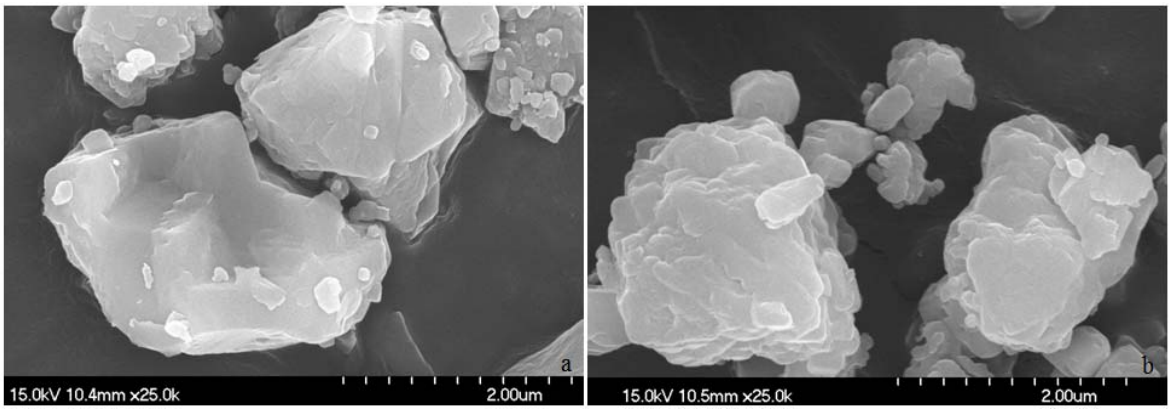

Figure 51. SEM Images of Lime Product from Calcination of a) Sample MSS-LS and b) Sample MRC-LS at 1,180 K in the SAP.

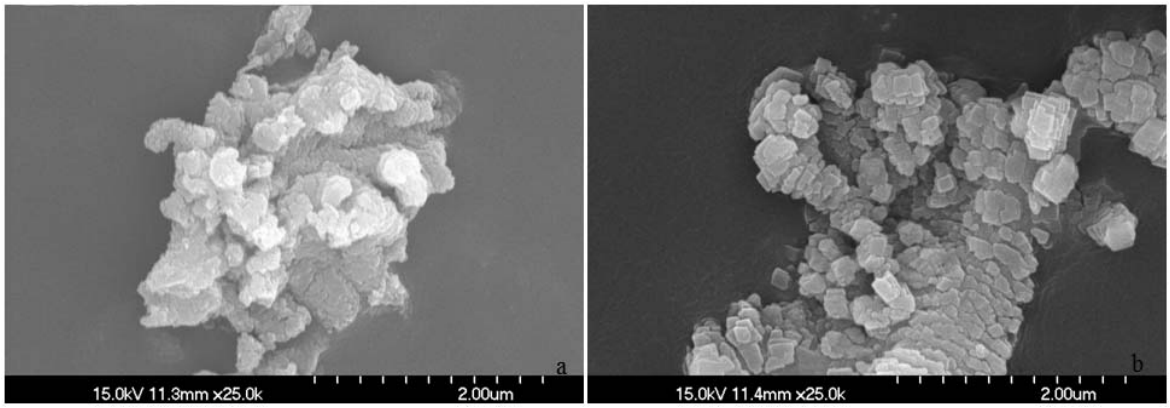

Figure 52. SEM Images of Limes Produced from Calcination of Sample MRC-LS a) SAP at 1,550 K, b) Batch Reactor at 1,273 K in N_2.

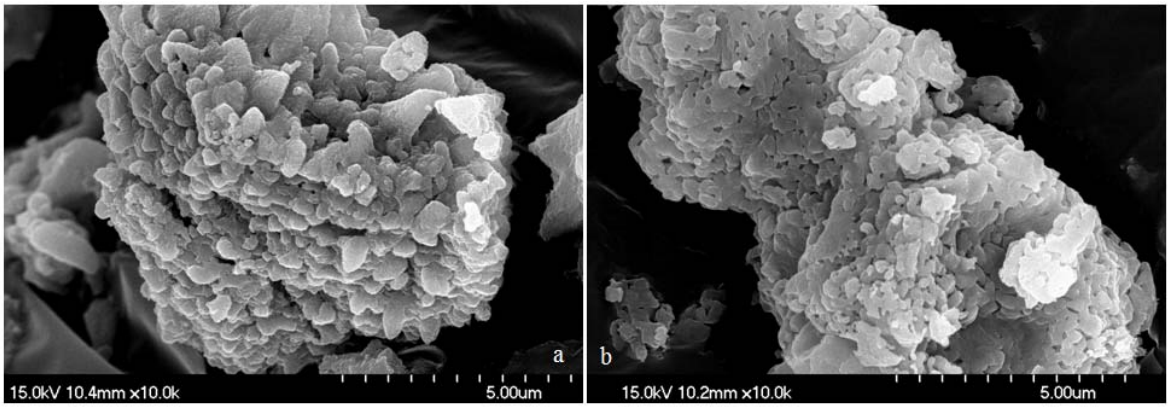

3.3 Calcination Kinetics

The kinetics of limestone decomposition is needed to describe the rate and EC during limestone calcination. The intrinsic kinetics data can be combined with a transport modeling to predict the calcination performance of a limestone particle in a rotary kiln under slow heating conditions or in an entrained-flow reactor under fast (flash) calcination conditions. In this work, calcination kinetics were determined by analyzing the thermal decomposition data of the two limestone samples obtained under linear heating rates in N_2 and CO_2 using a TGA. As previously mentioned the importance of mass and heat transfer limitations on the calcination reaction is greatly influenced by particle size of the limestone [Khinast, et al., 1996; Hu and Scaroni, 1996; Fuertes, et al., 1993]. For limestone particles < 90 μm particles, the size range used in this work, mass and heat transfer limitations have been shown to have little impact on the calcination reaction [Beruto and Searcy, 1974; Borgwardt, 1985]. As will be described in the next section, heat transfer calculations showed that under SAP experimental conditions, heat transfer limitations in limestone particles were negligible.

3.3.1 Temperature Profile in a 80 μm Limestone Particle in SAP

General plots describing the solutions to unsteady-state heat transfer for a solid spherical particle submerged in a large body of a fluid are presented in Figure 53 by the Heisler Chart [Heisler, 1947 and Geankoplis, 2003]. Figure 53 was used to create temperature gradient profiles in the limestone particle in SAP at different T_1 temperatures. θ_o^* is a temperature-dependent unitless parameter. F_o represents a time-dependent unitless parameter. The calculations were made by assuming that complete propane combustion with 14 % excess of air and are presented in Figure 54.

According to Figure 54, it can be concluded that heat transfer from the SAP gas to the center of a 80 μm limestone particle is very rapid. In fact, the temperature at the center of limestone particle reaches the gas temperature after only 0.1 second at gas temperatures above 825 K. Therefore, it was concluded that heat transfer is not a rate limiting step during the thermal decomposition of limestone in a dilute-phase flash calcination reactor such as the SAP. Calcination kinetics, calcination residence time, and mass transfer limitations (internal and external diffusional resistances and internal pore plugging) have potentially more impacts on the

EC in flash calcination. In addition, a non-uniform CO_2 concentration in the calcination reactor also affects the calcination and recarbonation kinetics of limestone. Mass transfer limitations; however, were not considered in interpreting the calcination kinetic data reported in this work.

Figure 53. Heisler Chart for Determining the Center Temperature of a Sphere with Radius of r_o.

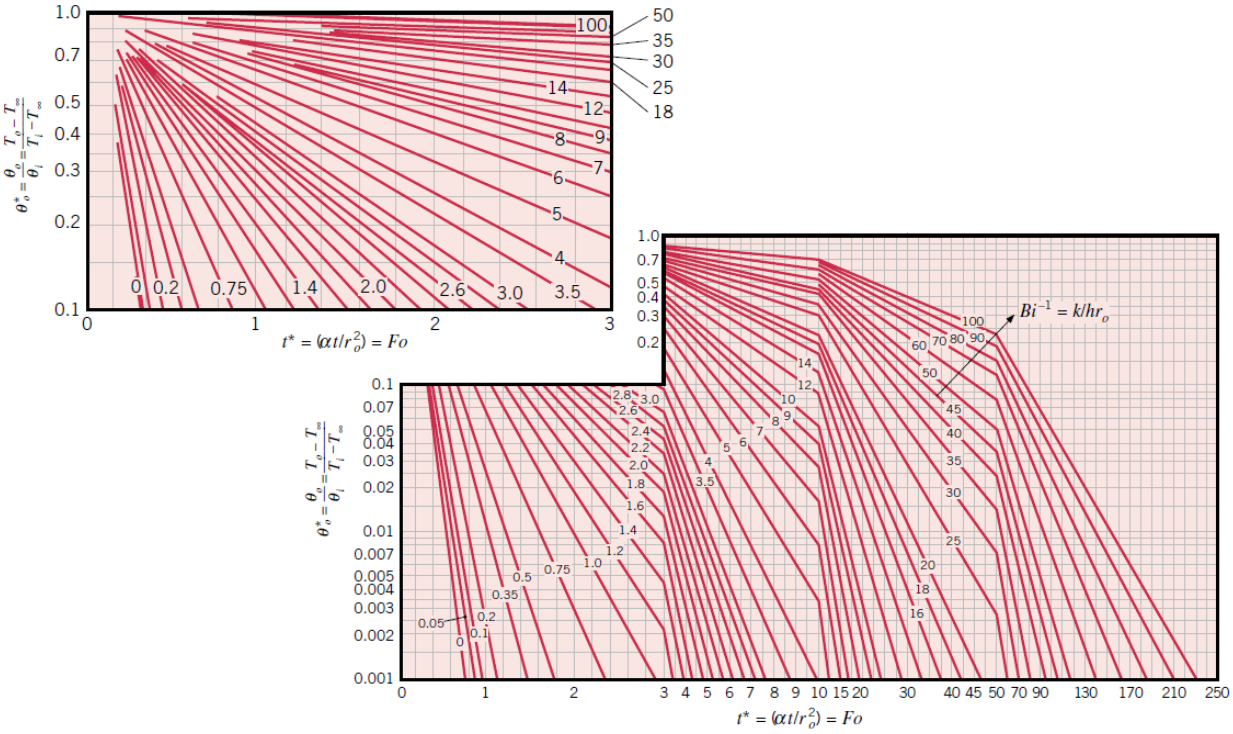

Figure 54. Heat up rate of a 80 µm Limestone Particle at Different Gas Temperatures in an Entrained-Flow Reactor.

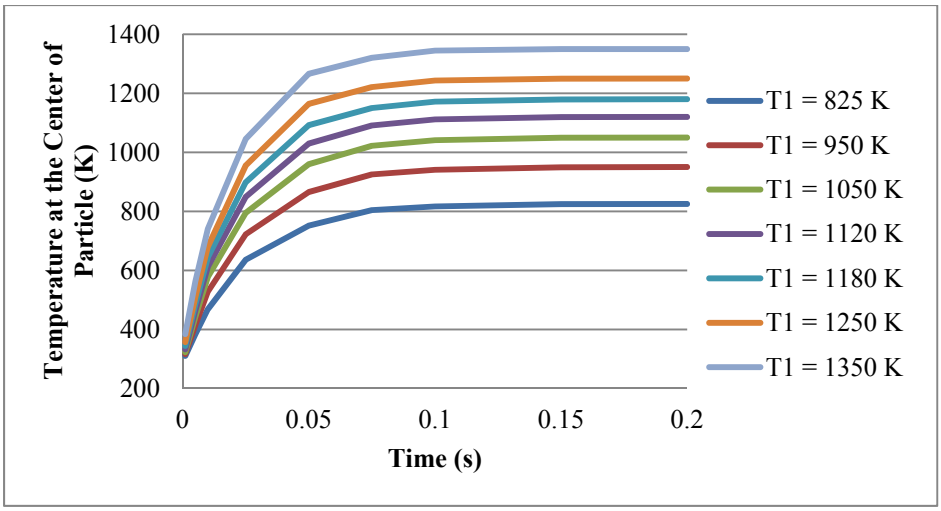

3.3.2 TGA Calcination in N_2

In TGA calcination experiments in N_2, recarbonation reaction of lime was assumed to be negligible because a small mass (< 25 mg) of limestone sample and a high flow of N_2 gas purge (100 mL/min) were used to sweep away the released CO_2 from the vicinity of the sample. For decomposition of 50 mg limestone in N_2 (100 ml/min) at a linear heating rate of 10 K/min, the amount and the rate of CO_2 released from the sample in a major decomposition region (between 950 and 1,050 K or 10 minutes reaction time) are 0.0005 moles and 0.00005 moles/min. Therefore, the average concentration of CO_2 in the vicinity of the sample pan during the thermal decomposition reaction of limestone is 1 mol %, or 0.01 atm, or 1 kPa. According to the chemical equilibrium, at P_{CO_2} of 1 kPa, limestone decomposes at 825 K (Figure 2). Therefore, TGA calcination data generated in N_2 describes only the thermal decomposition of $CaCO_3$ to CaO.

In TGA experiments, limestone samples MRC-LS and MSS-LS (< 25 mg) were heated in 100 mL/min N_2 at linear heating rates of 2, 5, and 10 K/min to 1,273 K (Figure 55 and Figure 56, respectively). The solid and dotted lines in Figure 55 and Figure 56 present the TG or weight change and DTG or rate of weigh change data for the limestone samples. Under these test conditions, the thermal decomposition reaction of limestone begins at 873 K and terminates at 1,073 K. The rate of weight loss, corresponding to the thermal decomposition of calcium carbonate to calcium oxide, increases as temperature increases and reaches a maximum at 973 K. At temperatures above the maximum rate, the rate of weight loss decreases as lesser amounts of calcium carbonate remain in the sample. Eventually the rate becomes zero as all of the calcium carbonate in the sample decomposes to calcium oxide. Theoretically, for a pure limestone (100 % calcium carbonate), a complete conversion of calcium carbonate to calcium oxide should yield 44 % weight loss. The weight changes profiles in Figure 55 and Figure 56 are less than 44 % due to the presences of impurities such as silicon oxide (Si_2O_3), aluminum oxide (Al_2O_3), and other minerals in the sample. Weight changes attributed to the decomposition of these impurities typically take place at temperatures higher than 1,273 K [Adolfsson, et al., 1999].

As shown in Figure 55 and Figure 56, TG and DTG curves of calcination shifted to lower temperatures at slower heating rates. One advantage of measuring the kinetics at a slower heating rate is to minimize the difference between the temperature of sample particles and the

temperature in the gas phase in the vicinity of the sample, where the TGA thermocouple is located. In addition, CO_2 is released at a slower rate during the thermal decomposition of $CaCO_3$ and rapidly is mixed with the purge gas, preventing local CO_2 accumulation around limestone particles. Therefore, a slow heating rate is more favorable to a fast heating rate from thermodynamics and mass and heat transfer considerations.

The shape of the TG and DTG profiles of sample MRC-LS at 2, 5 and 10 K/min were similar. At a heating rate of 2 K/min, sample MRC-LS began to decompose at 775 K, the rate of the decomposition reached a maximum at 975 K, and the reaction was completed at 1,000 K. However, the profiles shifted by 50 K at 5 K/min and 100 K at 10 K/min to higher decomposition temperatures. The TG and DTG profiles of sample MSS-LS were similar to those observed for sample MRC-LS at the tested heating rates; however, the onset, the maximum rate, and the termination temperatures were 50 K lower that those observed for sample MRC-LS at each heating rate. Hence, it can be conclude that sample MRC-LS is thermally less reactive than sample MSS-LS.

Figure 55. TG and DTG Data from Calcination of Sample MRC-LS in N_2.

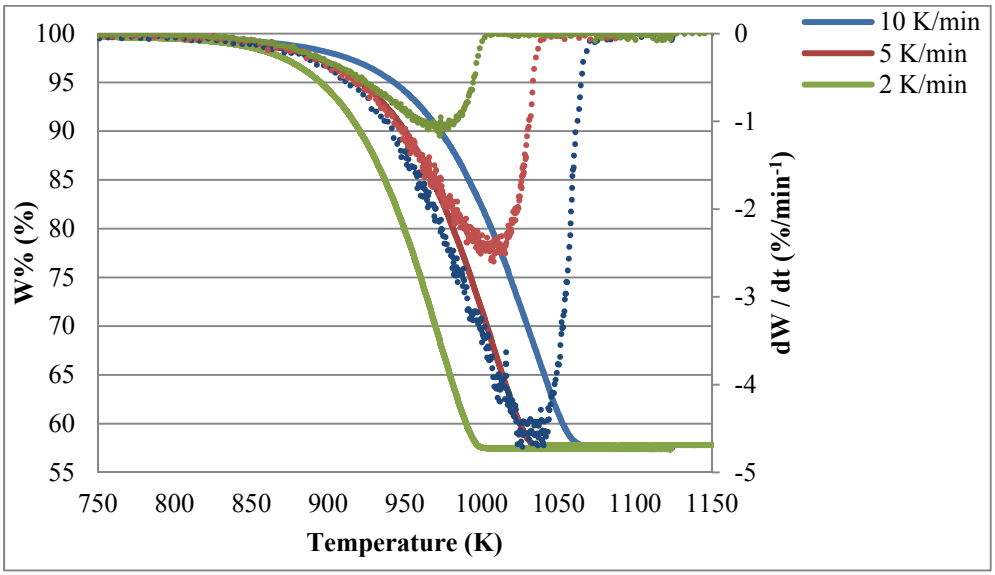

Figure 56. TG and DTG Data from Calcination of Sample MSS-LS in N_2.

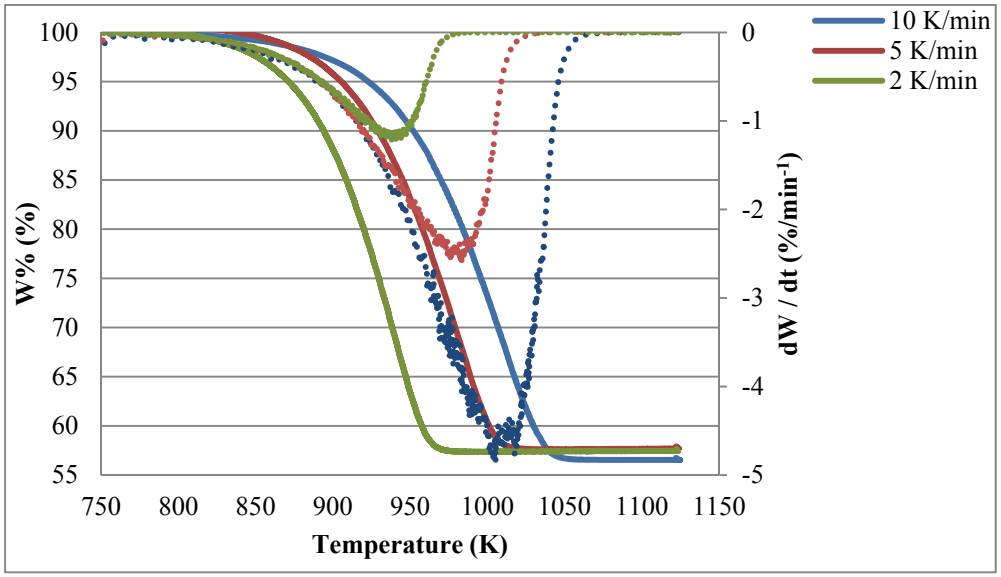

3.3.2.1 Kinetics Analysis of Calcination by DTG-Curve-Fitting Method

The calculated average values of kinetics parameters are listed in Table 6.The predicted kinetic parameters at 2, 5 K/min, and 10 K/min heating rates were comparable (< 5 % deviation). The values of Ea, n, and A are also comparable with those reported in the literature for several different limestone samples (Ar and Dogu, 2001).

Table 6. Average Kinetic Parameters for Samples MRC-LS and MSS-LS Obtained by DTG-SIM Method.

Description	Ea (kJ/mol)	A (min^{-1})	n
MRC-LS	196.5	1.9E+9	0.55
MSS-LS	176	2.64E+8	0.6

The calculated kinetic parameters were included in Equation 26 and Equation 27 to generate predicted conversion (α) and the rate of conversion (dα/dT) data. A comparison between the predicted and experimental data for sample MRC-LS (Figure 57 to Figure 59) and for sample MSS-LS (Figure 60 to Figure 62) show good agreements between the experimental and predicted α and dα/dT at each heating rate and conversion levels between 15 and 75 %. This

conversion range presents the range of the EC obtained in the SAP. The deviations between the experimental and predicted α and dα/dT data were quantified using Equation 39 and are summarized in Table 7. They are less than 10 % in the temperature and the conversion ranges selected. It should be noted that this kinetic model describes the calcination reaction of the limestone in an inert atmosphere and does not include the contribution of the recarbonation reaction of lime. The kinetic model should be used with some caution to predict calcination data outside the range of the experimental data employed in the kinetic analysis.

Figure 57. Comparison of Predicted (DTG-SIM) and Experimental α and dα/dT of Sample MRC-LS at 10 K/min in N_2.

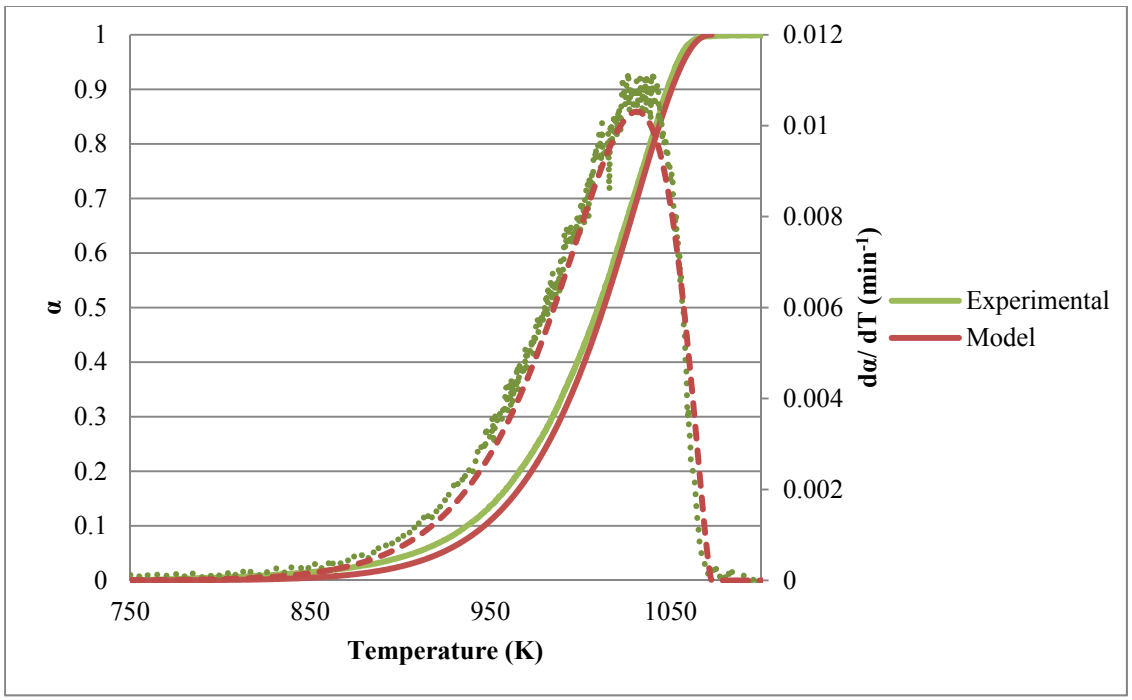

Figure 58. Comparison of Predicted (DTG-SIM) and Experimental α and dα/dT of Sample MRC-LS at 5 K/min in N_2.

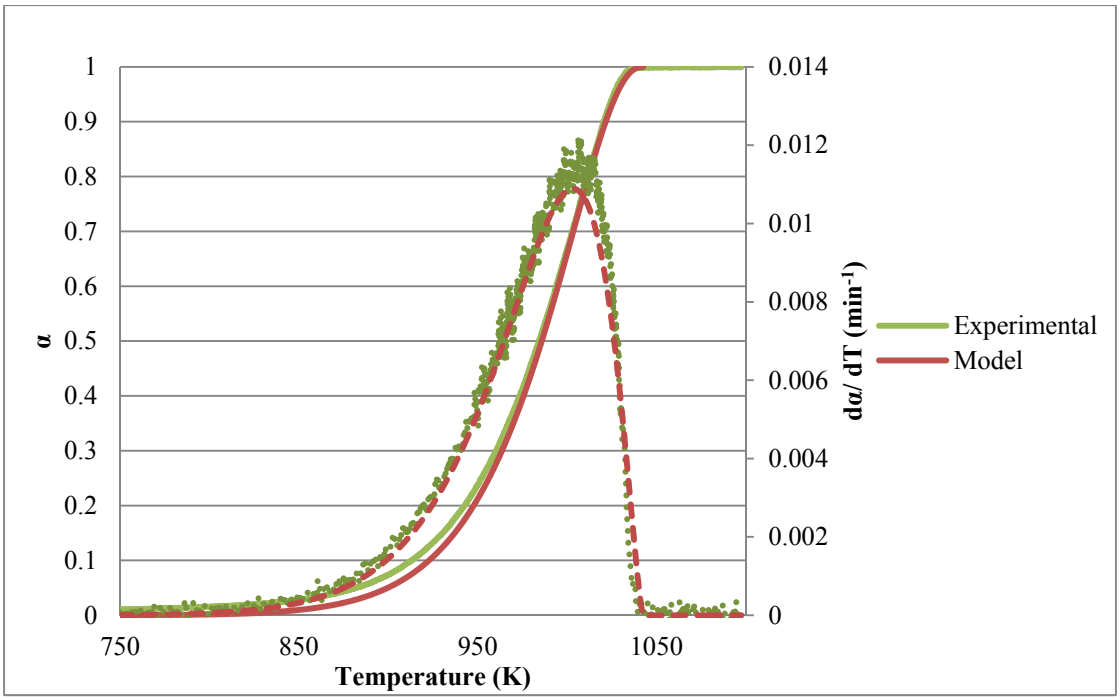

Figure 59. Comparison of Predicted (DTG-SIM) and Experimental α and dα/dT of Sample MRC-LS at 2 K/min in N_2.

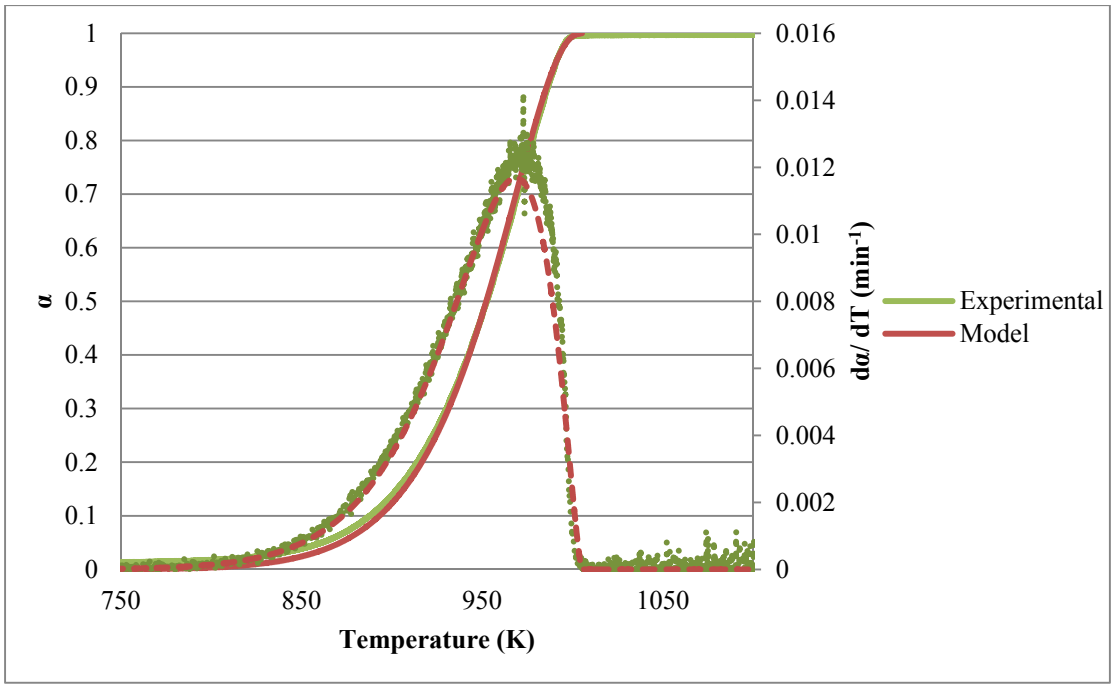

Figure 60. Comparison of Predicted (DTG-SIM) and Experimental α and dα/dT of Sample MSS-LS at 10 K/min in N_2.

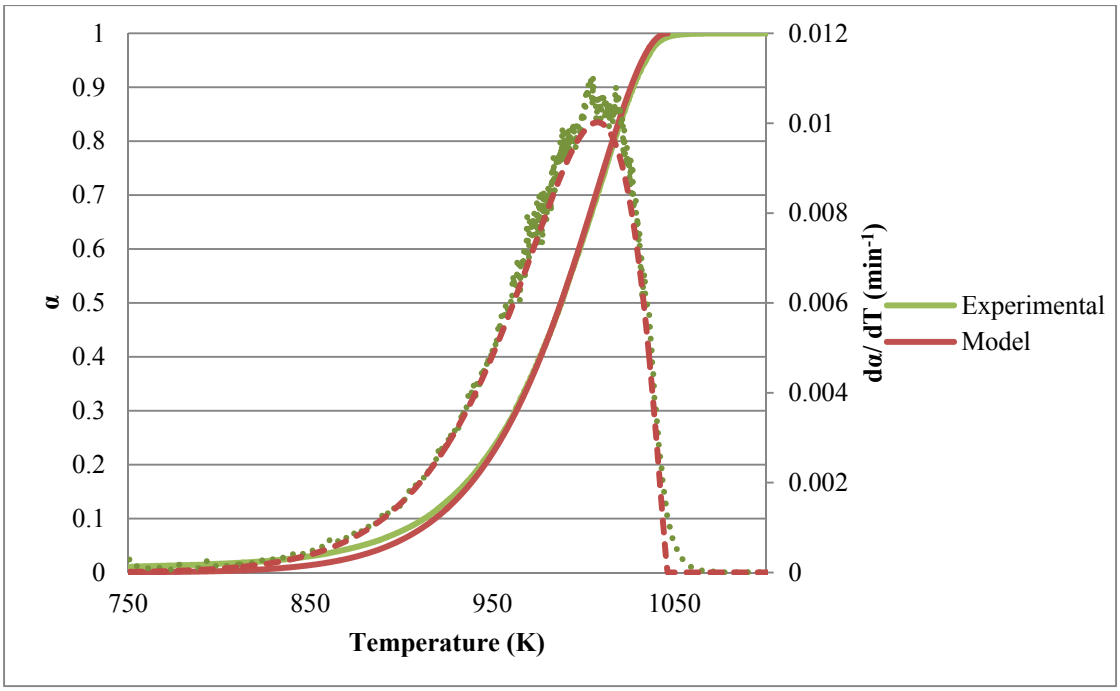

Figure 61. Comparison of Predicted (DTG-SIM) and Experimental α and dα/dT of Sample MSS-LS at 5 K/min in N_2.

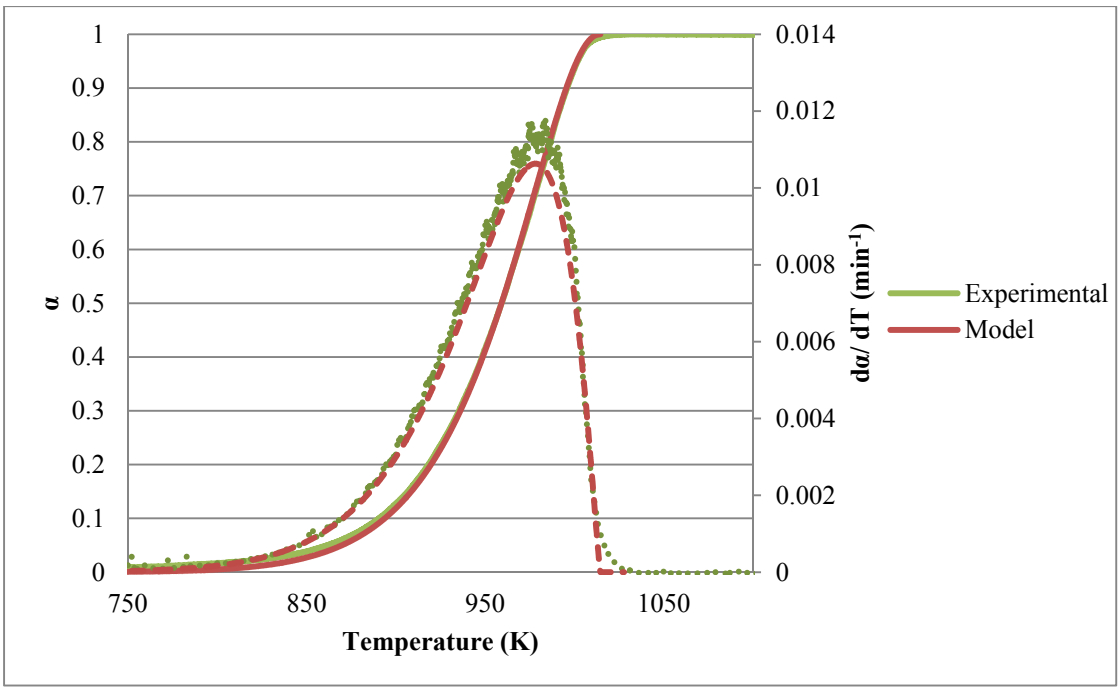

Figure 62. Comparison of Predicted (DTG-SIM) and Experimental α and dα/dT of Sample MSS-LS at 2 K/min in N_2.

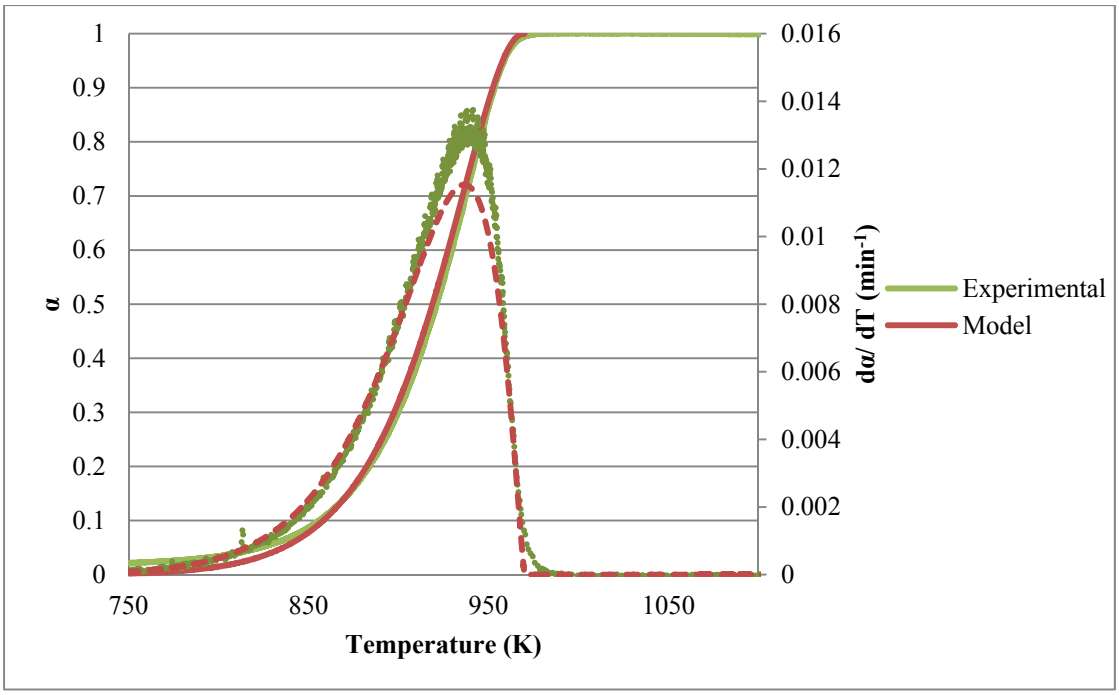

Table 7. Deviations between Predicted (DTG-SIM Model) and Experimental Data in N_2.

Heating Rate (K/min)	MRC-LS		MSS-LS	
	Deviation of α (%)	Deviation of dα/dT (%)	Deviation of α (%)	Deviation of dα/dT (%)
10	9.63	6.91	2.34	4.30
5	6.94	4.62	1.81	5.78
2	3.38	3.71	4.55	5.62

3.3.2.2 Coats-Redfern-Linearization-Based Method

Experimental TGA calcination data in Figure 55 for sample MRC-LS and in Figure 56 for sample MSS-LS were plotted according to the dictate of Equation 31 for $n \neq 1$ and Equation 32 for $n = 1$. When $n = 1$, the R^2 obtained when data were plotted according to Equation 32 was < 0.1. Thus, calcination of limestone in N_2 atmosphere could not be described by a 1st order

reaction. The value of n in Equation 31 was varied to obtain the highest R^2 based on assumed n values. The highest R^2 values were obtained using CR-Linearized method when n = 0.6 as shown in Figure 63 and Figure 64. Activation energy and frequency factor were calculated using Equation 35 and Equation 36 from the slopes and intercepts of these plots and are summarized in Table 8. The deviations between the kinetic parameters obtained using CR-Linearization technique at each heating rate were higher than those obtained using the DTG-SIM method. Hence, the predicted α and dα/dT values based on the average kinetic parameters did not fit the experimental data well based on the author's visual inspection and personal interpretation.

Figure 63. CR-Linearized Plot (Equation 31) for MRC-LS Calcination at 2, 5, and 10 K/min in N_2.

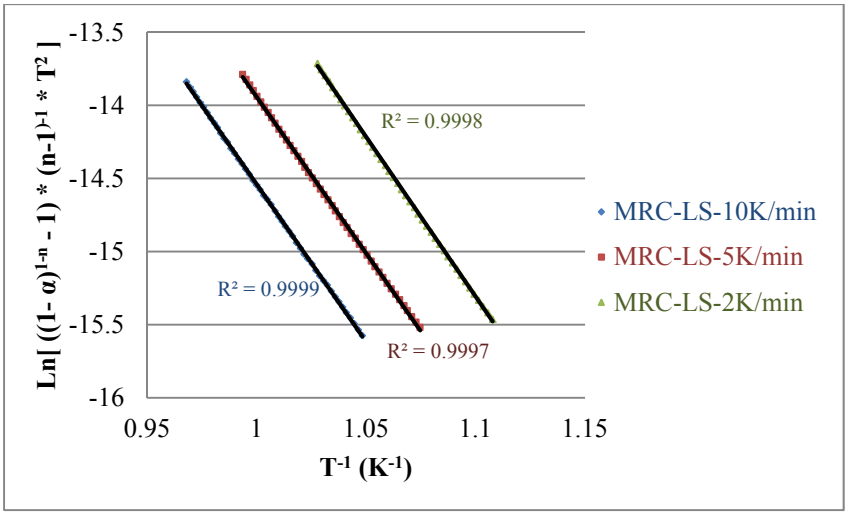

Figure 64. CR-Linearized Plot (Equation 31) for MSS-LS Calcination at 2, 5, and 10 K/min in N_2.

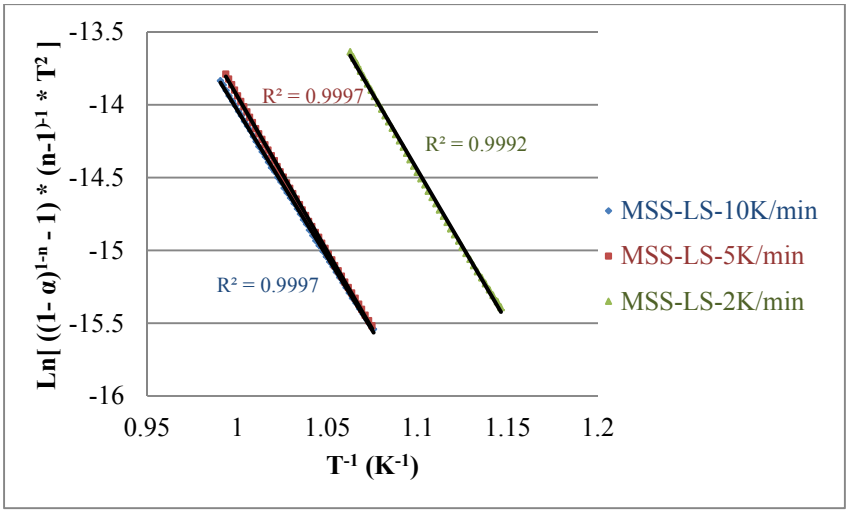

Table 8. Ea and A Obtained by CR-Linearization Method

Heating Rate (K/min)	MRC-LS			MSS-LS		
	Ea	A	n	Ea	A	n
	kJ/mol	min^{-1}		kJ/mol	min^{-1}	
10	179	2.52 E+08	0.6	169	1.14E+08	0.6
5	178	1.94 E+08	0.6	171	1.59E+08	0.6
2	182	2.82 E+08	0.6	191	2.78E+08	0.6

Conversion and rate of conversion data predicted by Equation 26 and Equation 27 based on the parameters listed in Table 8 were compared to the experimental data of sample MRC-LS (Figure 65 to Figure 67) and sample MSS-LS (Figure 68 to Figure 70). The deviations between the predicted and the experimental data, calculated using Equation 39 and summarized in Table 9, were less than 7 % in the range of interest (conversions between 10 and 75 %). However, the model could not accurately predict the maximum rate of conversion (10 % deviation) of the limestone samples.

Figure 65. Comparison of Predicted (CR-Based) and Experimental α and dα/dT of Sample MRC-LS at 10 K/min in N_2.

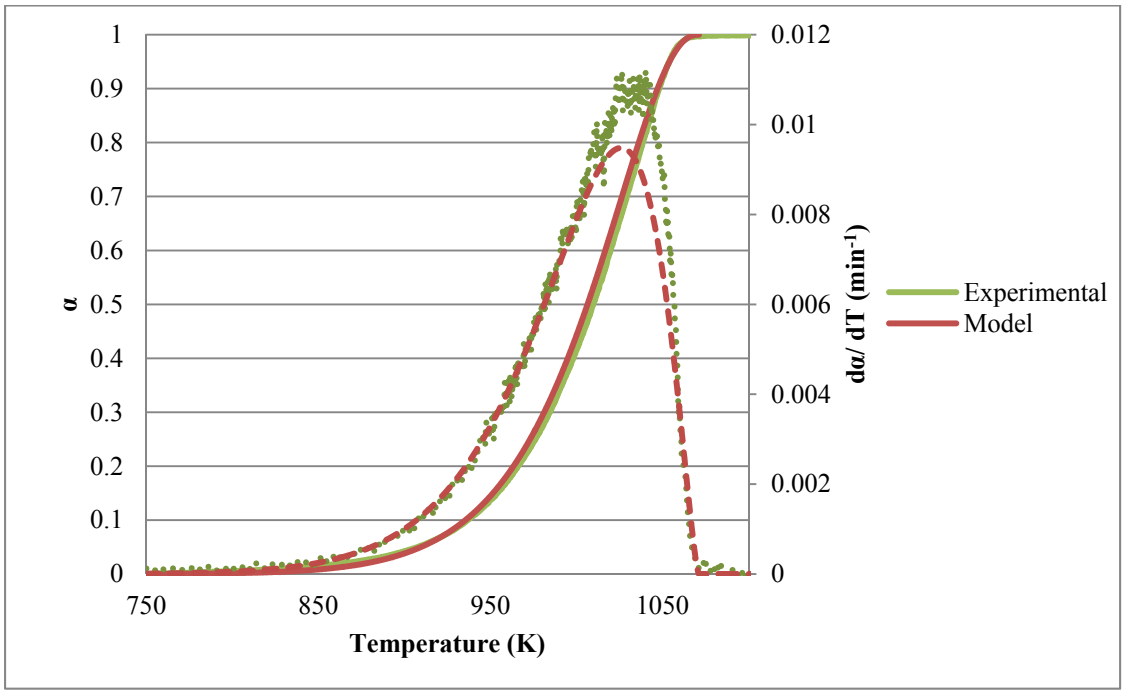

Figure 66. Comparison of Predicted (CR-Based) and Experimental α and dα/dT of Sample MRC-LS at 5 K/min in N_2.

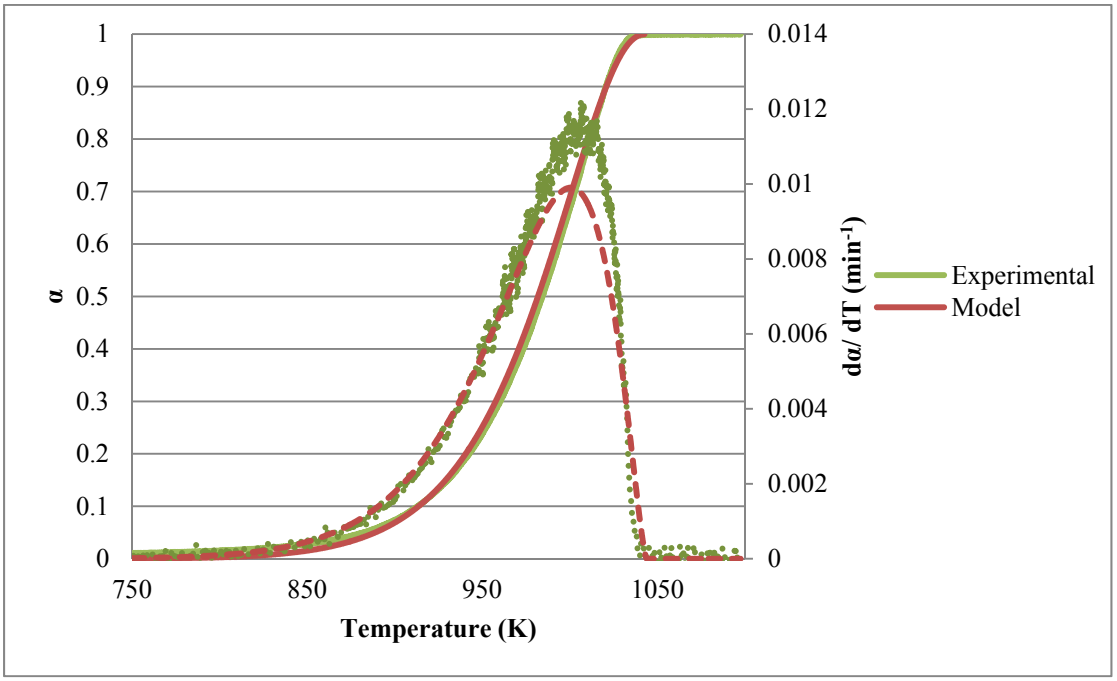

Figure 67. Comparison of Predicted (CR-Based) and Experimental α and dα/dT of Sample MRC-LS at 2 K/min in N_2.

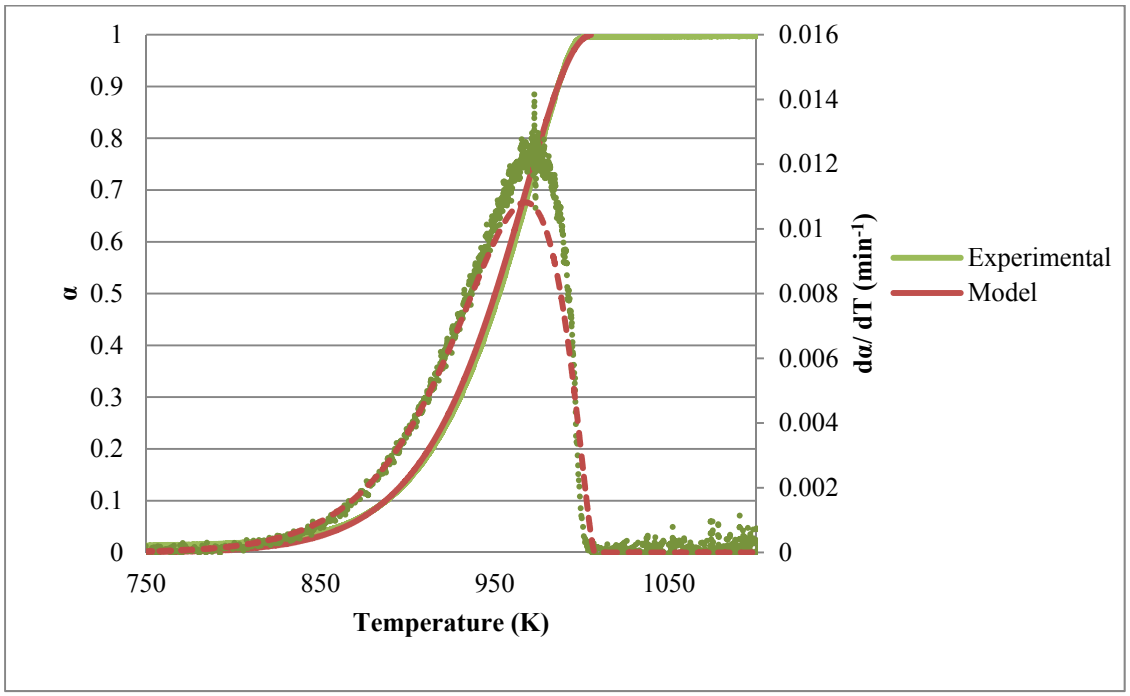

Figure 68. Comparison of Predicted (CR-Based) and Experimental α and dα/dT of Sample MSS-LS at 10 K/min in N_2.

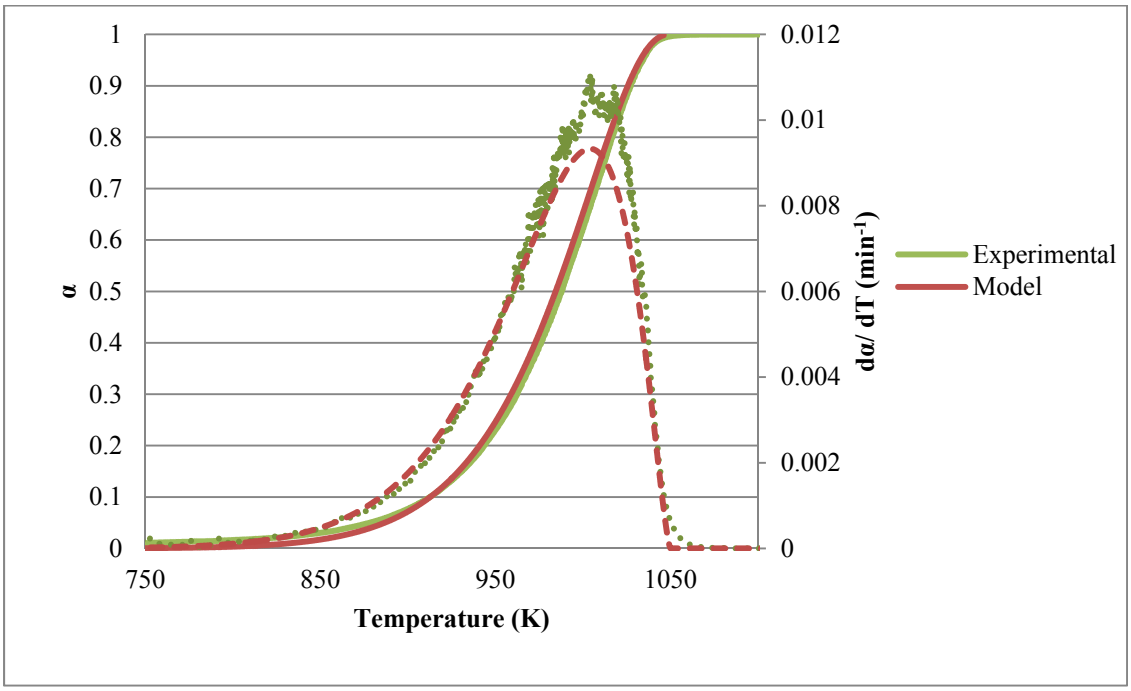

Figure 69. Comparison of Predicted (CR-Based) and Experimental α and dα/dT of Sample MSS-LS at 5 K/min in N_2.

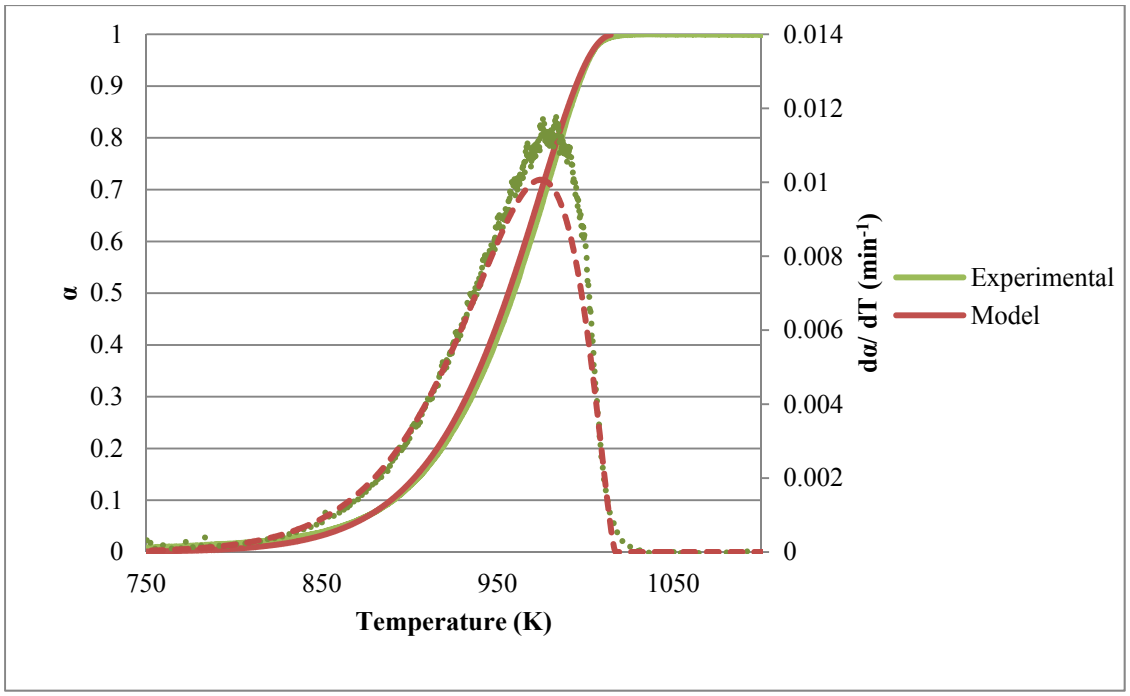

Figure 70. Comparison of Predicted (CR-Based) and Experimental α and dα/dT of Sample MSS-LS at 2 K/min in N_2.

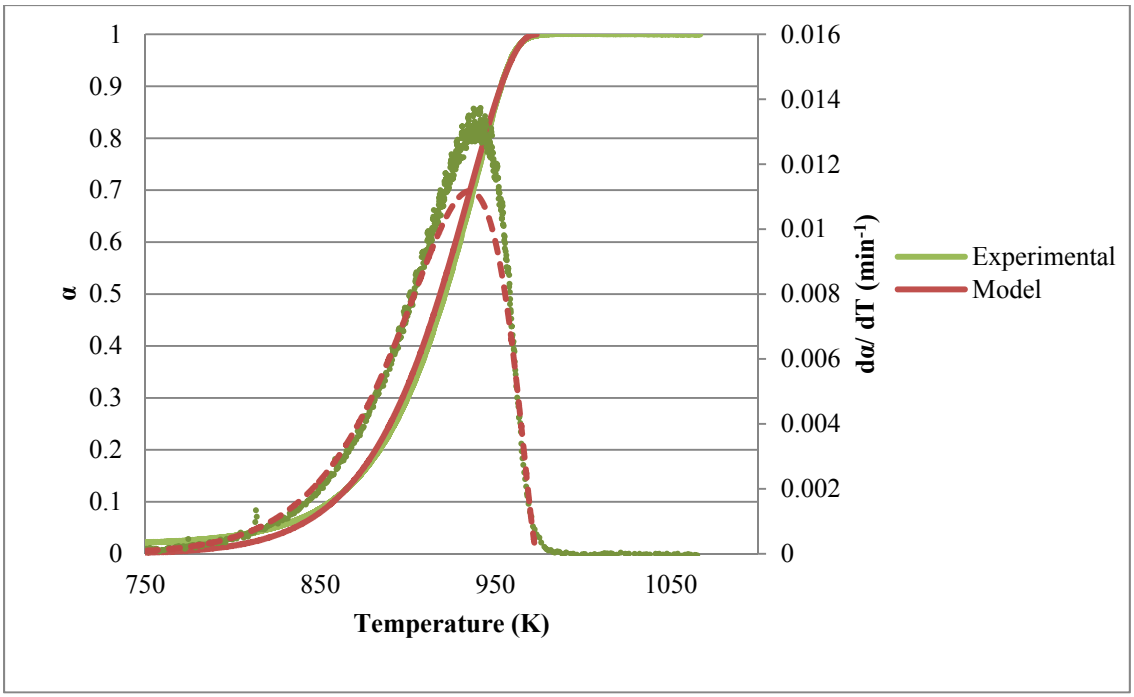

Table 9. Deviations between Predicted (Criado-Redfern) and Experimental Data in N_2.

Heating Rate (K/min)	MRC-LS		MSS-LS	
	Deviation of α (%)	Deviation of dα/dT (%)	Deviation of α (%)	Deviation of dα/dT (%)
10	6.20	4.82	6.25	5.64
5	5.00	5.88	6.03	4.67
2	4.48	5.63	5.80	6.74

3.3.2.3 Criado-Linearization Method

Figure 71 and Figure 72 represent the dictate of Equation 37 on the experimental TGA data of sample MRC-LS (Figure 55) and sample MSS-LS (Figure 56). The value of n in Equation 37 was varied to obtain the highest R^2 for each linearized plot. The highest R^2 was obtained for each plot when n = 0.6. Activation energy and frequency factor were calculated using Equation 35 and Equation 36 and they are summarized in Table 10.

Figure 71. Criado-Linearized Plot (Equation 37) for Sample MRC-LS Calcined at 2, 5, and 10 K/min in N_2.

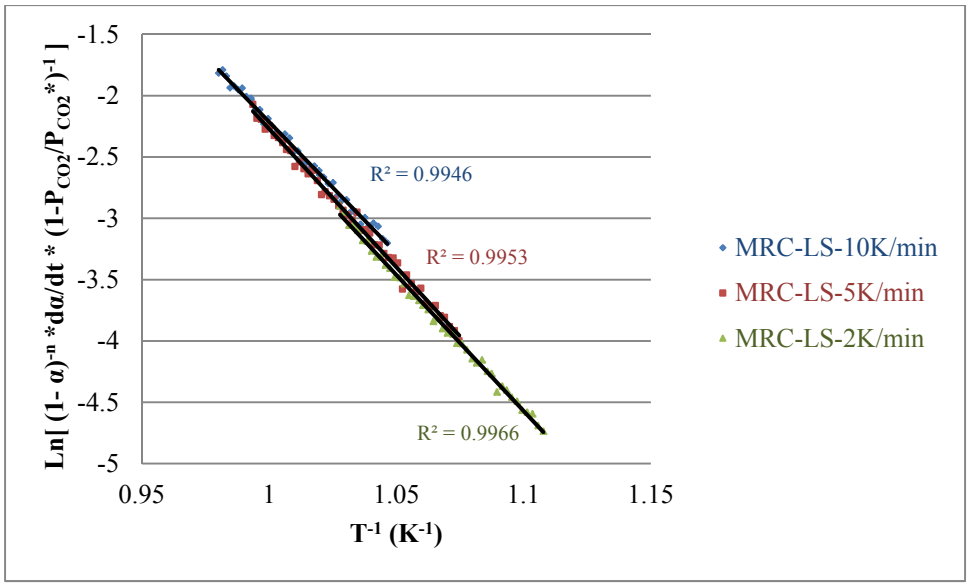

Figure 72. Criado-Linearized Plot (Equation 37) for Sample MSS-LS Calcined at 2, 5, and 10 K/min in N_2.

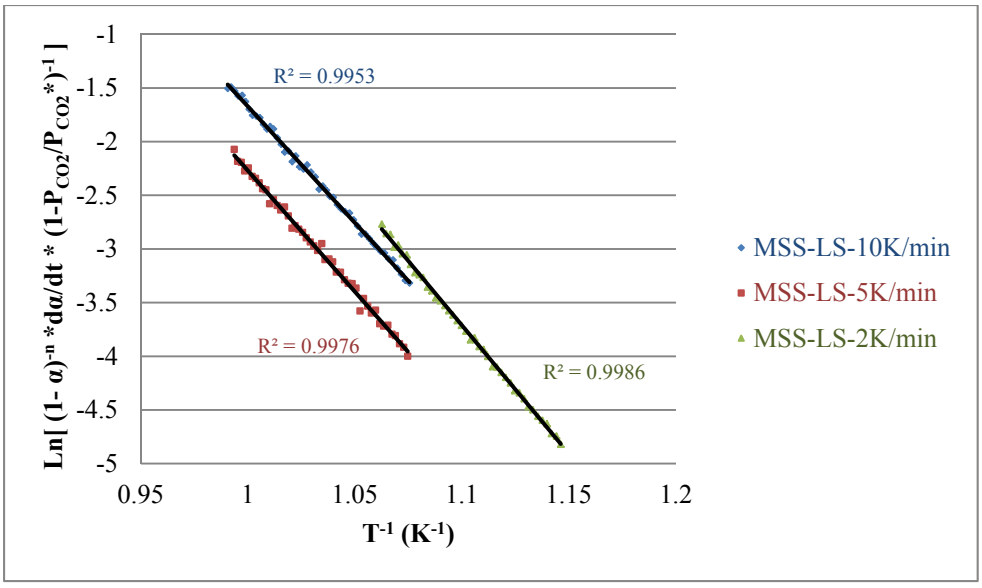

Table 10. The Values of Ea and A Obtained Using Criado-Linearization Technique.

Heating Rate (K/min)	MRC-LS			MSS-LS		
	Ea	A	n	Ea	A	n
	kJ/mol	min^{-1}		kJ/mol	min^{-1}	
10	181	3.12 E+08	0.6	181	5.12 E+08	0.6
5	186	5.12 E+08	0.6	192	1.15 E+08	0.6
2	186	4.77 E+08	0.6	196	4.72 E+08	0.6

Conversion (Equation 26) and rate of conversion (Equation 27) data were generated using parameters listed in Table 10 and compared to the experimental data for sample MRC-LS (Figure 73 to Figure 75) and sample MSS-LS (Figure 76 to Figure 78). The deviations between the predicted and the experimental data, calculated using Equation 39, were < 5 % (Table 11). The predicted TG and DTG data are in good agreements with the experimental data.

Figure 73. Comparison of Predicted (Criado) and Experimental α and dα/dT of Sample MRC-LS Calcined at 10 K/min in N_2.

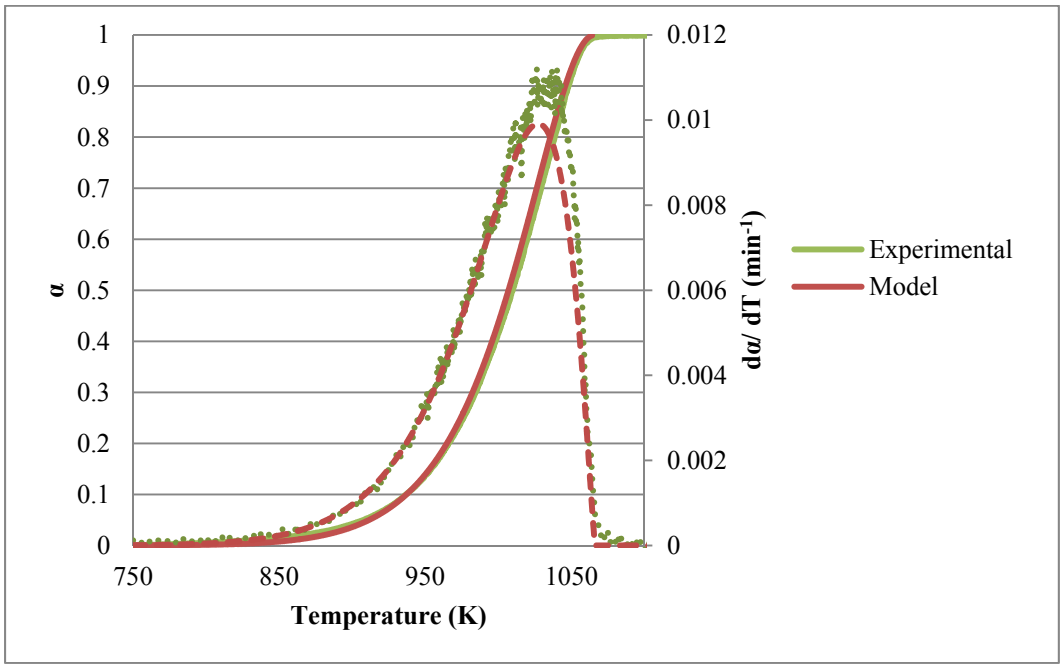

Figure 74. Comparison of Predicted (Criado) and Experimental α and dα/dT of Sample MRC-LS Calcined at 5 K/min in N_2.

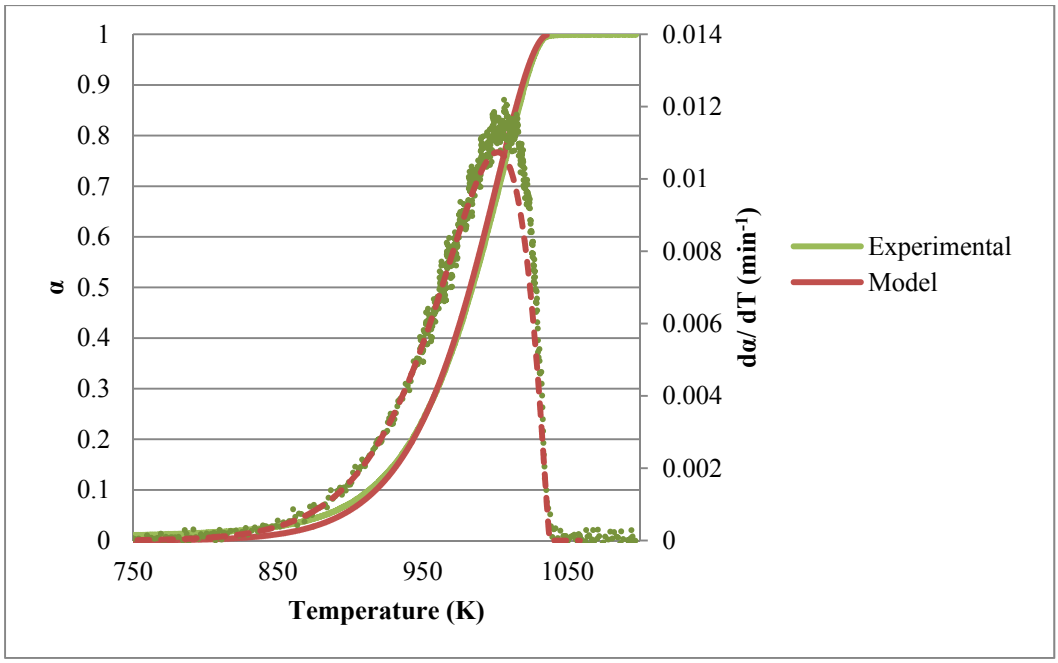

Figure 75. Comparison of Predicted (Criado) and Experimental α and dα/dT of Sample MRC-LS Calcined at 2 K/min in N_2.

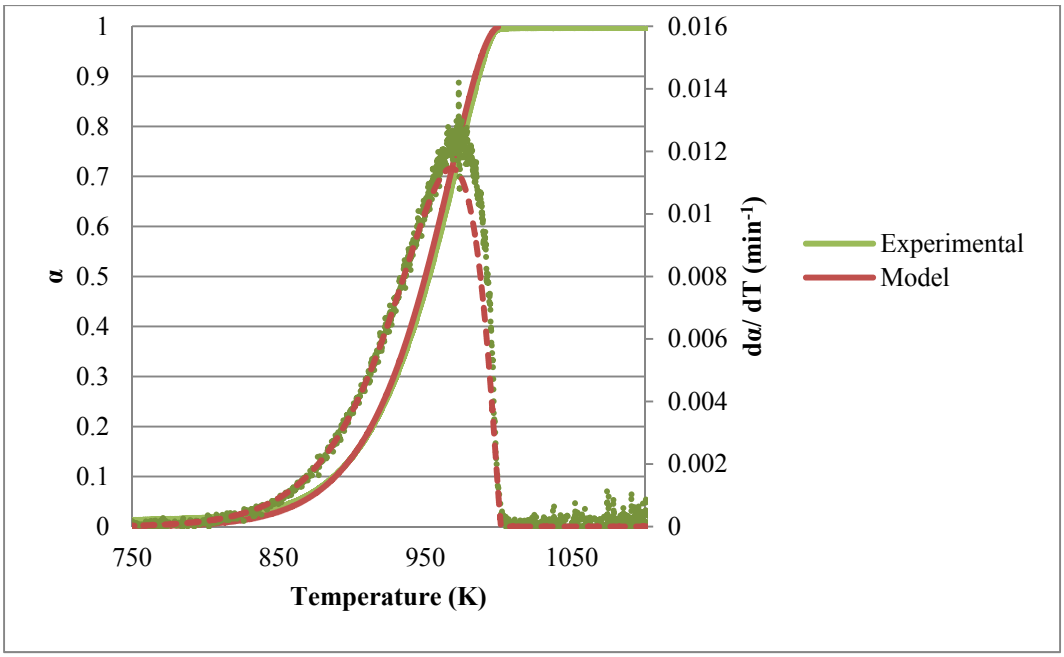

Figure 76. Comparison of Predicted (Criado) and Experimental α and dα/dT of Sample MSS-LS Calcined at 10 K/min in N_2.

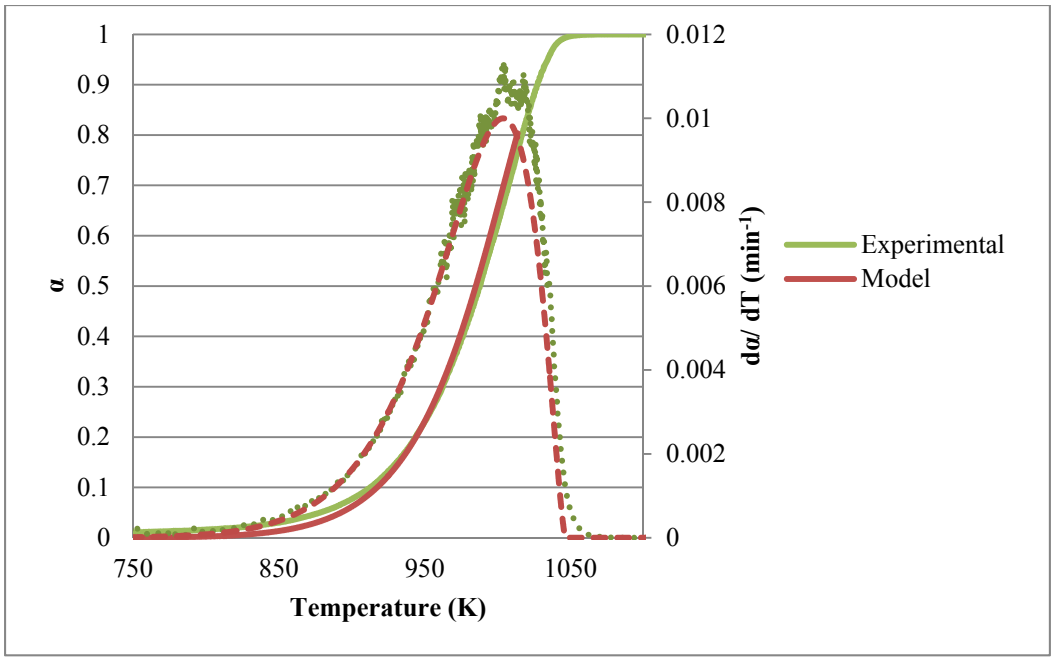

Figure 77. Comparison of Predicted (Criado) and Experimental α and dα/dT of Sample MSS-LS Calcined at 5 K/min in N_2.

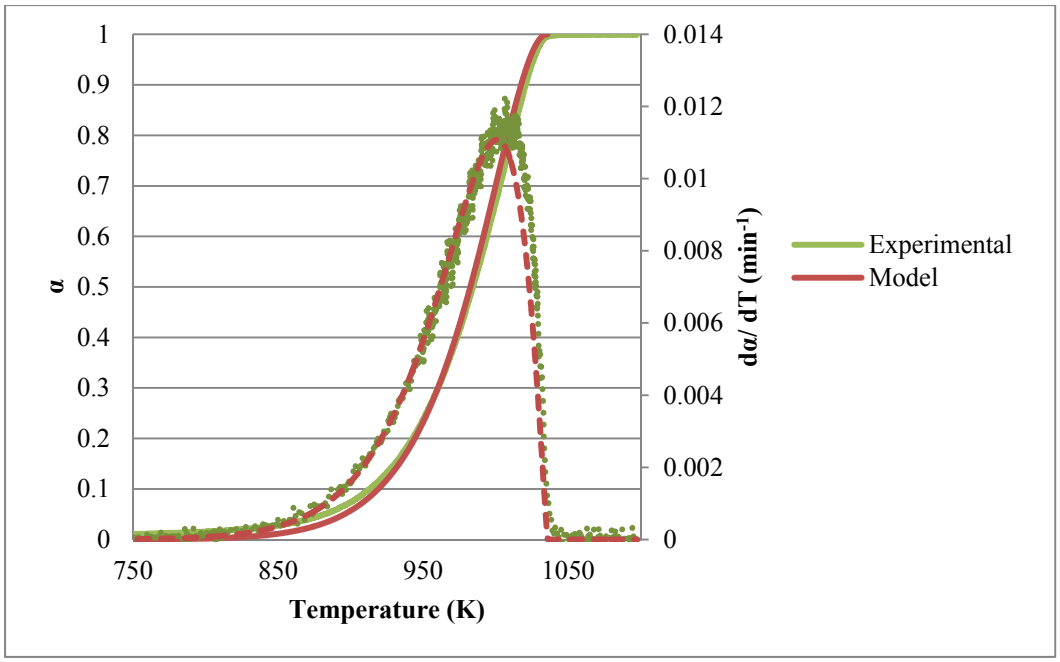

Figure 78. Comparison of Predicted (Criado) and Experimental α and dα/dT of Sample MSS-LS Calcined at 2 K/min in N_2.

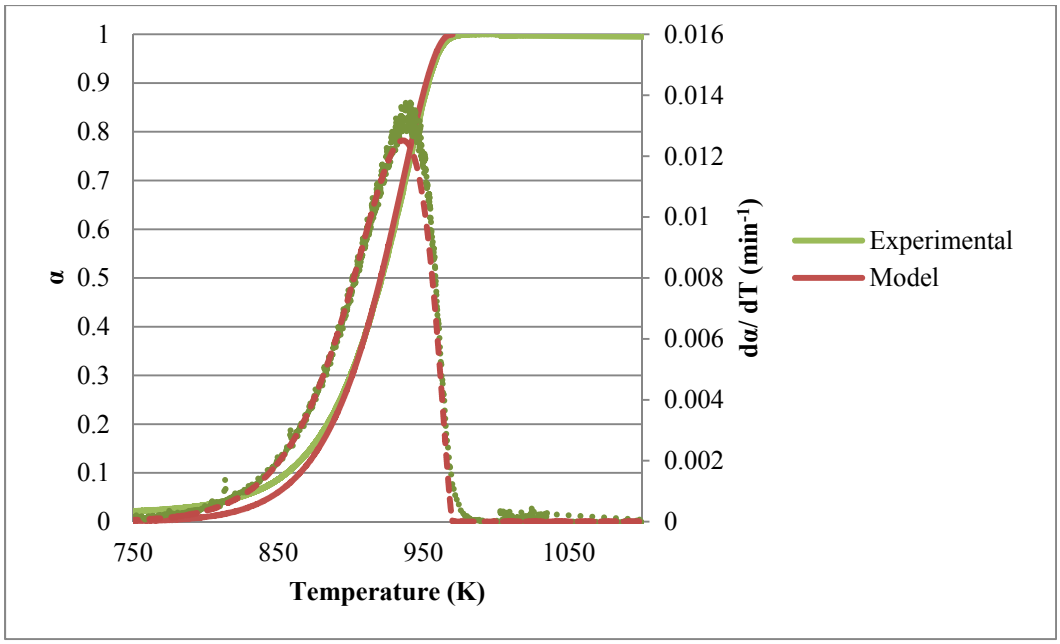

Table 11. Deviations between Predicted (Criado) and Experimental Calcination Data in N_2.

Heating Rate (K/min)	MRC-LS		MSS-LS	
	Deviation of α (%)	Deviation of dα/dT (%)	Deviation of α (%)	Deviation of dα/dT (%)
10	4.53	3.59	3.65	3.53
5	3.59	3.39	3.59	3.39
2	4.31	3.20	4.53	2.43

Results from the above discussion, regarding the three non-isothermal kinetic analysis methods, indicate that these data analysis approaches were adequate to predict thermal decomposition of the two limestone samples in N_2 at the selected heating rates. CR and Criado-Linearization methods resulted in different sets of kinetic parameters at different heating rates. The difference between each set of the kinetic parameters were; however, relatively small. Data

predicted by the CR-based method had smaller deviations (< 7 %) to the experimental data than the DTG-SIM-based method in the range of calcium carbonate mass conversions between 15 and 75 %. Differences between each set of kinetic parameters by the Criado Linearization method were rather significant; however, the predicted calcination data by this method had the smallest deviations (< 5%) amongst the three data analysis methods examined. The maximum deviation in the predicted α and dα/dT using the kinetics parameters obtained by the three methods for calcination in N_2 are summarized in Table 12.

Table 12. Summary of Calculated Kinetics Parameters and Maximum Deviations of Predicted α and dα/dT for Sample MRC-LS and MSS-LS in N_2 at Various Heating Rates.

Technique	Sample	Heating Rate (K/min)	Ea (kJ/mol)	A (min^{-1})	n	Max Deviation (%)
DTG SIM	MRC-LS	10, 5, 2	196	1.9E+9	0.55	10
DTG SIM	MSS-LS	10, 5, 2	176	2.64E+8	0.6	6
CR	MRC-LS	10	179	2.52 E+08	0.6	6
CR	MRC-LS	5	178	1.94 E+08	0.6	6
CR	MRC-LS	2	182	2.82 E+08	0.6	6
CR	MSS-LS	10	169	1.14E+08	0.6	6
CR	MSS-LS	5	171	1.59E+08	0.6	6
CR	MSS-LS	2	175	2.78E+08	0.6	7
Criado	MRC-LS	10	181	3.12 E+08	0.6	5
Criado	MRC-LS	5	186	5.12 E+08	0.6	4
Criado	MRC-LS	2	186	4.77 E+08	0.6	4
Criado	MSS-LS	10	181	5.12 E+08	0.6	4

Criado	MSS-LS	5	192	1.15 E+09	0.6	4
Criado	MSS-LS	2	196	4.72 E+09	0.6	5

3.3.3 TGA Calcination in CO_2

3.3.3.1 DTG-Curve-Fitting Method

The kinetic model in the DTG-SIM software does not consider the effect of partial pressure of CO_2 and thus the recarbonation reaction of lime; therefore, this method could not determine the intrinsic kinetic parameters of this type of calcination. Rather, the apparent kinetics parameters obtained by this method only are valid to describe the net thermal decomposition reaction of limestone in the temperature region where the data were analyzed. Therefore, prediction of rates outside the limits of the experimental data used to obtain the kinetic expressions will not be accurate. Kinetic parameters determined with the DTG-SIM method are summarized in Table 13. The predicted conversion and the rate of conversion data for sample MRC-LS (Figure 79 to Figure 81) and sample MSS-LS (Figure 82 to Figure 84) using Equation 26 and Equation 27 exhibited poor fits to the experimental data.

Table 13. The Values of Ea and A Obtained Using DTG-Curve-Fitting Technique in DTG-SIM.

P_{CO_2} (kPa)	MRC-LS			MSS-LS		
	Ea	A	n	Ea	A	n
	kJ/mol	min^{-1}		kJ/mol	min^{-1}	
11	358	9.56 E+15	0.55	181	1.88 E+16	0.48
25	358	5.24 E+15	0.55	192	6.25 E+15	0.51
50	358	1.77 E+15	0.55	196	1.77 E+15	0.51

Figure 79. Comparison of Predicted (DTG-SIM) and Experimental α and dα/dT of Sample MRC-LS at 5 K/min in 10 kPa P_{CO_2}.

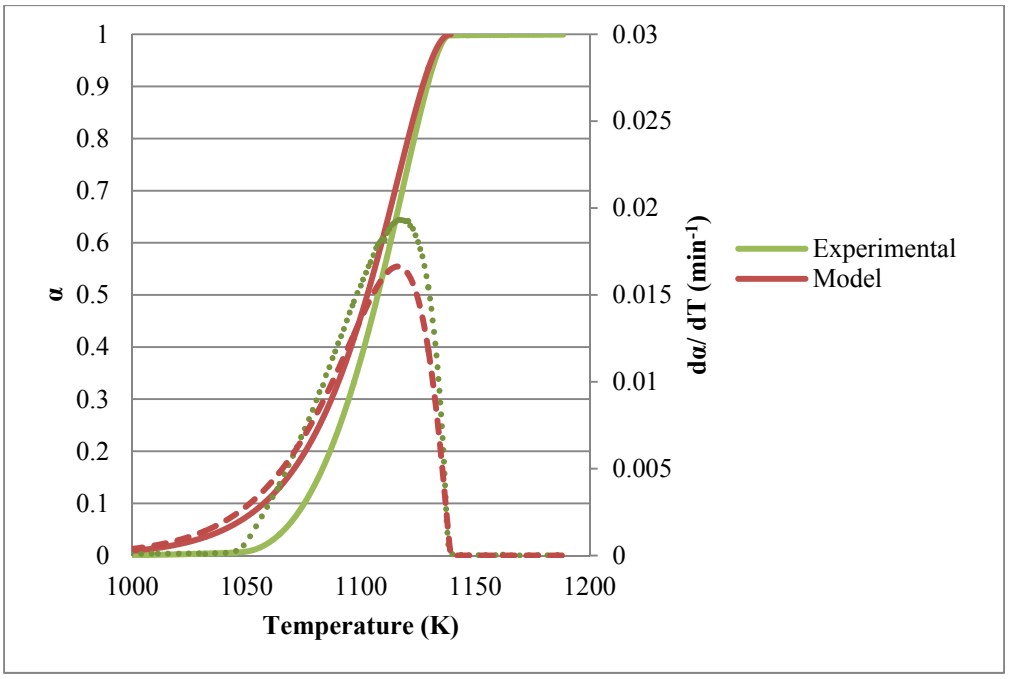

Figure 80. Comparison of Predicted (DTG-SIM) and Experimental α and dα/dT of Sample MRC-LS at 5 K/min in 25 kPa P_{CO_2}.

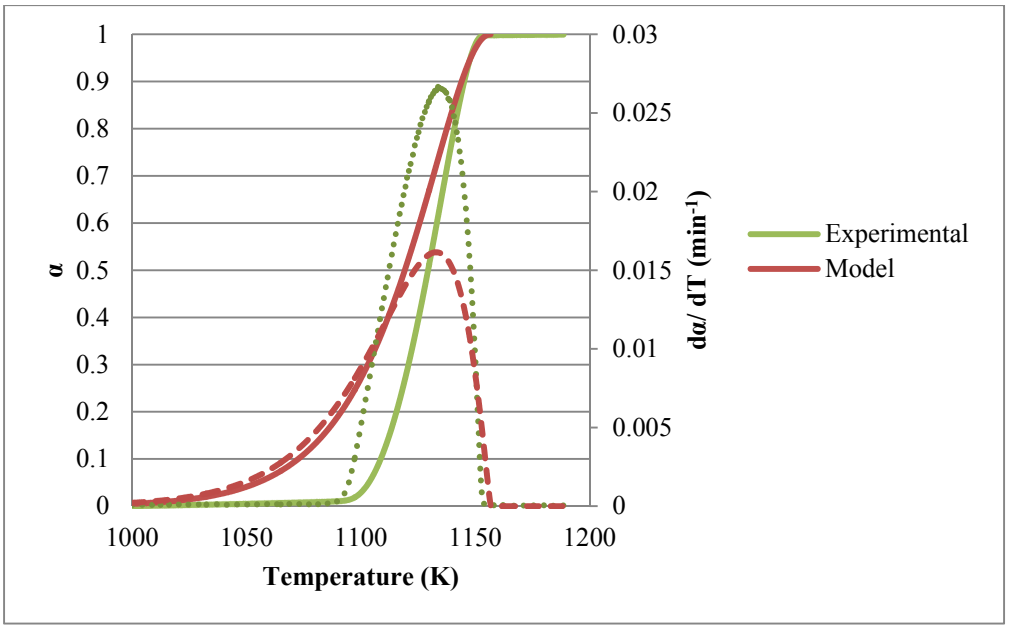

Figure 81. Comparison of Predicted (DTG-SIM) and Experimental α and dα/dT of Sample MRC-LS at 5 K/min in 50 kPa P_{CO_2}.

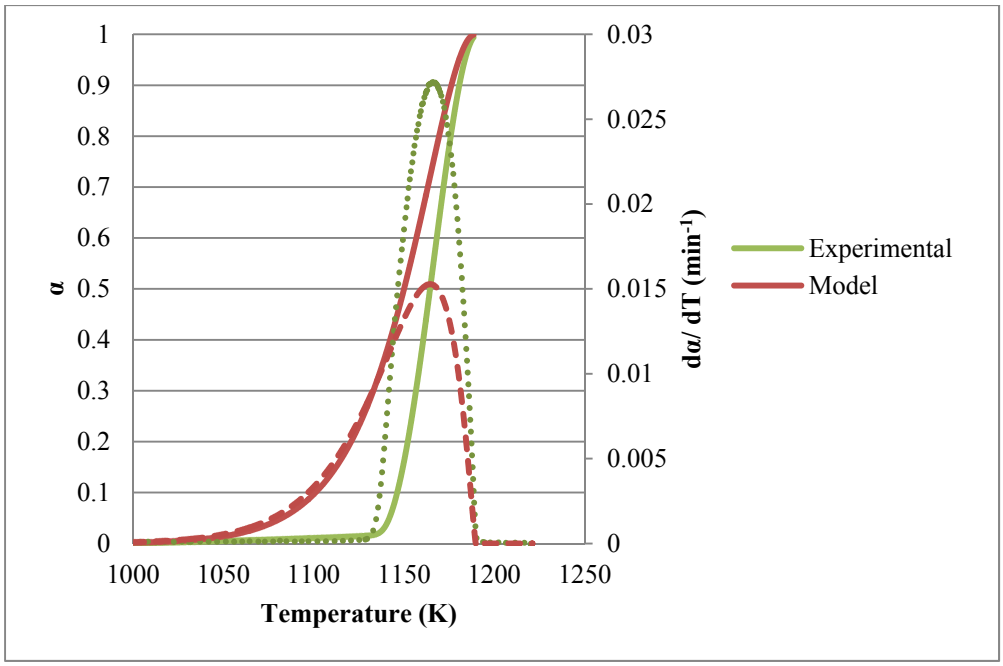

Figure 82. Comparison of Predicted (DTG-SIM) and Experimental α and dα/dT of Sample MSS-LS at 5 K/min in 10 kPa P_{CO_2}.

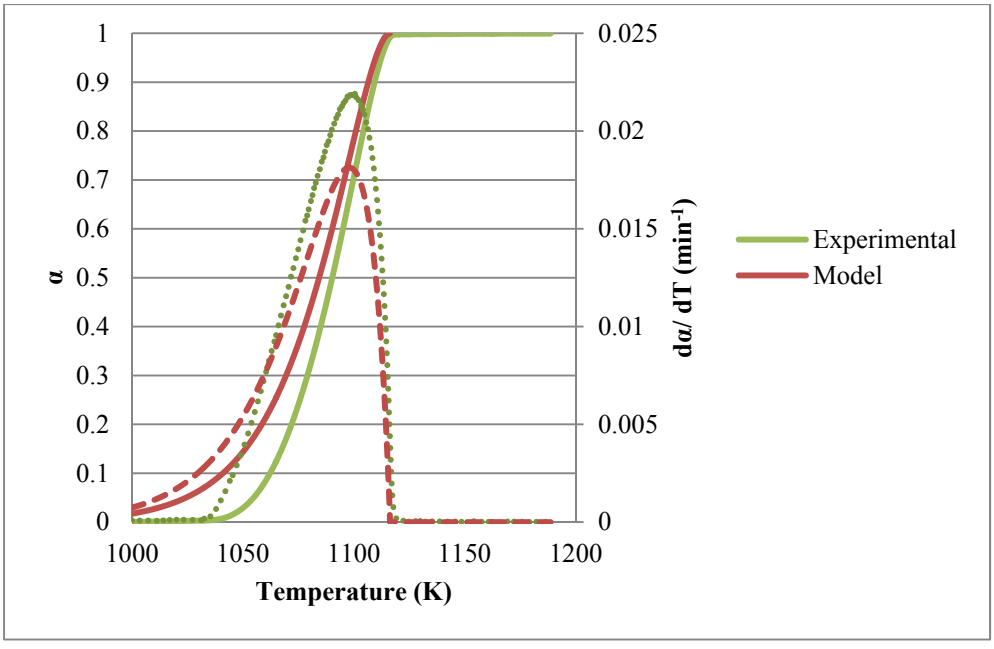

Figure 83. Comparison of Predicted (DTG-SIM) and Experimental α and dα/dT of Sample MSS-LS at 5 K/min in 25 kPa P_{CO_2}.

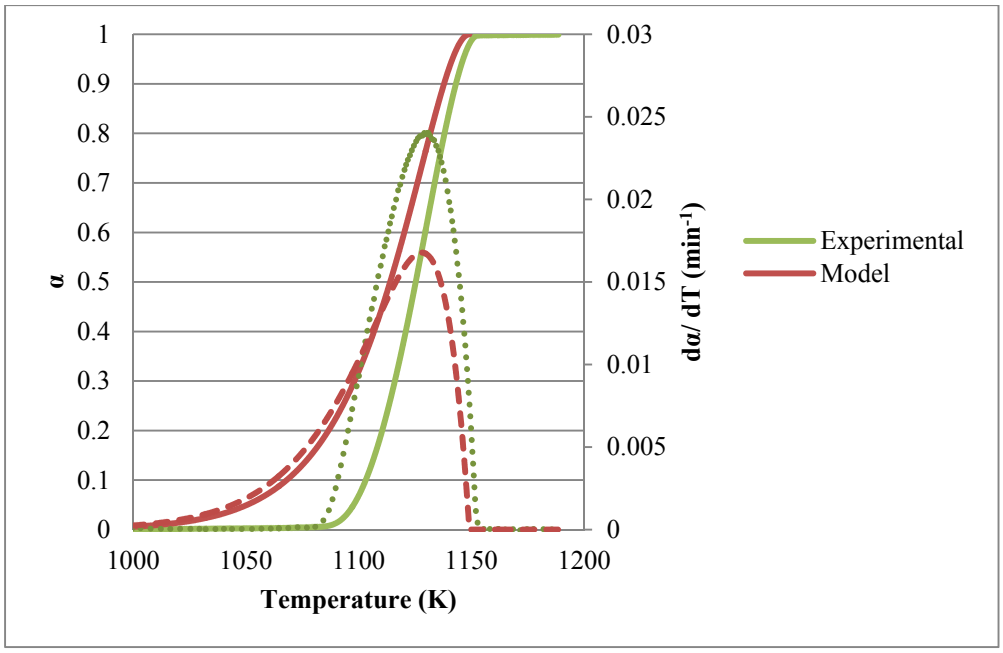

Figure 84. Comparison of Predicted (DTG-SIM) and Experimental α and dα/dT of Sample MSS-LS at 5 K/min in 50 kPa P_{CO_2}.

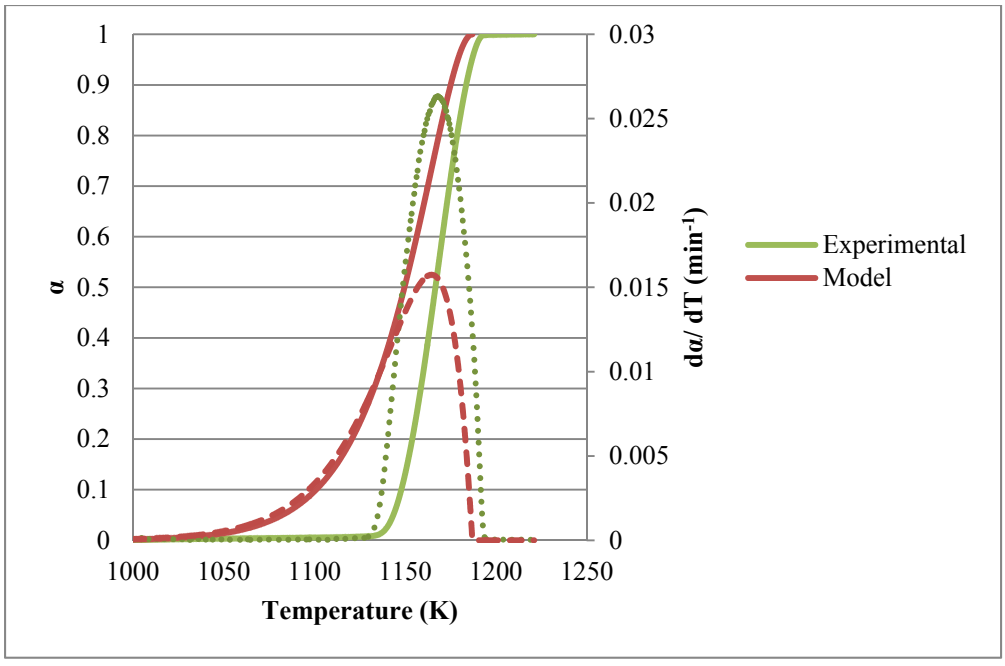

The deviations between the experimental and predicted values ranged between 30 and 100 %, Table 14. Based on these results, it was concluded that the DTG-curve-fitting approach is not a suitable technique to model non-isothermal calcination of limestone in CO_2.

Table 14. Deviations between Predicted (DTG-SIM) and Experimental Calcination Data in CO_2.

P_{CO_2} (kPa)	MRC-LS		MSS-LS	
	Deviation of α (%)	Deviation of dα/dT (%)	Deviation of α (%)	Deviation of dα/dT (%)
10	58.3	54.2	34.3	14.6
25	100.0	38.0	93.8	31.4
50	77.4	40.5	88.8	36.9

3.3.3.2 Coats-Redfern-Linearization-Based Method

The kinetic parameters obtained by the Coats-Redfern-Linearization method varied depending on the CO_2 partial pressure. The R^2 values of data plotted according to the dictate of Equation 32 were < 0.05 for an assumed n = 1. $R^2 > 0.999$ were; however, obtained when experimental data of sample MRC-LS (Figure 85) and sample MSS-LS (Figure 86) between conversions 15 and 75 % were plotted according to the dictate of Equation 31 for $n \neq 1$. The corresponding activation energy and frequency factor were calculated according to Equation 35 and Equation 36 and summarized in Table 15.

Figure 85. CR-Linearized Plot (Equation 31) for MRC-LS Calcination at 5 K/min and Various CO_2 Concentrations.

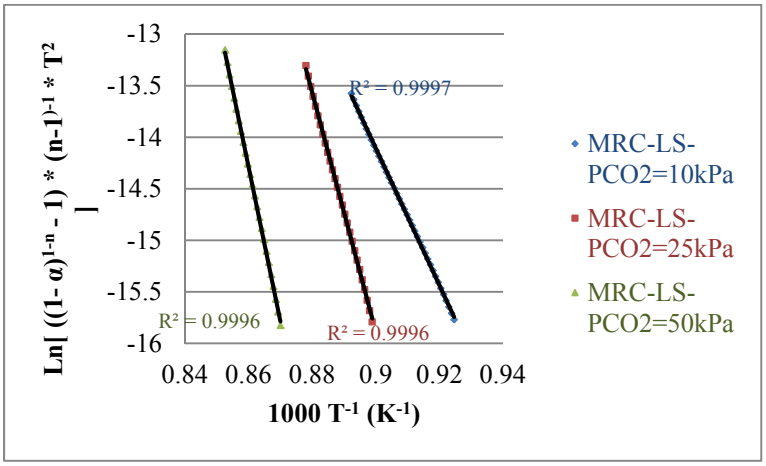

Figure 86. CR-Linearized Plot (Equation 31) for MRC-LS Calcination at 5 K/min and Various CO_2 Concentrations.

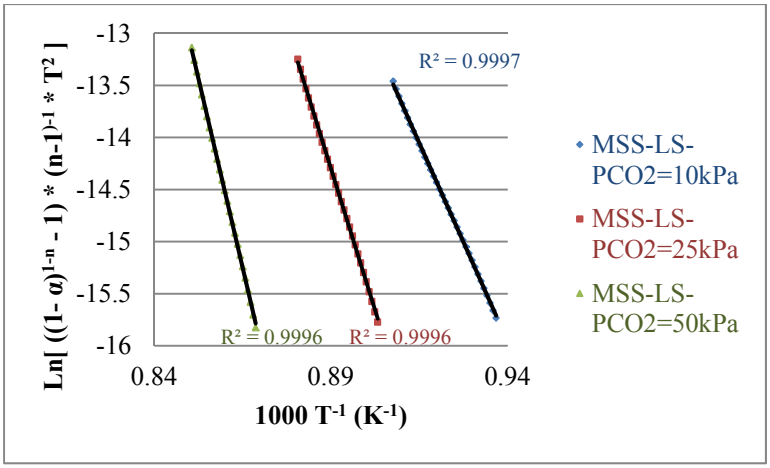

Table 15. The Values of Ea, n, and A Obtained by CR-Linearization Method.

P_{CO_2} (kPa)	MRC-LS			MSS-LS		
	Ea	A	n	Ea	A	n
	kJ/mol	min^{-1}		kJ/mol	min^{-1}	
10	551	2.11 E+25	1.2	633	5.37E+29	1.3
25	962	1.32 E+44	1.6	904	3.69E+41	1.7
50	1,243	3.21 E+55	2.0	1,205	5.07E+53	2.0

The activation energy varied between 551 and 1,243 kJ/mol in the ranges of CO_2 pressure employed. These values are too large for the thermal decomposition of limestone and cannot be explained by the enthalpy of reaction and have no physical meanings. However, they present "pseudo parameters" that can be used to predict the calcination rate of limestone in the temperature range and the partial pressure of CO_2 employed in the non-isothermal experiments. Predicted conversion and rate of conversion data by Equation 29 and Equation 30 based on the parameters listed in Table 15 for sample MRC-LS (Figure 87 to Figure 89) and sample MSS-LS (Figure 90 to Figure 92) showed deviations < 6 % between the experimental and the predicted

data. The deviations were calculated using Equation 39 and are summarized in Table 16. As seen in Figure 87 to Figure 92, the accuracies of the models decrease at near conversion > 90 %. It should be noted that predicating the calcination rates of the limestone outside the limits of the temperature region and CO_2 partial pressure used in the experiments is not valid.

Figure 87. Comparison of Predicted (CR) and Experimental α and dα/dT of Sample MRC-LS at 5 K/min in 10 kPa CO_2.

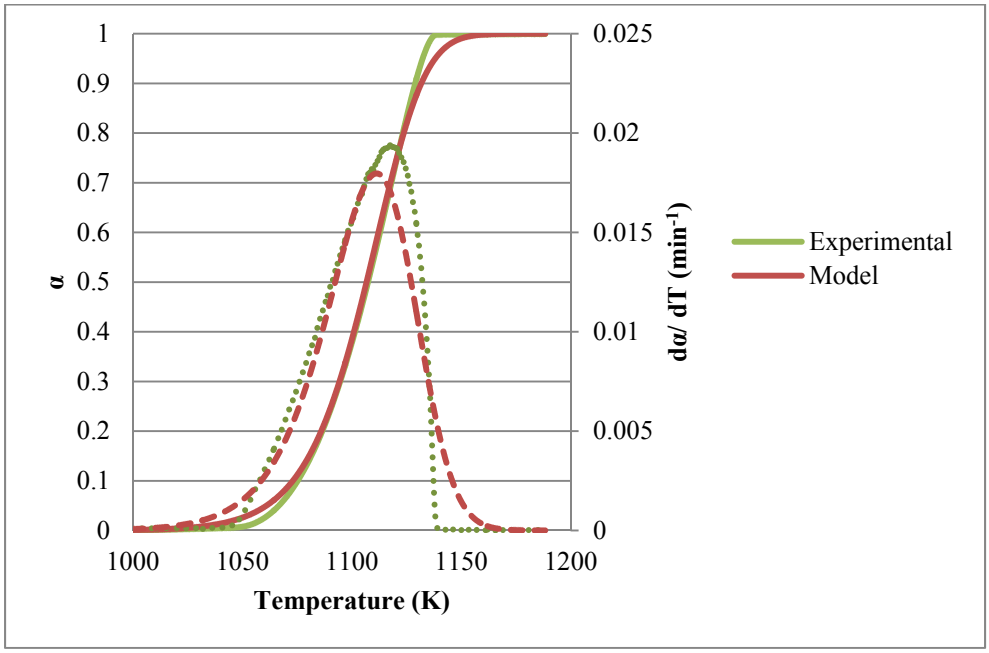

Figure 88. Comparison of Predicted (CR) and Experimental α and dα/dT of Sample MRC-LS at 5 K/min in 25 kPa CO_2.

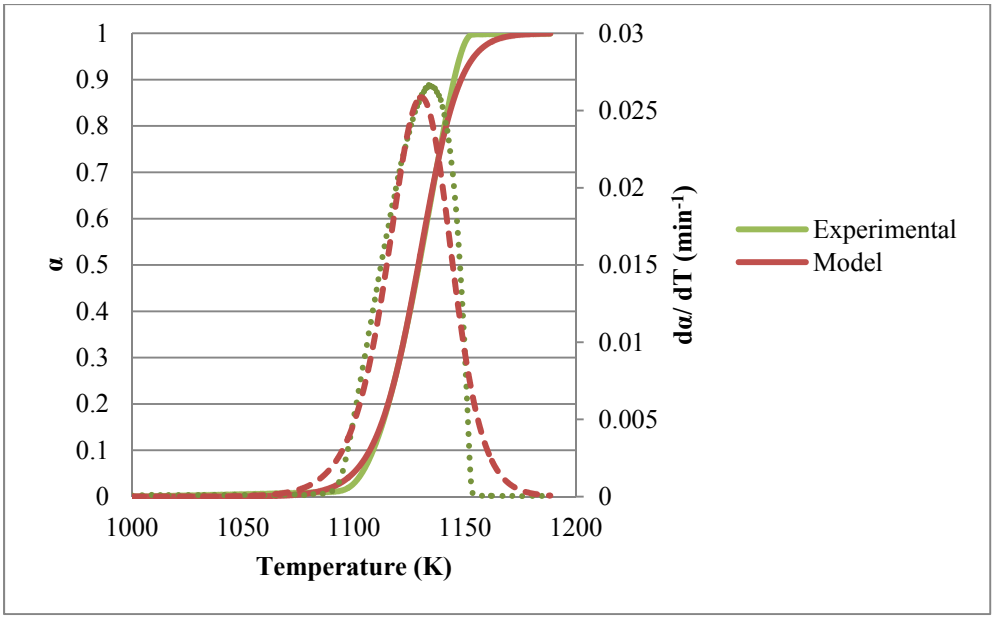

Figure 89. Comparison of Predicted (CR) and Experimental α and dα/dT of Sample MRC-LS at 5 K/min in 50 kPa CO_2.

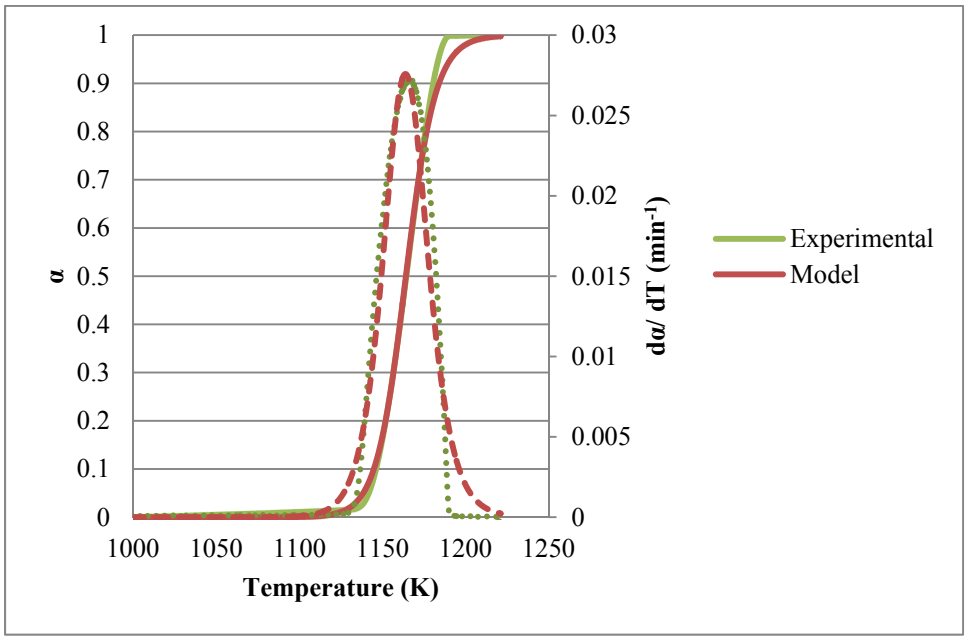

Figure 90. Comparison of Predicted (CR) and Experimental α and dα/dT of Sample MSS-LS at 5 K/min in 10 kPa CO_2.

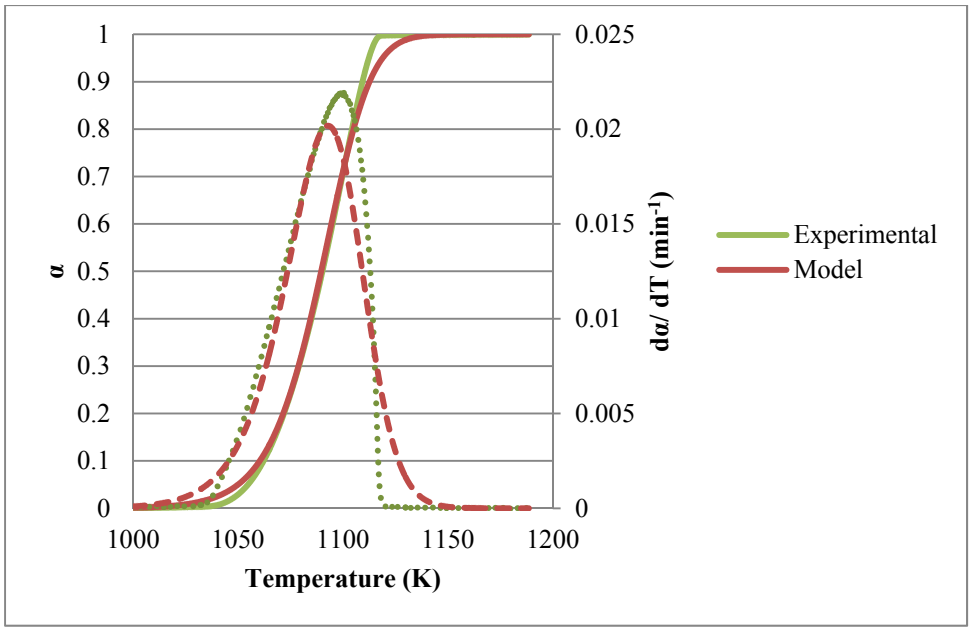

Figure 91. Comparison of Predicted (CR) and Experimental α and dα/dT of Sample MSS-LS at 5 K/min in 25 kPa CO_2.

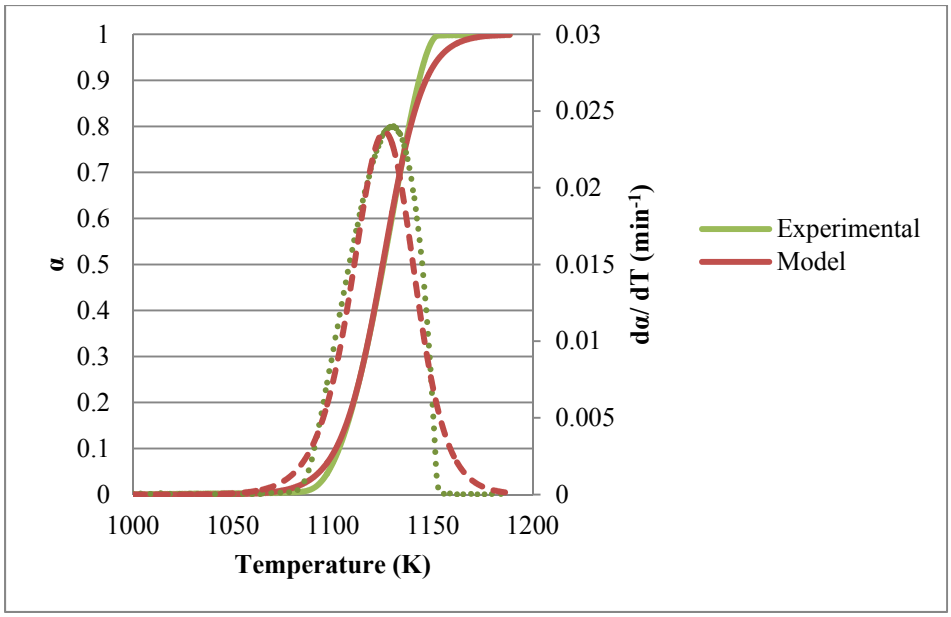

Figure 92. Comparison of Predicted (CR) and Experimental α and dα/dT of Sample MSS-LS at 5 K/min in 50 kPa CO_2.

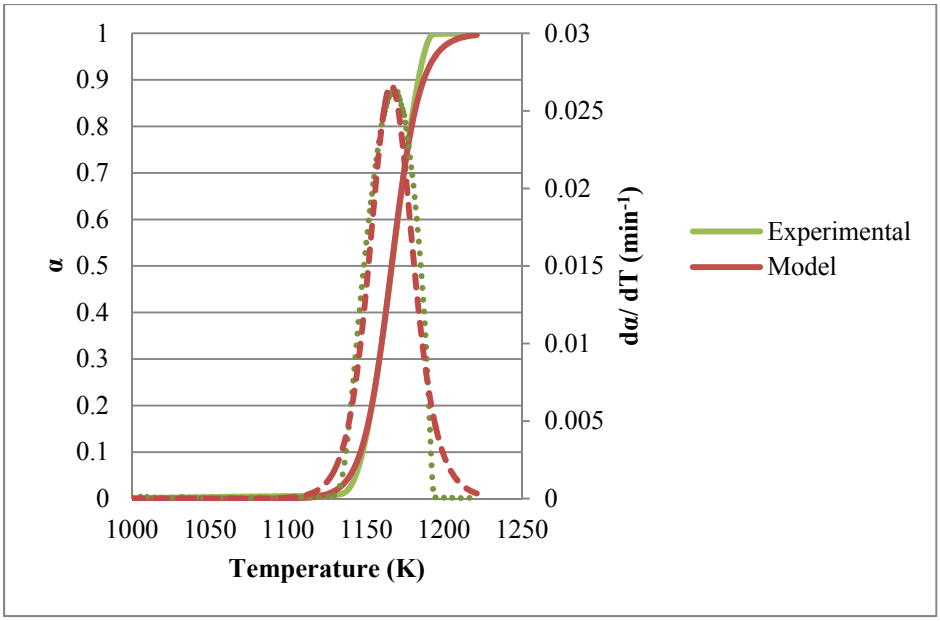

Table 16. Deviations between Predicted (Coats-Redfern) and Experimental Data for Sample MRC-LS and MSS-LS.

P_{CO_2} (kPa)	MRC-LS		MSS-LS	
	Deviation of α (%)	Deviation of dα/dT (%)	Deviation of α (%)	Deviation of dα/dT (%)
10	2.10	5.20	1.84	5.50
25	1.07	5.75	0.89	5.16
50	0.95	5.79	0.90	5.50

3.3.3.3 Criado-Linearization-Based Method

The recarbonation reaction of lime as described by the $(1-P_{CO_2}/P_{CO_2}^{*})$ term in Equation 28 was included in data analysis using the Criado-Linearization method. The linearized plots prepared according to the dictate of Equation 37 by assuming a reaction order to provide the best R^2 for each data set are presented in Figure 93 for sample MRC-LS and in Figure 94 for sample

MSS-LS. The activation energy and frequency factor calculated using Equation 35 and Equation 36 and are summarized in Table 17.

Figure 93. Criado-Linearized Plot (Equation 37) for MRC-LS Calcination at 5 K/min and Various CO_2 Concentrations.

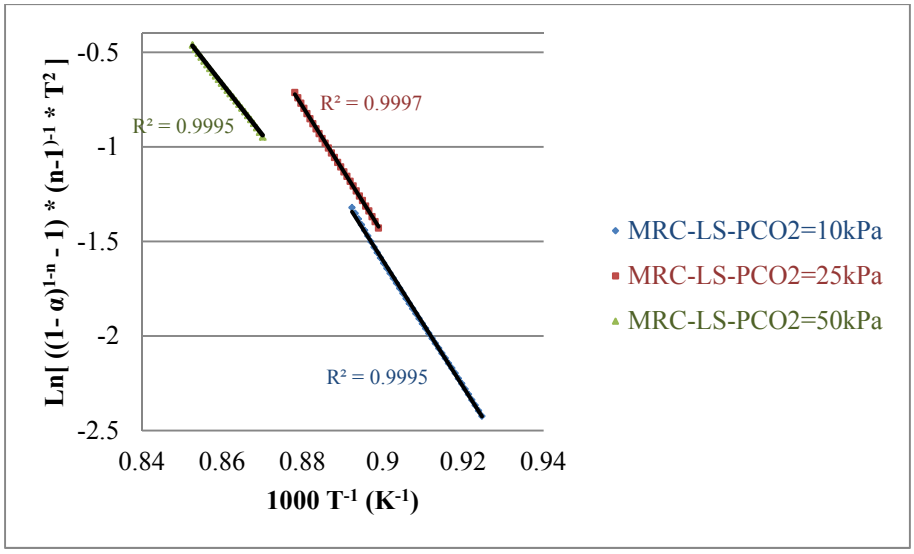

Figure 94. Criado-Linearized Plot (Equation 37) for MSS-LS Calcination at 5 K/min and Various CO_2 Concentrations.

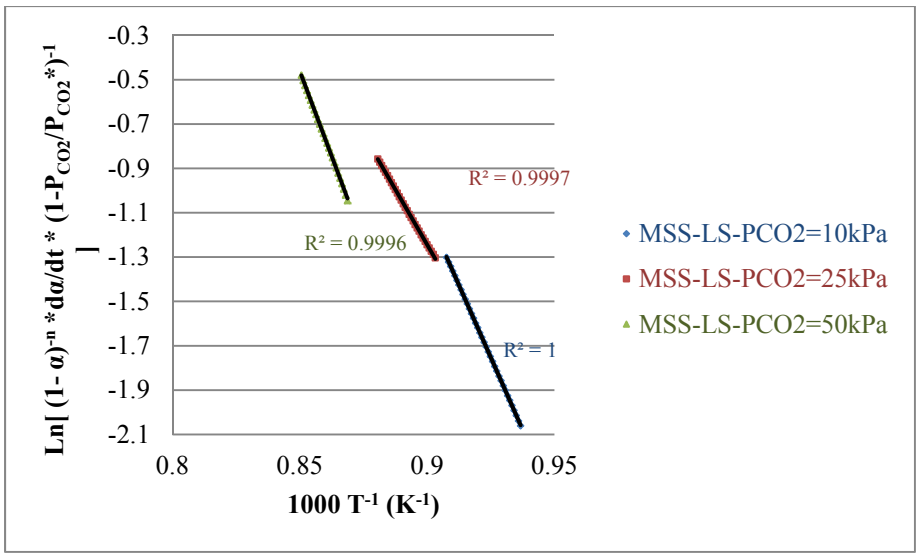

Table 17. The Values of Ea and A Obtained by Criado-Linearization Method

P_{CO_2} (kPa)	MRC-LS			MSS-LS		
	Ea	A	n	Ea	A	n
	kJ/mol	min^{-1}		kJ/mol	min^{-1}	
10	278	2.32 E+12	0.55	217	5.17E+09	0.40
25	279	3.00 E+12	0.55	166	1.78E+07	0.51
50	225	6.63 E+09	0.65	255	1.29E+11	0.70

The activation energies ranged between 225 and 278 kJ/mol and they are comparable to the values reported in the literature for the thermal decomposition of various limestone samples in CO_2 [Avila, et al., 2011]. The parameters listed in Table 17 were used to predict the conversion and rate of conversion of each limestone according to Equation 29 and Equation 30. The predicted data did not fit the experimental data well (Figure 95 to Figure 97 for MRC-LS and Figure 98 to Figure 100 for MSS-LS). Deviations between the experimental and predicted values calculated by Equation 39 were > 50 %, as shown in Table 18. Therefore, although the Criado Linearization method is amenable to inclusion of the recarbonation reaction, the predicted data did not fit the TGA calcination data obtained in this study.

Figure 95. Comparison of Predicted (Criado) and Experimental α and dα/dT of Sample MRC-LS at 5 K/min in 10 kPa CO_2.

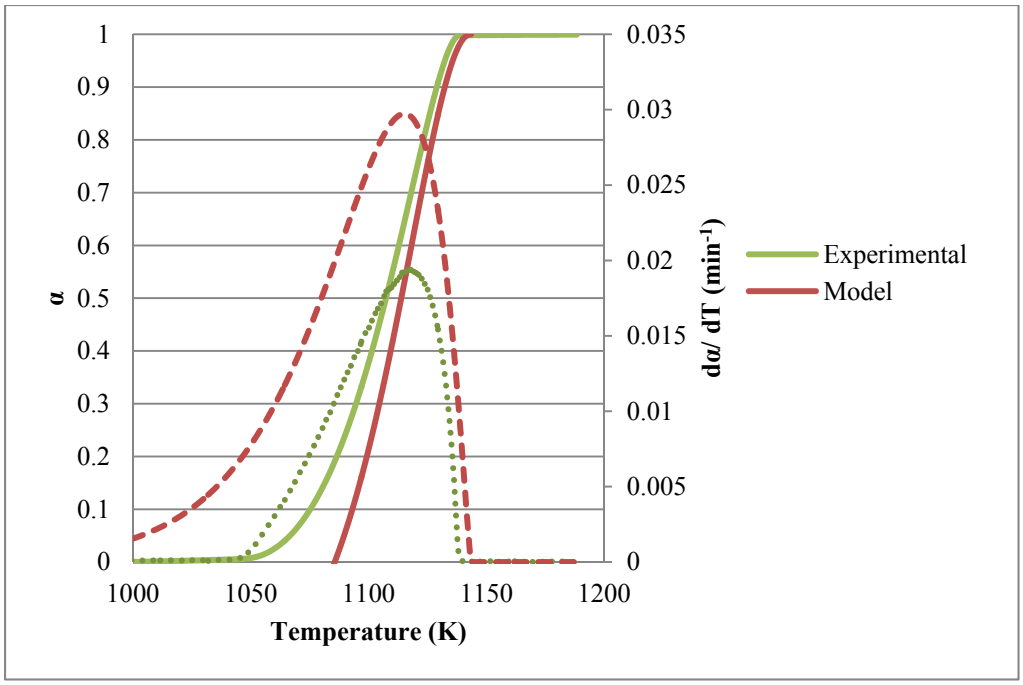

Figure 96. Comparison of Predicted (Criado) and Experimental α and dα/dT of Sample MRC-LS at 5 K/min in 25 kPa CO_2.

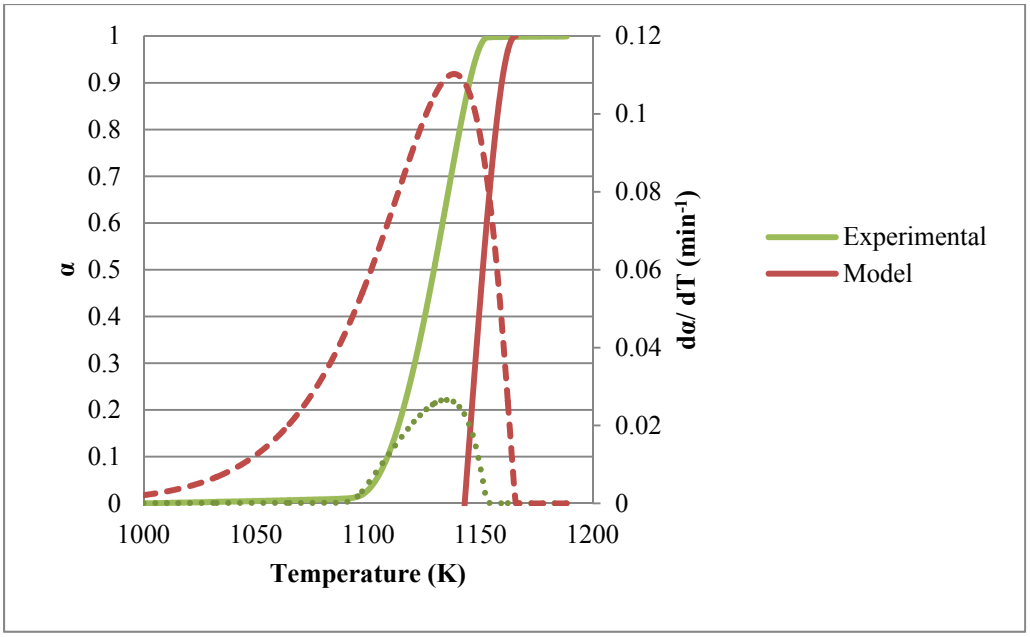

Figure 97. Comparison of Predicted (Criado) and Experimental α and dα/dT of Sample MRC-LS at 5 K/min in 50 kPa CO_2.

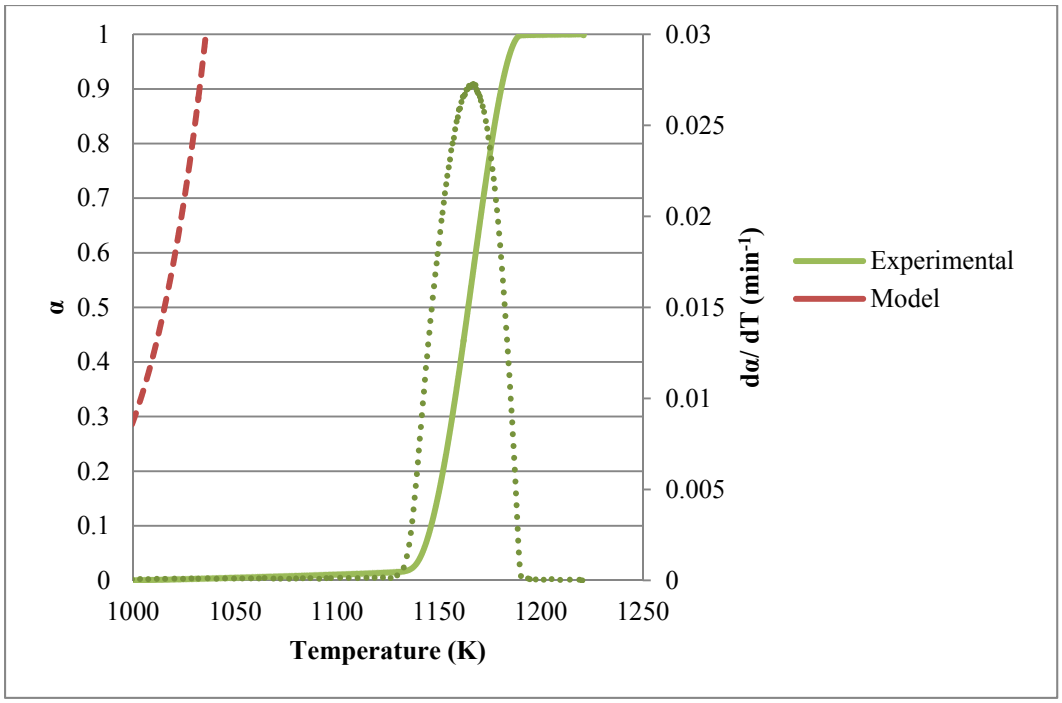

Figure 98. Comparison of Predicted (Criado) and Experimental α and dα/dT of Sample MSS-LS at 5 K/min in 10 kPa CO_2.

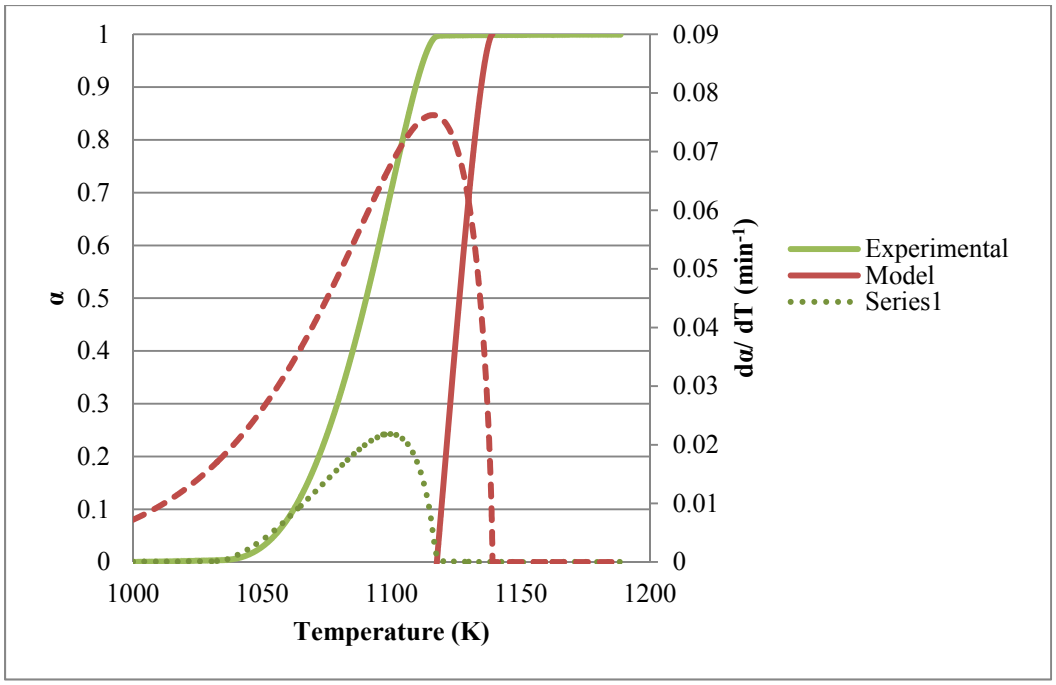

Figure 99. Comparison of Predicted (Criado) and Experimental α and dα/dT of Sample MSS-LS at 5 K/min in 25 kPa CO_2.

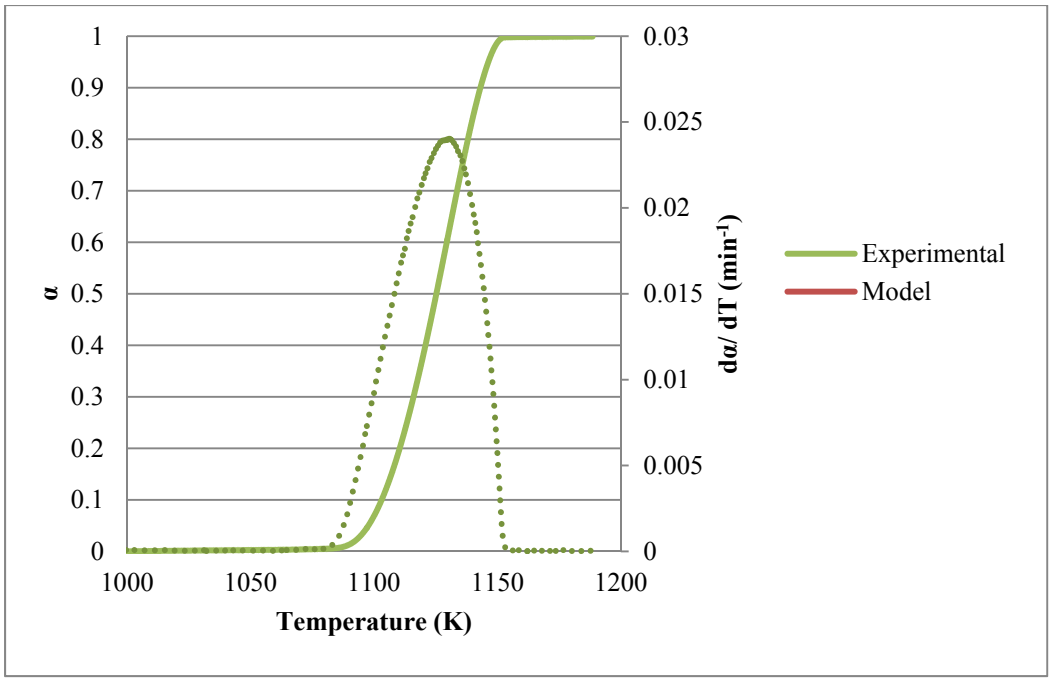

Figure 100. Comparison of Predicted (Criado) and Experimental α and dα/dT of Sample MSS-LS at 5 K/min in 50 kPa CO_2.

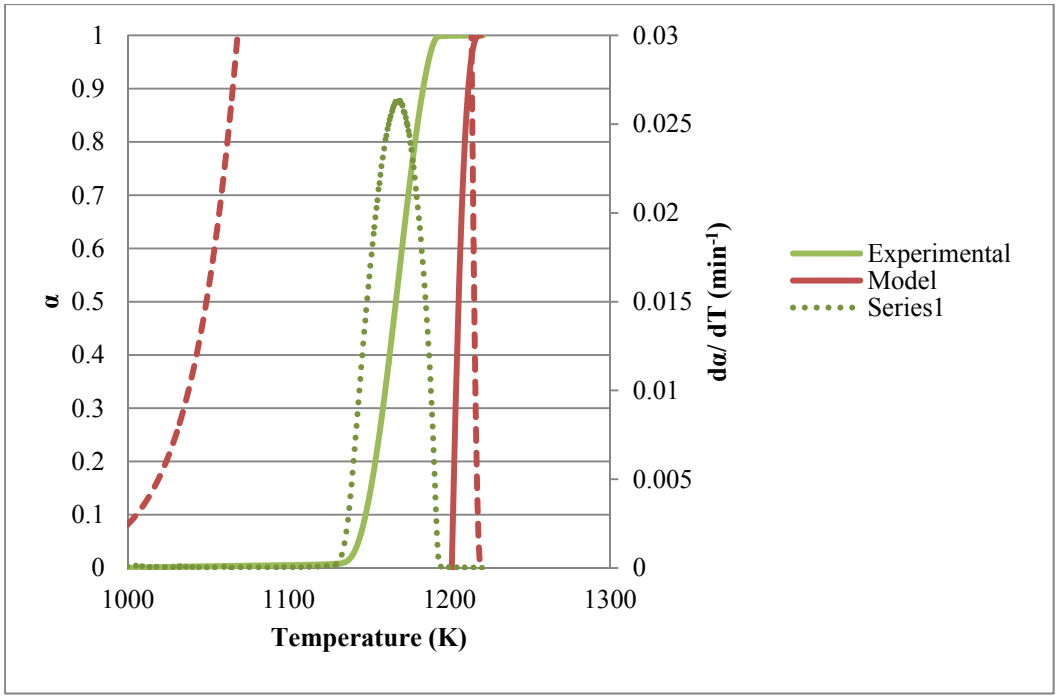

Table 18. Deviations between the Predicted (Criado) and Experimental Data in CO_2.

P_{CO_2} (kPa)	MRC-LS		MSS-LS	
	Deviation of α (%)	Deviation of dα/dT (%)	Deviation of α (%)	Deviation of dα/dT (%)
10	50	68	100	100
25	100	100	100	100
50	100	100	100	100

The summary of calcination kinetic parameters and maximum deviations in the predicted α and dα/dT using the kinetics parameters obtained by the three methods for calcination in CO_2 are summarized in Table 19. Apparent kinetics parameters determined using CR method yielded the lowest deviations between the models and experimental results.

Predicting calcination kinetics of limestone in CO_2 is more complicated than in N_2 in part because the recarbonation of lime occurs and CO_2 diffusional resistances in limestone/lime particle may not be ignored. Therefore, chemical reaction is not the only rate limiting step even at the early stage of the calcination reaction. A shrinking core model or other gas-solid reaction models which incorporate the effects of recarbonation may need to take mass transfer limitations into consideration to obtain improved kinetic information for the calcination of limestone in CO_2.

Table 19. Summary of Calculated Kinetics Parameters and Maximum Deviations of Predicted α and dα/dT for Sample MRC-LS and MSS-LS in CO_2 at Various Heating Rates.

Technique	Sample	P_{CO_2} (kPa)	Ea (kJ/mol)	A (min^{-1})	n	Max Deviation (%)
DTG SIM	MRC-LS	10	358	9.56 E+15	0.55	58
DTG SIM	MRC-LS	25	358	5.24 E+15	0.55	100

Table 19 (cont)

DTG SIM	MRC-LS	50	358	1.77 E+15	0.55	77
DTG SIM	MSS-LS	10	181	1.88 E+16	0.48	34
DTG SIM	MSS-LS	25	192	6.25 E+15	0.51	94
DTG SIM	MSS-LS	50	196	1.77 E+15	0.51	89
CR	MRC-LS	10	551	2.11 E+25	1.2	5
CR	MRC-LS	25	962	1.32 E+44	1.6	6
CR	MRC-LS	50	1,243	3.21 E+55	2.0	6
CR	MSS-LS	10	633	5.37E+29	1.3	6
CR	MSS-LS	25	904	3.69E+41	1.7	5
CR	MSS-LS	50	1,205	5.07E+53	2.0	6
Criado	MRC-LS	10	278	2.32 E+12	0.55	68
Criado	MRC-LS	25	279	3.00 E+12	0.55	100
Criado	MRC-LS	50	225	6.63 E+09	0.65	100
Criado	MSS-LS	10	217	5.17E+09	0.40	100
Criado	MSS-LS	25	166	1.78E+07	0.51	100
Criado	MSS-LS	50	255	1.29E+11	0.70	100

3.4 Predicting Extent of Calcination in a Flash Calciner

As was described earlier, a flash calcination refers to rapid thermal decomposition of limestone, often in a dilute-phase reactor such as an entrained-flow or a circulating fluid-bed reactor. To predict the extent of calcination in such a reactor, the kinetics of the calcination reaction is needed.

Equation 45 is the integral form of Equation 19 when assuming isothermal conditions. It describes the mass conversion of limestone to lime when both calcination and recarbonation reactions are considered. The $P_{CO_2}^*$ term (the equilibrium calcination partial pressure at a given temperature) in Equation 45 is substituted by Equation 28 to obtain Equation 46. Equation 46 can be used to calculate the EC of a limestone at a given reaction temperature and CO_2 partial pressure using the values of E, A, and n predicted from the thermal decomposition reaction of limestone in N_2.

Equation 45:
$$\boldsymbol{\alpha = 1 - \left[(n-1)\left(1 - \frac{P_{CO_2}}{P_{CO_2}^*}\right) A\, e^{-\frac{Ea}{RT}}\, t\right]^{\frac{1}{1-n}}}$$

Equation 46:
$$\boldsymbol{\alpha = 1 - \left[(n-1)\left(1 - \frac{P_{CO_2}}{B\, e^{-\frac{F}{RT}}}\right) A\, e^{-\frac{Ea}{RT}}\, t\right]^{\frac{1}{1-n}}}$$

The extent of calcination of sample MRC-LS and sample MSS-LS were calculated using Equation 46 (ISO T Model). The TGA kinetic parameters, determined for the thermal decomposition of each limestone sample in N_2 by the DTG-SIM method (Table 6), were used to calculate the extent of calcination. The following assumptions were made:

1. Calcination reactor operates under an isothermal condition at atmospheric pressure (constant calcination temperature and total pressure of 101 kPa).
2. Uniform CO_2 concentration in the reactor, no radial or axial CO_2 concentration gradients.
3. Limestone particles < 90 μm are rapidly heated to the calcination gas temperature. The particle heat up time (0.1 seconds) << calcination residence time of 1 - 3 seconds (Figure 54)
4. External and intra-particle heat and mass transports are negligible.
5. Extent of calcination is not impacted by sintering and pore plugging phenomena.
6. Thermal decomposition reaction of limestone is kinetically controlled.
7. All particles are entrained in the calcination gas; thus, the residence time of a particle can be calculated from the average gas velocity in the reactor.

Extent of the calcination of sample MRC-LS and sample MSS-LS calculated at different temperatures, residence times, and partial pressures of CO_2 according to Equation 46 are presented in Figure 101 to Figure 114.

Figure 101. EC of Sample MRC-LS at 825 K.

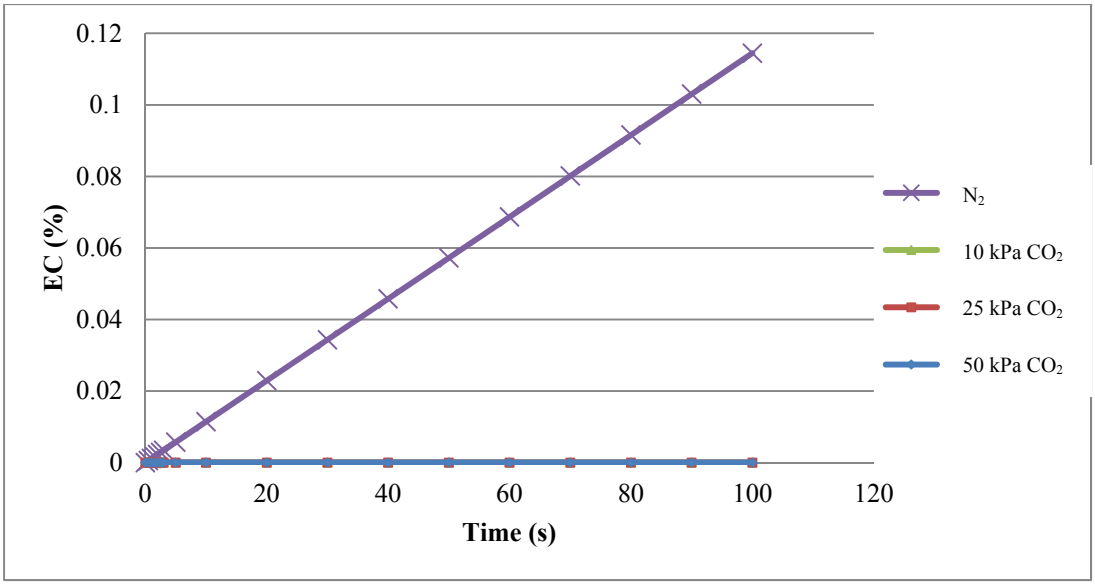

Figure 102. EC of Sample MRC-LS at 950 K.

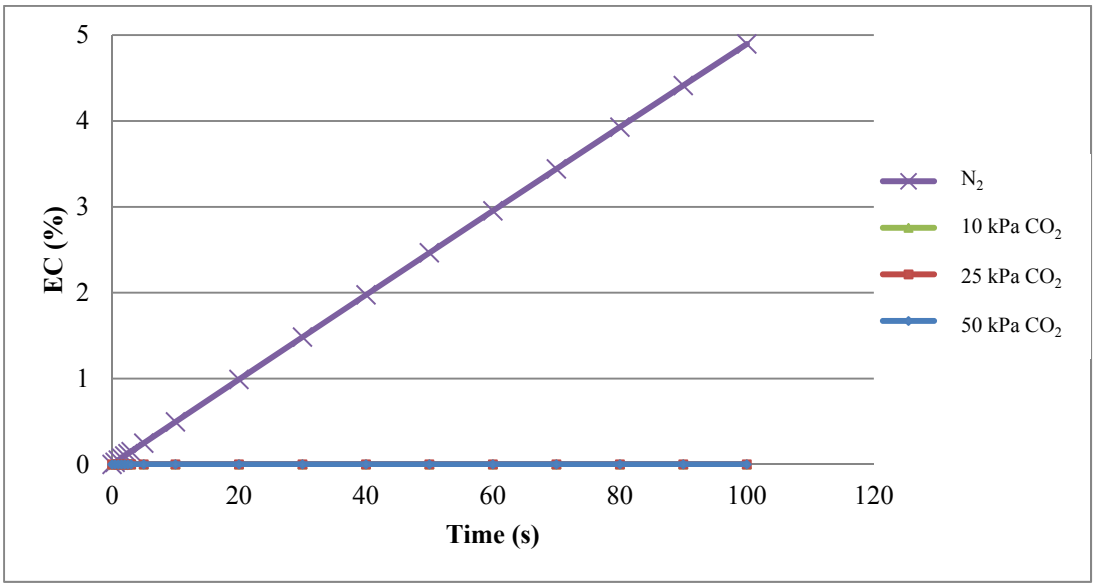

Figure 103. EC of Sample MRC-LS at 1,050 K.

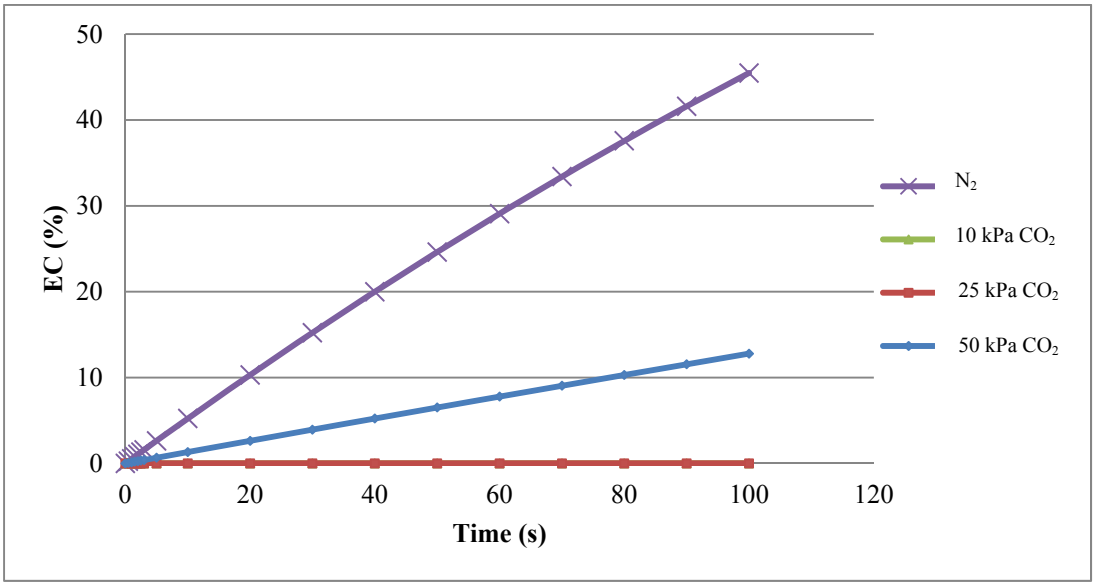

Figure 104. EC of Sample MRC-LS at 1,120 K.

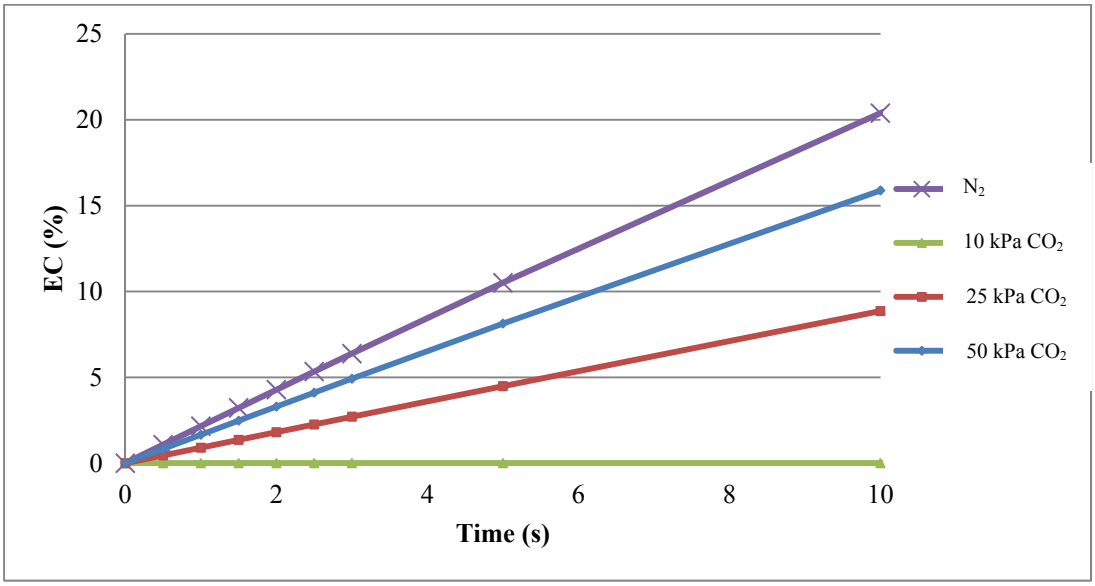

Figure 105. EC of Sample MRC-LS at 1,180 K.

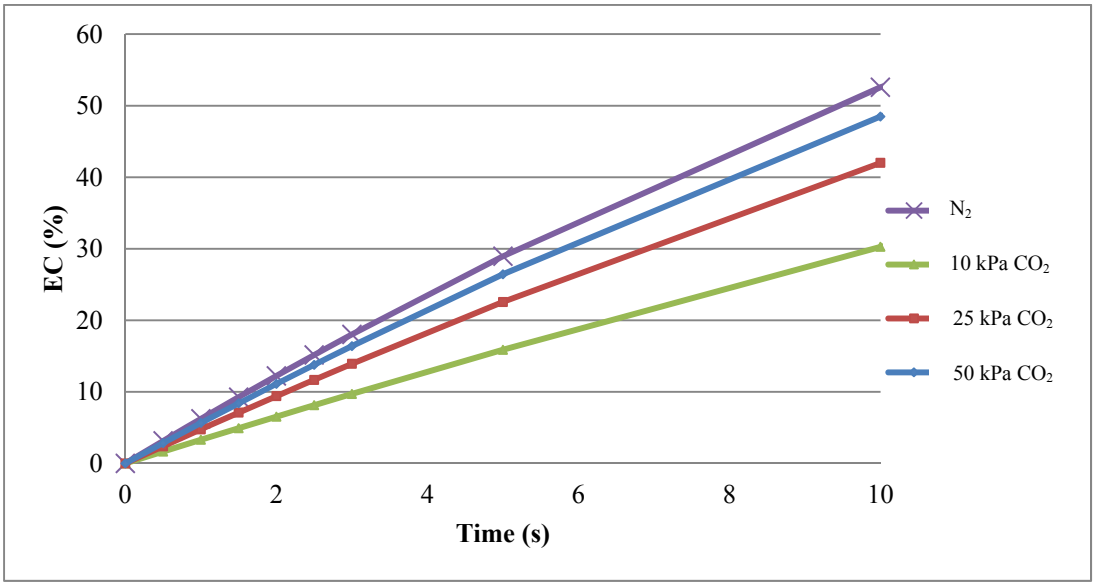

Figure 106. EC of Sample MRC-LS at 1,250 K.

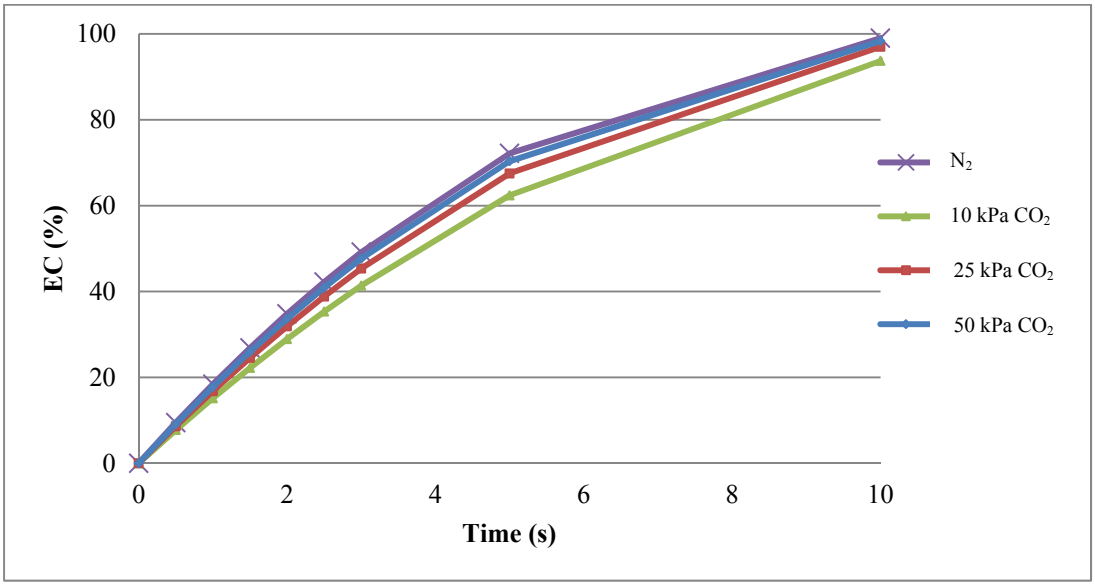

Figure 107. EC of Sample MRC-LS at 1,350 K.

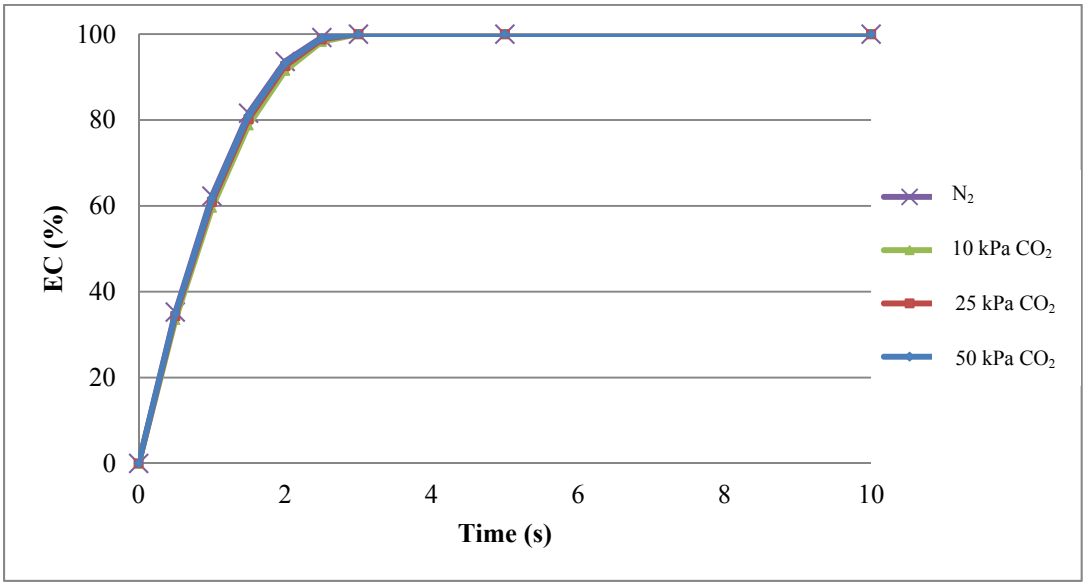

Figure 108. EC of Sample MSS-LS at 825 K.

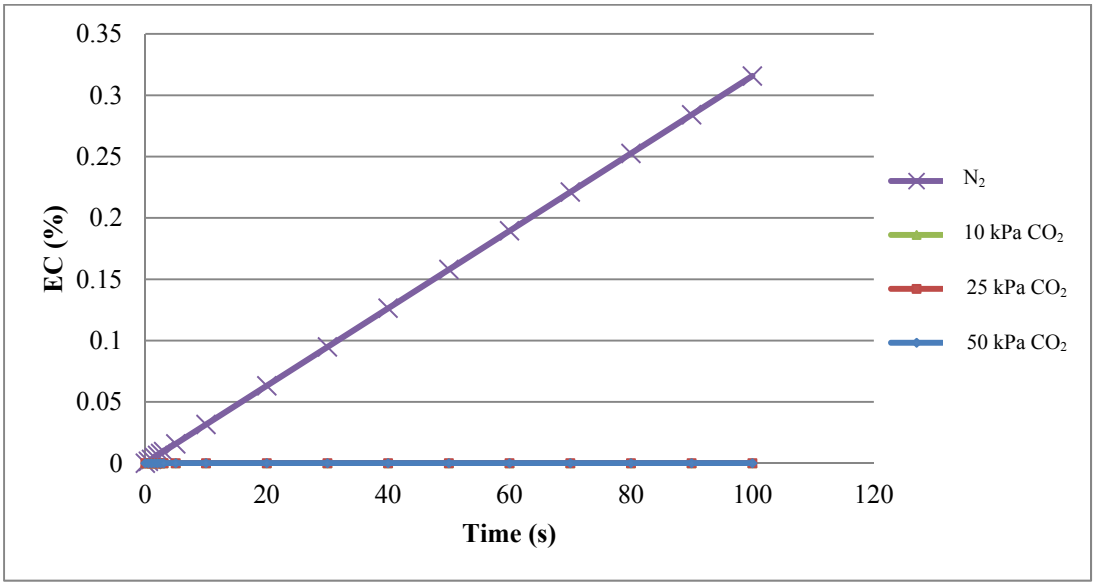

Figure 109. EC of Sample MSS-LS at 950 K.

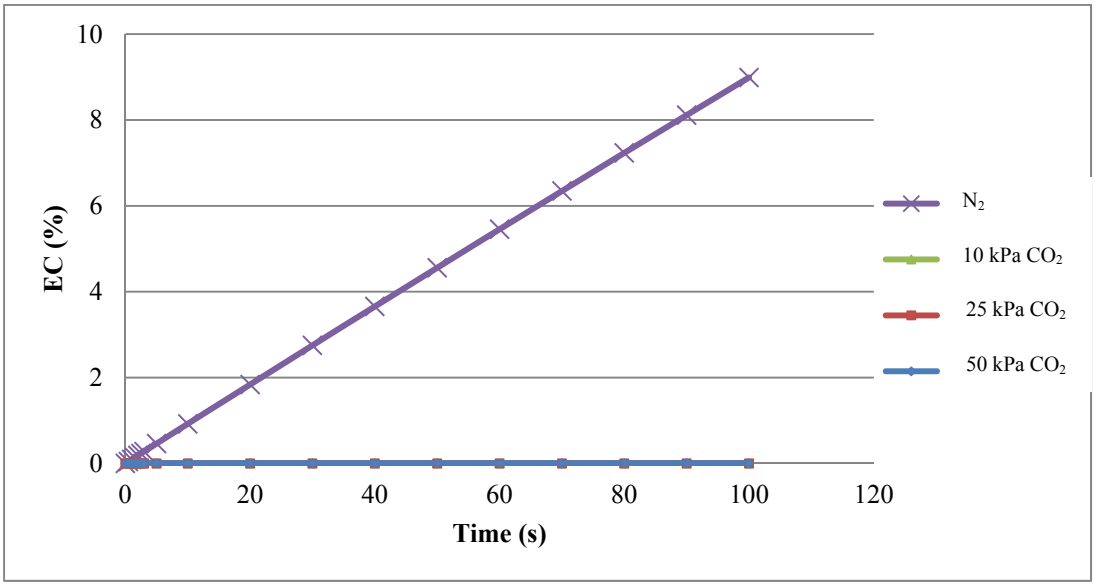

Figure 110. EC of Sample MSS-LS at 1,050 K.

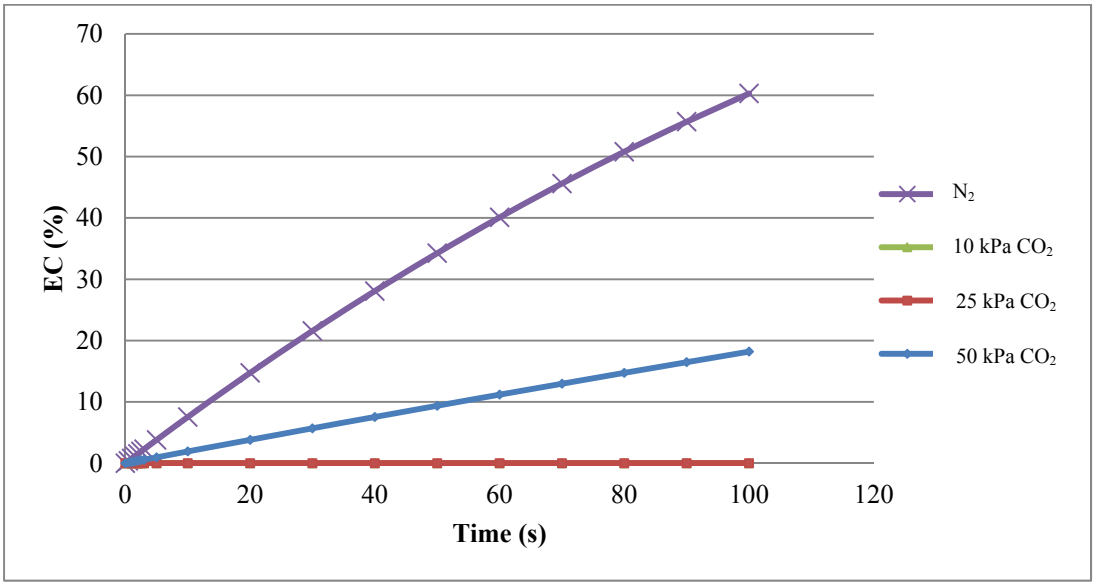

Figure 111. EC of Sample MSS-LS at 1,120 K.

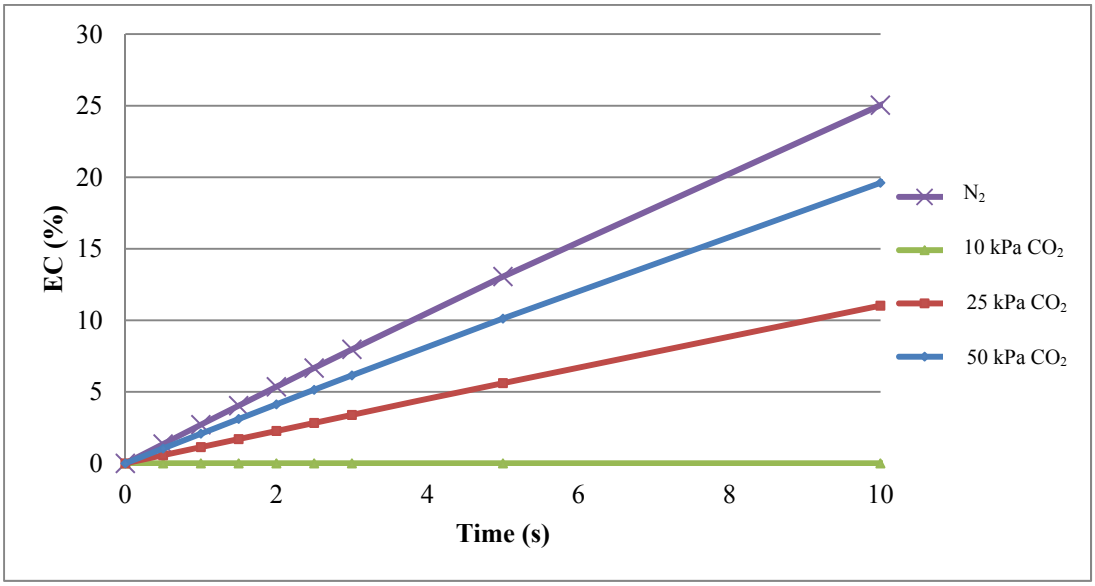

Figure 112. EC of Sample MSS-LS at 1,180 K.

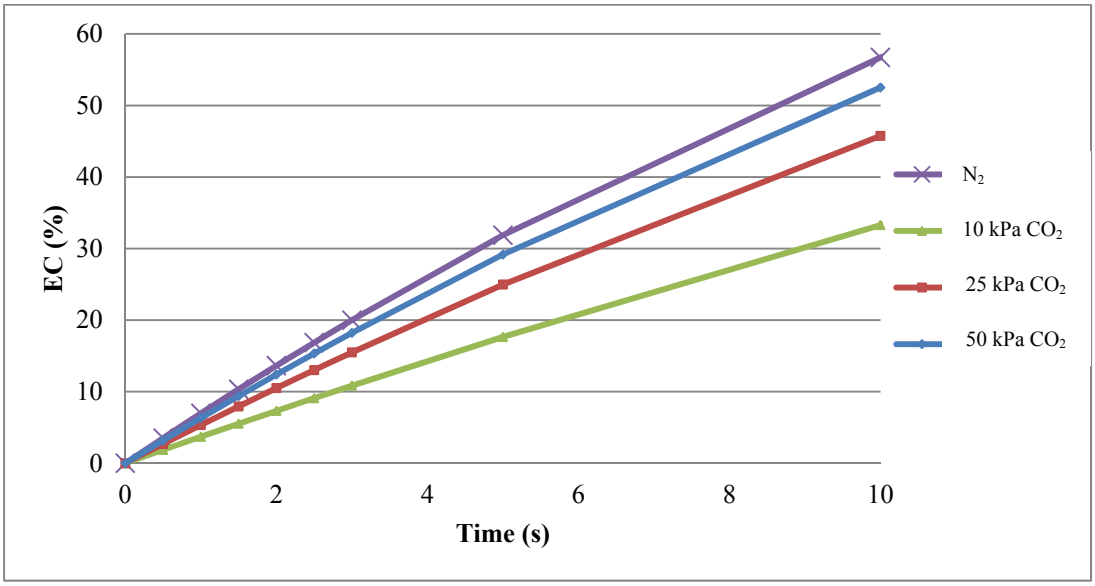

Figure 113. EC of Sample MSS-LS at 1,250 K.

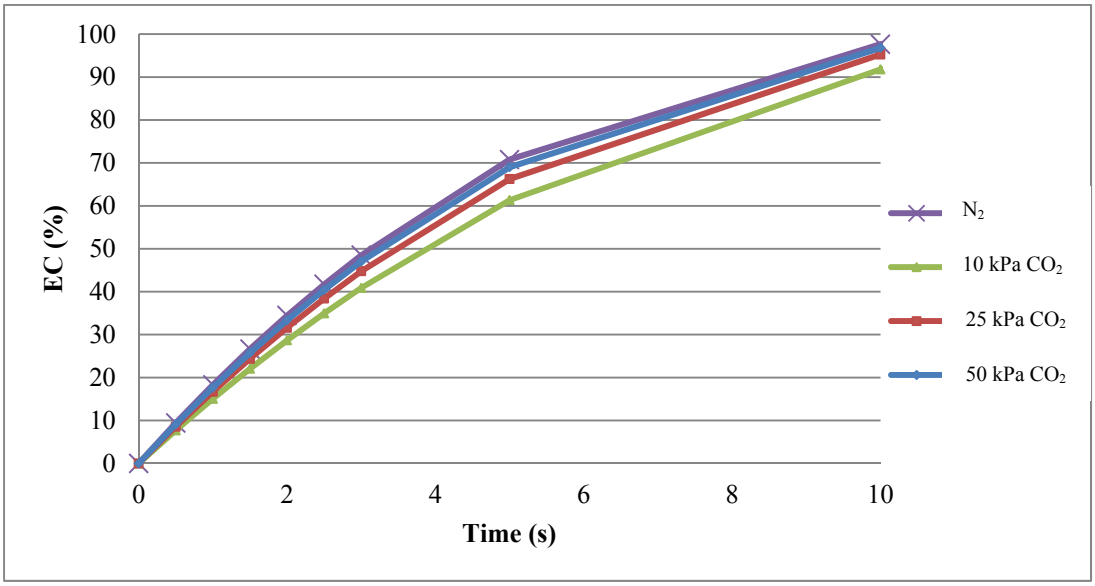

Figure 114. EC of Sample MSS-LS at 1,350 K.

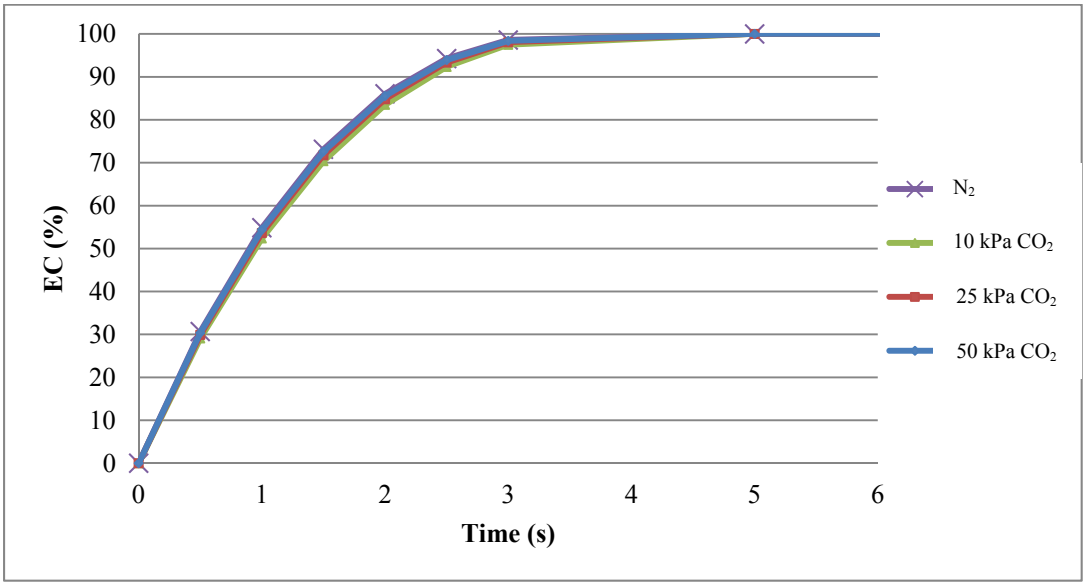

The following conclusions can be drawn from examination of data presented in Figure 101 to Figure 114.

1. The rate of calcination of sample MSS-LS is higher than sample MRC-LS at below 1,250 K and lower at above 1,250 K.
2. No conversions at 825 K in N_2 in 100 seconds (Figure 101 and Figure 108).

3. No conversion at 925 K in 10, 25, and 50 kPa CO_2 and 100 seconds; 5 % conversion at 925 K in N_2 and 60 seconds (Figure 101 and Figure 108).
4. Less than 20 % conversions at 1050 K in 10 kPa CO_2 and 100 seconds (Figure 103 and Figure 110).
5. Between 60-70 % conversions at 1,250 K in 10, 20, and 50 kPa CO_2 and 5 seconds (Figure 106 and Figure 113).
6. Conversions > 95 % at 1,350 K in 10, 20, and 50 kPa CO_2 and 2.5 seconds (Figure 107 and Figure 114).
7. Increasing the temperature diminishes the impact of CO_2 pressure on the calcination reaction. Comparable conversions (83-85 %) resulted at 1,350 K in N_2 and 50 kPa CO_2 and 2 seconds (Figure 107 and Figure 114).

3.5 Predicting Extent of Calcination in SAP

Theoretically, ISO T Model over-estimates the extent of calcination of limestone in SAP for several reasons. First, as was shown in Figure 115, SAP was not operated under isothermal conditions and the gas temperature decreased along the length of the reactor. As the temperature is lowered below the equilibrium calcination temperature, the recarbonation reaction rather than calcination reaction will occur. However, as shown in Figure 101 to Figure 114, the ISO T Model under estimated the extent of calcination of samples MRC-LS and MSS-LS at temperature below 1,250 K.

Second, ISO T Model describes limestone calcination in an ideal mixed reactor where the gas flow in uniform and mass and heat transfer transports between the limestone particles and the calcination gas as well as intra-particle transports do not impact the calcination kinetics. In reality; however, gas-gas and gas-solid mixing processes may not be ideal under the conditions SAP was operated. Third, ISO T Model assumes that all of the limestone particles are entrained in the gas and therefore the residence time of a limestone particle in SAP is equal to the average gas residence time. However, the actual residence time of a limestone particle in the SAP depends on its size. Therefore, the extent of calcination will be impacted by the size of the limestone particle; residence time of a particle decreases with increasing size.

An alternative model, NONISO T, was considered. NONISO T model incorporates the measured gas temperatures in the SAP instead of assuming an isothermal condition to calculate the ECs. The temperature profiles in the SAP at different operating conditions were presented in Figure 115. The procedure to calculate the EC of limestone is as follows:

1. Select a temperature profile in Figure 115. The profiles are labeled according to the measured temperature at T_1 location. Each data point present the measured temperature at a location in the SAP at a given residence time. The residence time is based on the average gas velocity. It is assumed that the gas and particle residence times are equal.
2. For each temperature profile, average temperatures at several small residence time increments are obtained. The averages temperature for each time interval is assumed constant (isothermal).
3. EC (conversion) at each average temperature and residence time from step 2 is calculated using Equation 46 and the kinetic parameters obtained in the TGA experiments in N_2 by the DTG-SIM method (Table 6).
4. Repeat steps 1-3 for other temperature profiles and CO_2 pressures.
5. Plot EC vs residence time.

Predicted ECs for sample MRC-LS are presented in Figure 116 to Figure 122 and for sample MSS-LS in Figure 123 to Figure 129. Theoretically, at a CO_2 pressure of 10 kPa, the pressure calculated based on the propane combustion, limestone decomposition in the SAP only should occur at temperatures above 1,025 K. The predicted ECs for the two limestone samples indicate less than 2 % conversion in one second at 1,120 K and 10 kPa CO_2 pressure (Figure 119 and Figure 126). Additionally, the predicted data clearly show the negative impact of CO_2 pressure on conversion at different calcination temperatures. The maximum conversion at 10 kPa CO_2 for both samples occurred at 1,350 K; about 70 % for sample MRC-LS and 60 % for sample MSS-LS. The rate of calcination of sample MSS-LS is faster than sample MRC-LS at below 1,300 K and slower above 1,300K.

Figure 115. Temperature Profile across SAP at Different Residence Times.

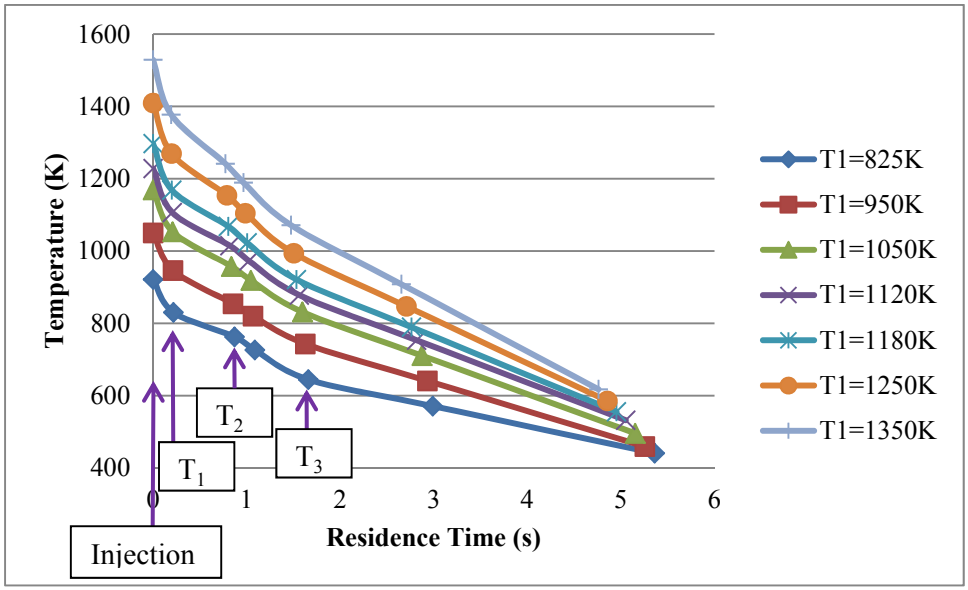

Figure 116. EC Prediction for Sample MRC-LS by NONISO T Model at T_1 = 825 K.

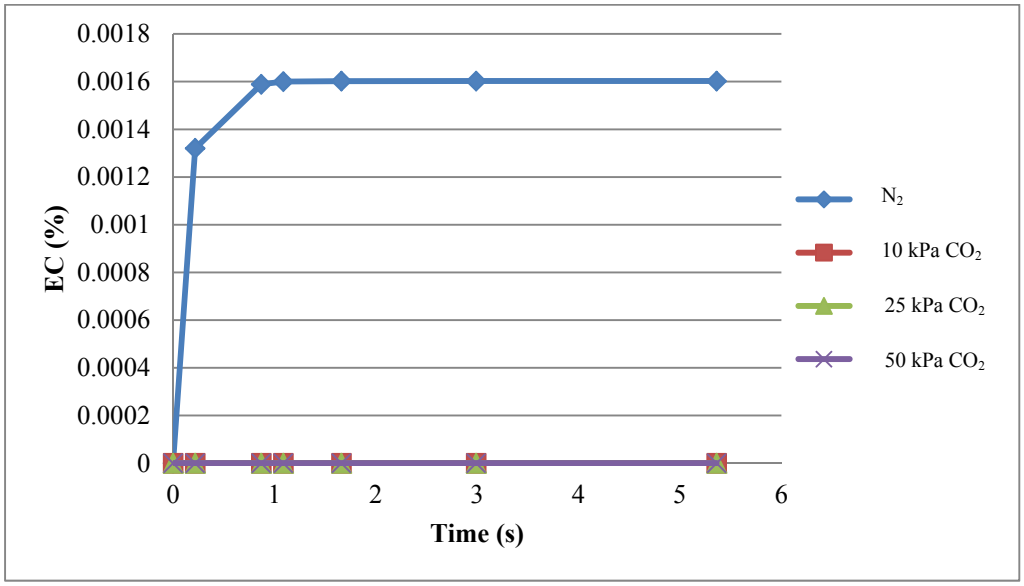

Figure 117. EC Prediction for Sample MRC-LS by NONISO T Model at T_1 = 950 K.

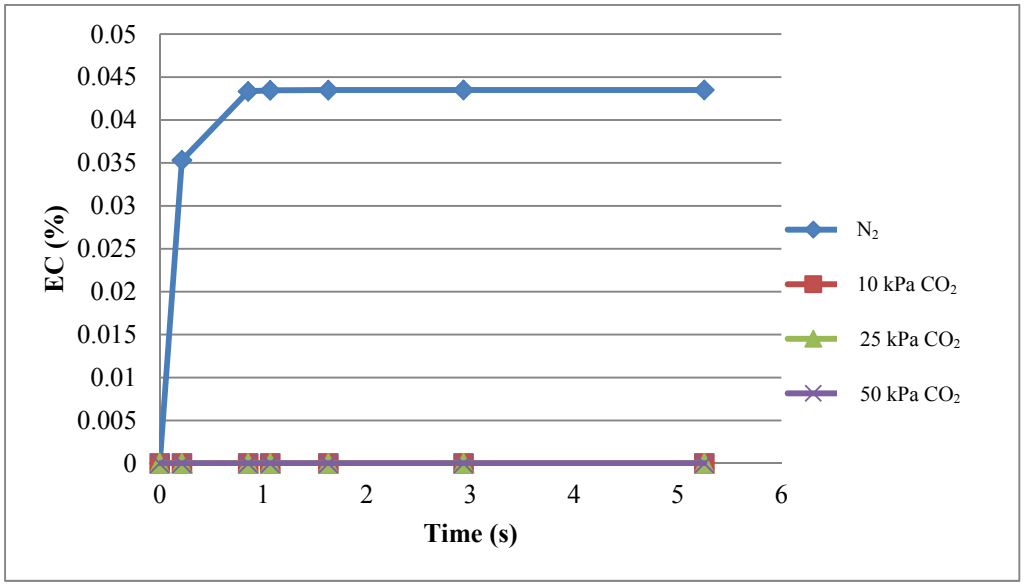

Figure 118. EC Prediction for Sample MRC-LS by NONISO T Model at T_1 = 1,050 K.

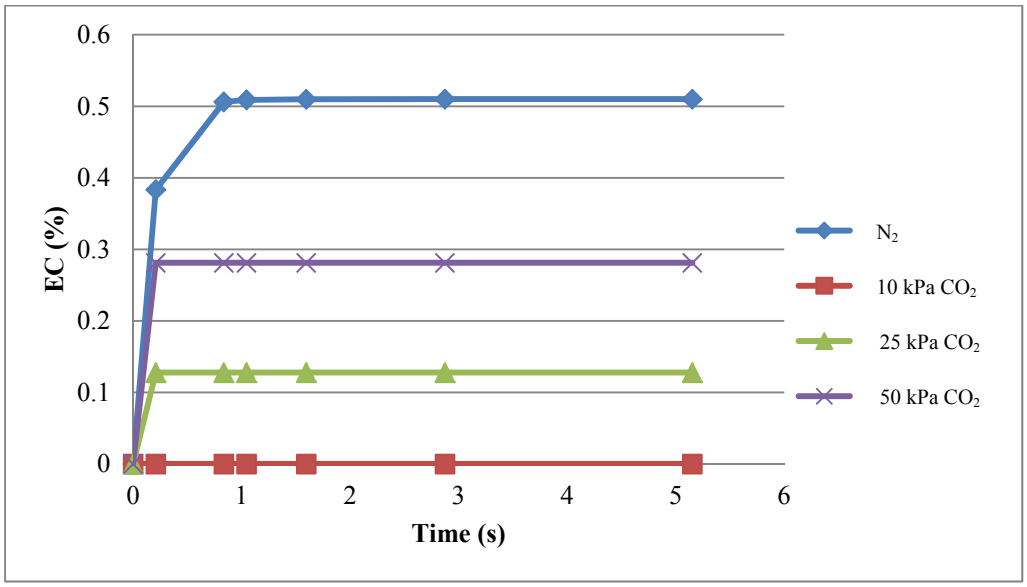

Figure 119. EC Prediction for Sample MRC-LS by NONISO T Model at T_1 = 1,120 K.

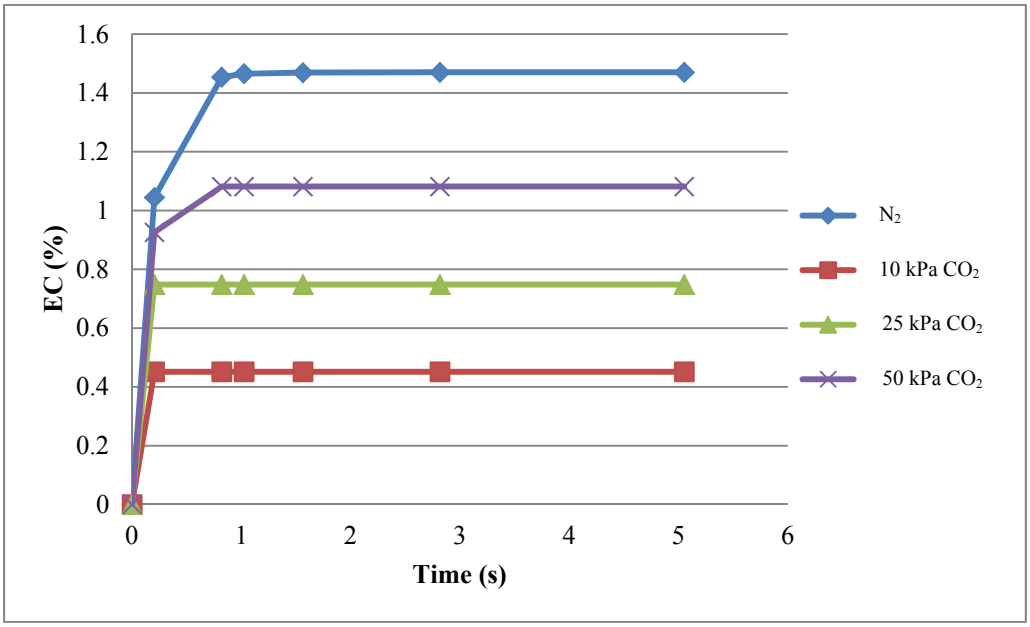

Figure 120. EC Prediction for Sample MRC-LS by NONISO T Model at T_1 = 1,180 K.

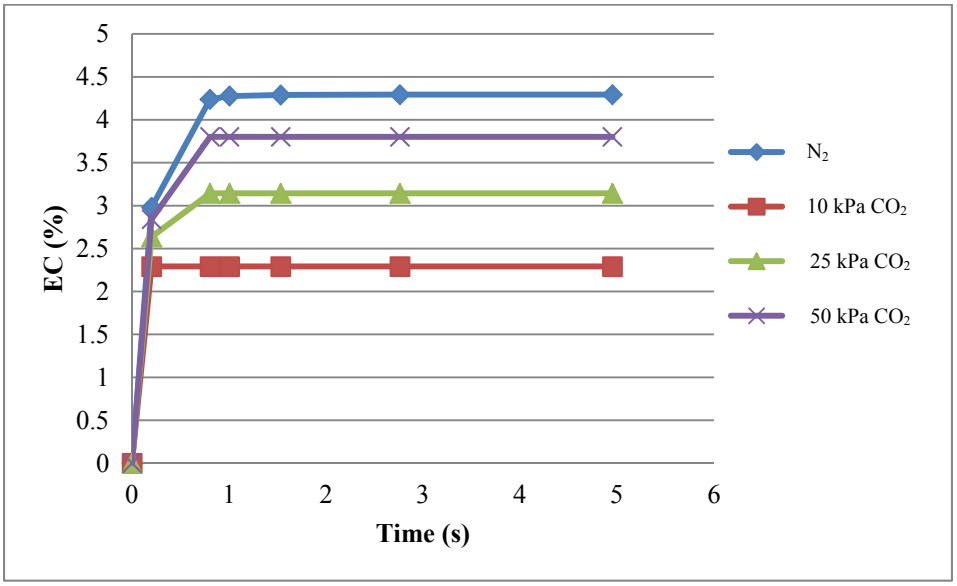

Figure 121. EC Prediction for Sample MRC-LS by NONISO T Model at T_1 = 1,250 K.

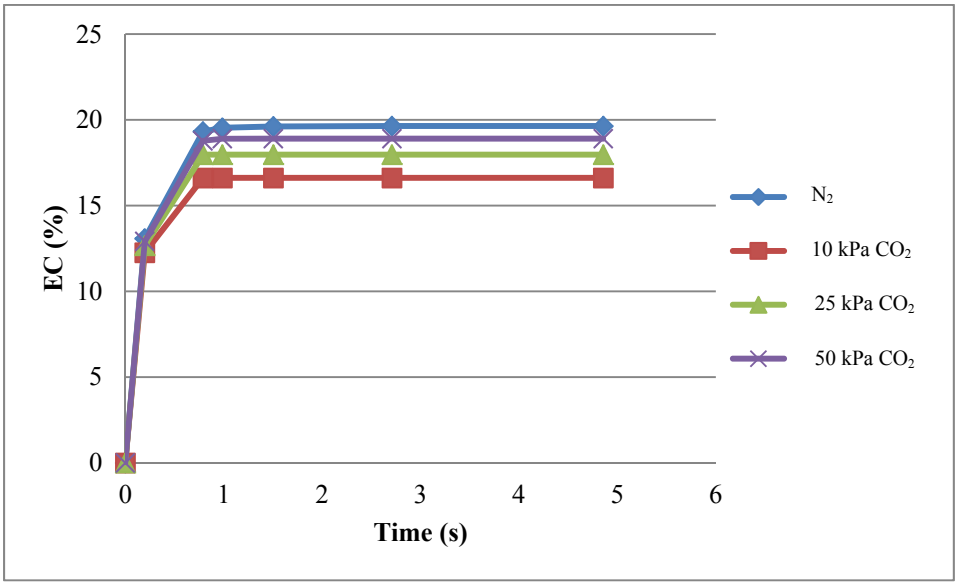

Figure 122. EC Prediction for Sample MRC-LS by NONISO T Model at T_1 = 1,350 K.

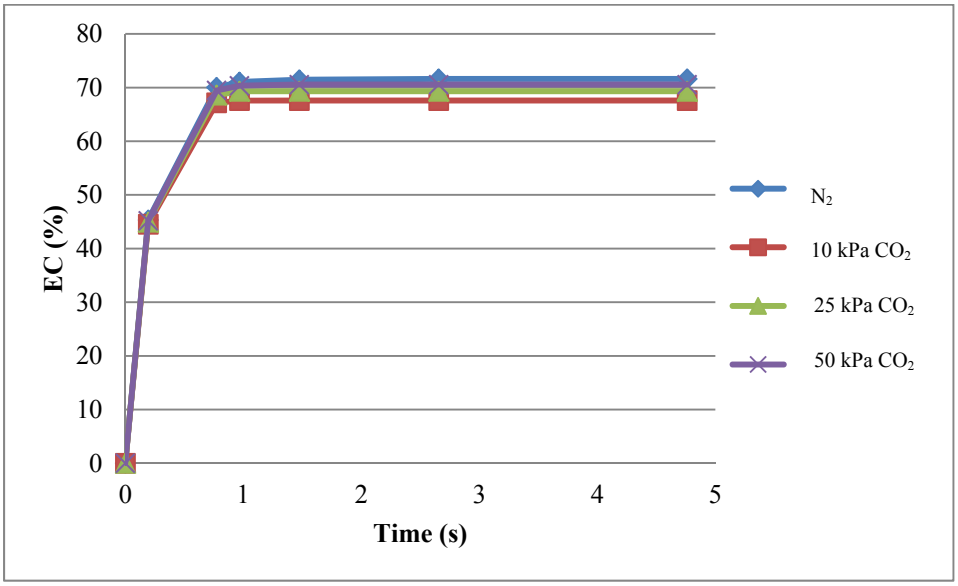

Figure 123. EC Prediction for Sample MSS-LS by NONISO T Model at T_1 = 825 K.

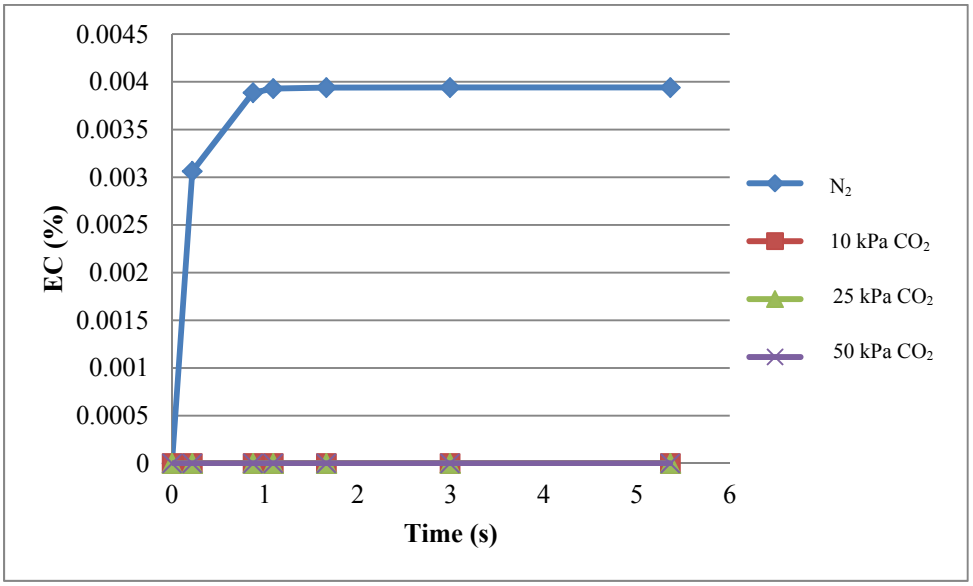

Figure 124. EC Prediction for Sample MSS-LS by NONISO T Model at T_1 = 950 K.

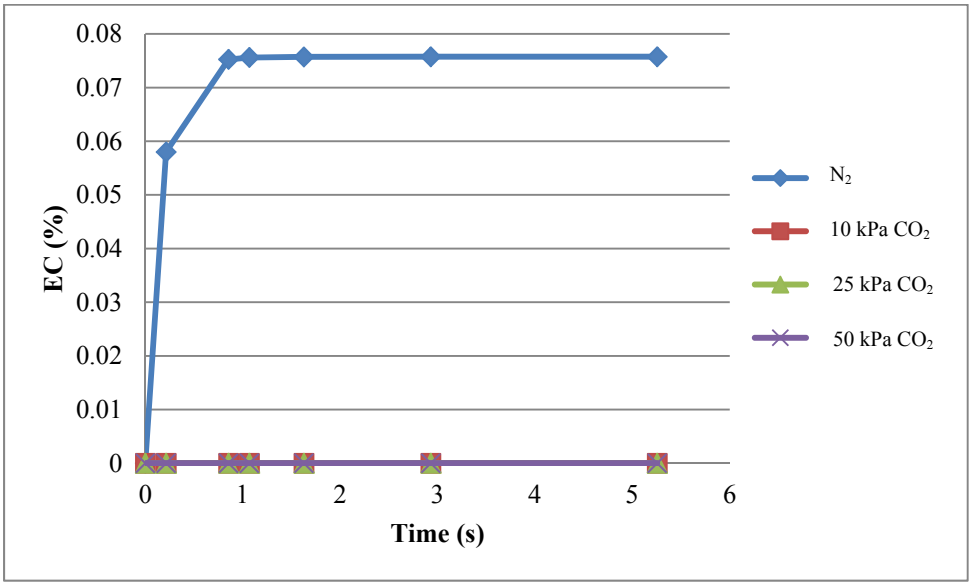

Figure 125. EC Prediction for Sample MSS-LS by NONISO T Model at T_1 = 1,050 K.

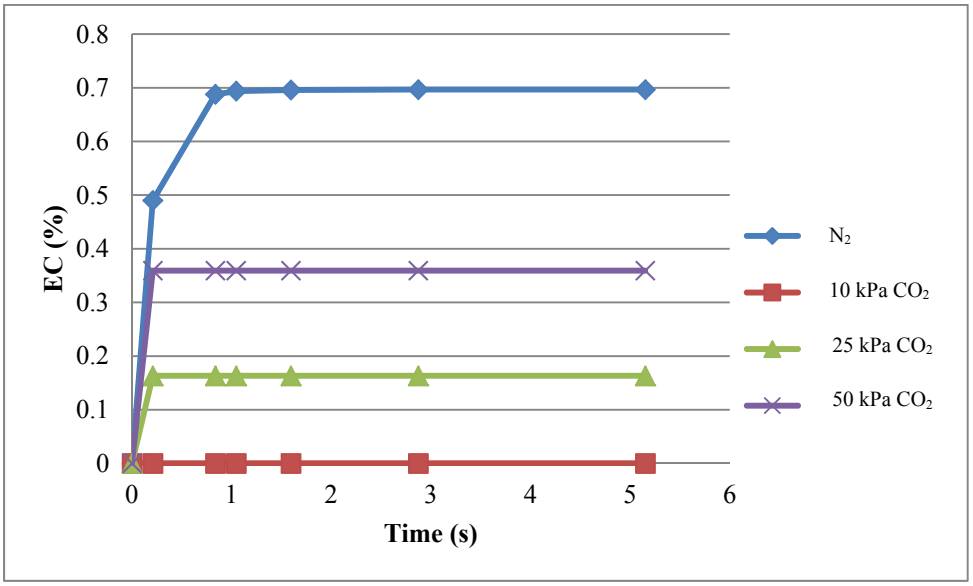

Figure 126. EC Prediction for Sample MSS-LS by NONISO T Model at T_1 = 1,120 K.

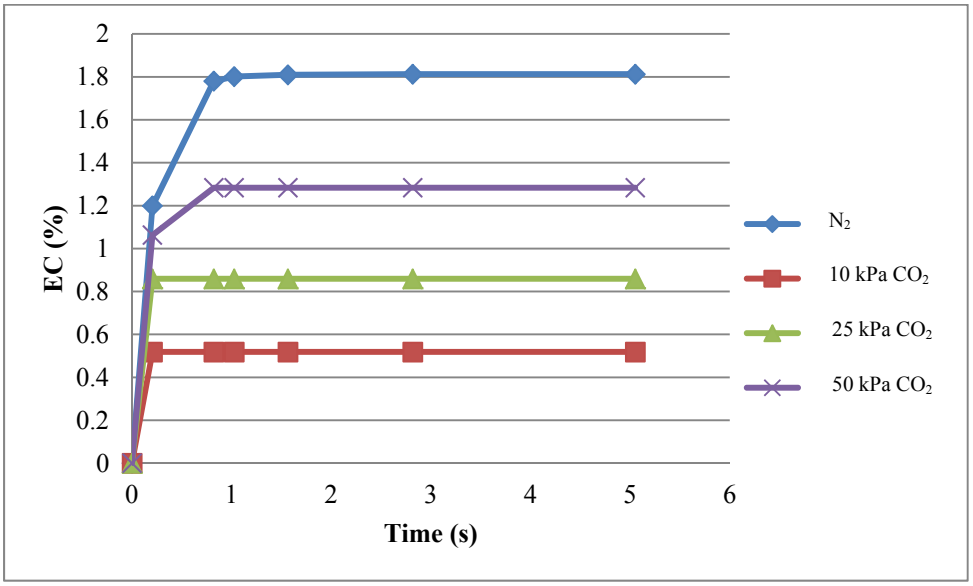

Figure 127. EC Prediction for Sample MSS-LS by NONISO T Model at T_1 = 1,180 K.

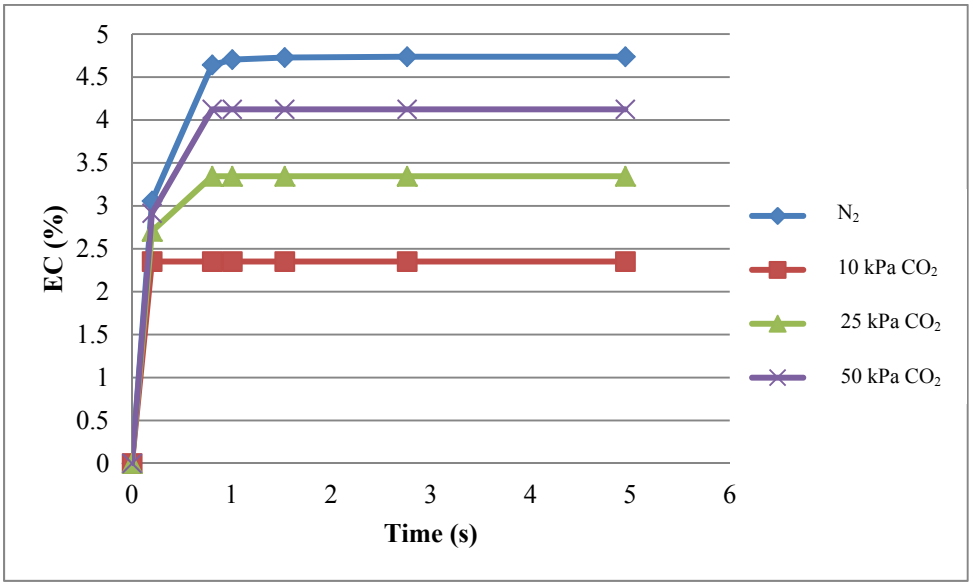

Figure 128. EC Prediction for Sample MSS-LS by NONISO T Model at T_1 = 1,250 K.

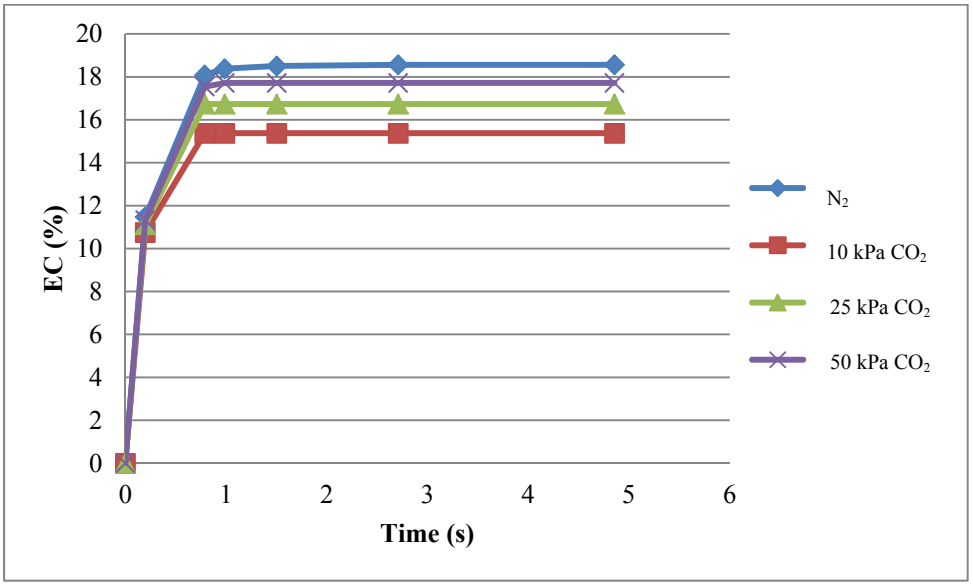

Figure 129. EC Prediction for Sample MSS-LS by NONISO T Model at T_1 = 1,350 K.

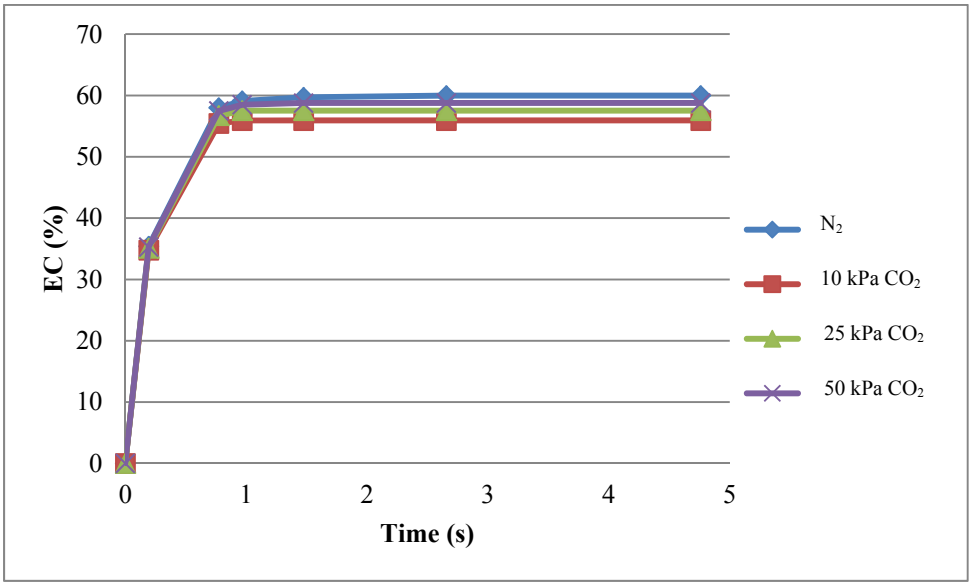

Figure 130 and Figure 131 present comparisons of the experimental SAP ECs with those predicted by the ISO T and NONISO T models at various temperatures, 5 seconds calcination time, and 0 and 10 kPa CO_2. ECs based on the two models present the maximum predicted values at the corresponding temperatures. Both models underestimated the observed experimental ECs at below 1,250 K and ISO T model overestimated the EC above 1,250 K. However, both models correctly predicted no conversions below 1,025 K, the thermodynamic calcination temperature for the thermal decomposition of the limestone in 10 kPa CO_2. Conversions in N_2 (0 kPa P_{CO_2}) are also small, confirming data shown in Figure 130 and Figure 131. The fact that both limestone decomposed at below 1,025 K (EC of about 45 % at 1,025 K) under the operating conditions of the SAP, is an indication that limestone particles were actually exposed to much higher temperatures than measured during the SAP experiments. As was discussed previously, temperature has the most impact on the rate of the calcination. Also, it was mentioned earlier that experimental conversion data were presented at temperatures measured at T_1 location where the where the gas temperatures were least 10 % lower than at the location where limestone was injected into SAP. However, even based on the temperatures at the injection port, thermodynamically, limestone decomposition should not have occurred. Based on the SAP results and the above discussion, it can conclude that the actual particle temperature was likely much higher than the measured gas temperatures at the injection and T_1 locations.

Radiation heat transfer both from the propane flame and walls of the SAP reactor could have contributed to the higher limestone particle temperature. The impact of thermal radiation on limestone particle temperature is not addressed in this work.

Additionally, as was described earlier, due to the size distribution of limestone particles, the residence times of the particles were non-uniform. Particles with shorter residence time than the residence time of the calcination gas will have shorter time to decompose. Since, the impact of particle size on the EC was not considered in the model, consequently, the experimental ECs would be higher than the model predictions.

Figure 130. Comparisons of Experimental and Modeled EC in SAP for Sample MRC-LS.

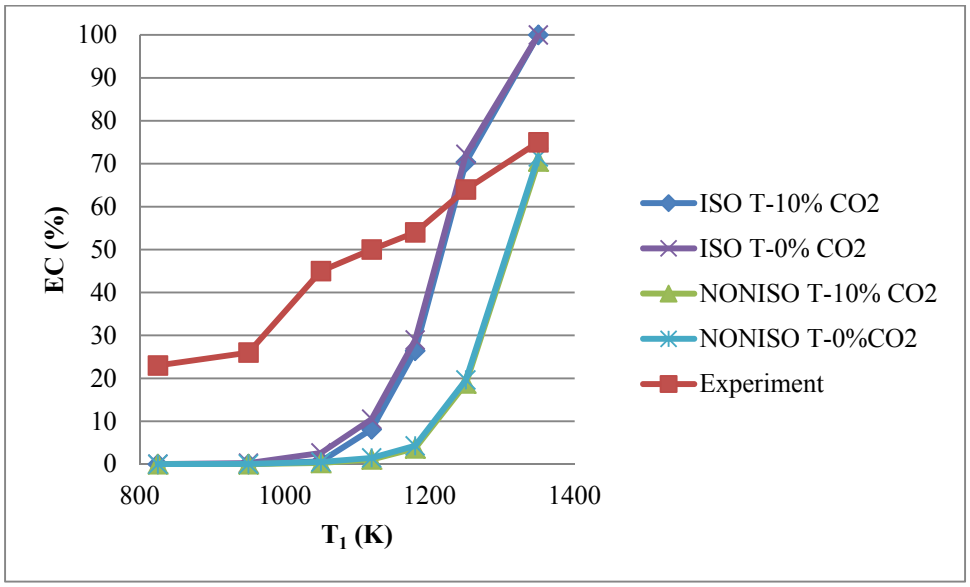

Figure 131. Comparisons of Experimental and Modeled EC in SAP for Sample MSS-LS.

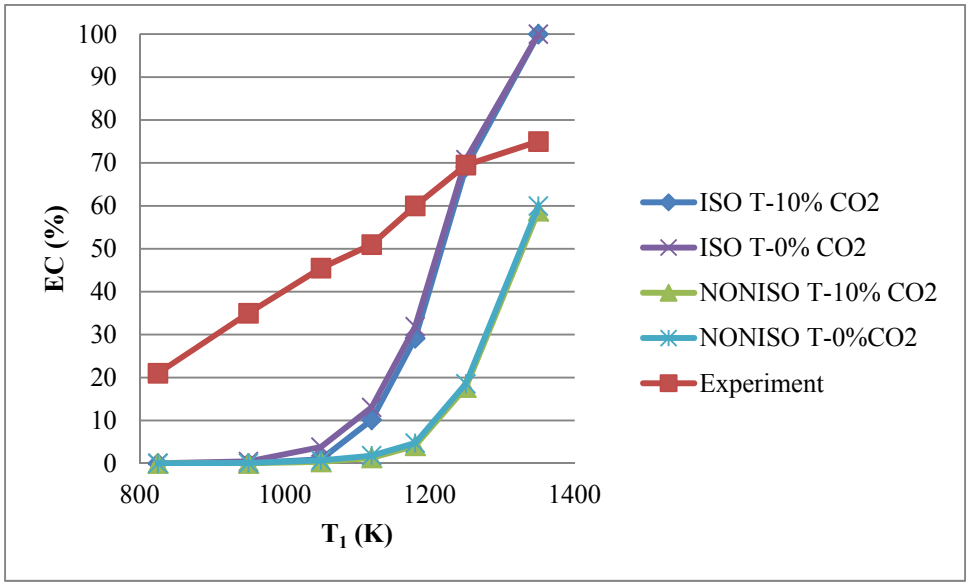

4 SUMMARY, CONCLUSIONS AND FUTURE WORK

In this work, limestone calcination in a Sorbent Activation Process (SAP) was studied. SAP, a patented technology, was developed by the Illinois State Geological Survey (ISGS), a division of the Prairie Research Institute at the University of Illinois at Urbana Champaign (UIUC) and Electric Power Research Institute (EPRI), Palo Alto, CA. SAP offers on-site production of environmental sorbents such as activated carbon or quicklime to remove air pollutants from flue gases of coal-fired power plants. SAP has successfully been demonstrated at pilot- and full-scale for production of activated carbon (AC) to remove vapor-phase mercury in coal combustion flue gas.

The focus of this research was to explore the technical feasibility of producing quicklime from thermal decomposition of limestone in a bench-scale SAP. The bench-scale SAP located at the Applied Research Laboratory of ISGS was used for this purpose. Pulverized limestone was injected in the entrained-flow reactor of the SAP at different operating conditions and the product quicklime was collected and characterized for extend of calcination and surface area. The average calcination time varied between 3 to 5 seconds. Kinetic information for thermal decomposition of limestone was obtained by non-isothermal thermogravimetric analysis method. Calcination data obtained at 2, 5, and 10 K/min linear heating rates in N_2 and in 10, 20, and 50 kPa CO_2 were analyzed by several kinetic analysis methods to determine the reaction order, activation energy and frequency factor at different test conditions. The kinetic information was used to predict limestone calcination in the SAP.

SAP experiments were performed using two limestone samples (sample MRC-LS and sample MSS-LS). Surface areas, extent of calcinations (ECs), and surface morphologies of quicklimes produced in the SAP were significantly impacted by temperature, residence time, and the composition of the calcination gas. Limestone calcination in the SAP occurred even at gas temperature below 1,025 K, the minimum thermodynamic temperature for thermal decomposition of limestone at 10 kPa CO_2. It was concluded that the temperature of limestone particles were higher than the gas temperature. Theoretically, a higher calcination temperature and a longer residence time should result in a higher EC. Results from SAP experiments; however, revealed that EC increased with increasing temperature field although increasing SAP temperature resulted in decreasing the residence time of limestone particles. Therefore, it was

concluded that temperature field in the SAP had a stronger impact on the EC than the particle residence time. Flash calcination in SAP suppressed the sintering effects, which causes a decrease in surface area of quicklime, during limestone calcination due to the short exposure time of limestone particle to the hot calcination gas. The highest total surface area was 12 m^2/g obtained from calcination of sample MRC-LS. The surface area of most commercial quicklime is < 2 m^2/g. The highest carbonate-free surface area of the lime products (normalized to its CaO content) was 37 m^2/g. EC and surface area development of limestone in SAP were independent of particle size for smaller than 45 μm particles for the test conditions used in this research.

Kinetic parameters of calcination of limestone are required to predict calcination behaviors in SAP. DTG-curve fitting (using DTG-SIM software), Coats-Redfern (CR), and Criado-Linearization methods were employed to determine the kinetic parameters of calcination of limestone samples using non-isothermal TGA data. Kinetic expressions developed using these kinetics analysis methods predicted limestone calcination in N_2 with a high accuracy (< 10 % deviation). However, the accuracy was low (up to 100 % deviation for Criado-Linearization method) when the same methods were applied to predict calcination of limestone in CO_2. Kinetic parameters generated using the CR-Linearization method had the smallest deviation (< 6 %) between the experimental and predicted TGA calcination data.

Kinetic parameters obtained by the DTG-curve-fitting method in N_2 were used to predict extent of calcination in the SAP. Two different models were developed, ISO T and NONISO T. ISO T assumes an isothermal temperature field in SAP and NONISO T uses the actual temperature field in SAP to predict EC. The impact of mass and heat transfer limitations and particle size distribution were not included in developing these models. The models were solely based on chemical reaction kinetics. Model predictions showed that increasing the calcination temperature diminishes the impact of CO_2 pressure on the calcination reaction. Both models underestimated the measured ECs in the SAP at below 1,250 K and the ISO T model overestimated the ECs above 1,250 K. However, both models correctly predicted no conversions below 1,025 K, the thermodynamic calcination temperature for the thermal decomposition of the limestone in 10 kPa CO_2.

Future work of this study should focus on : 1) installation of additional thermocouples to continuously monitor both axial and radial temperature profiles in the SAP, 2) an understanding

of the flow pattern and hydrodynamic inside the SAP to better estimate gas-gas and gas-solid mixing, 3) testing several size-graded limestone samples to evaluate the impact of particle size on limestone calcination, 4) calibrating the propane and combustion air flow rates to obtain more accurate readings, 5) quantify the extent of particle deposition in SAP, 6) measure gas phase concentrations of CO, CO_2, O_2, NO_x, and hydrocarbons (HCs), and verify those measured values, and 7) incorporate mass and heat transports effects in the model to better predict calcination performance of limestone in bench-, pilot-, and full-scale SAPs.

Appendix A

Equation 47 represents an unsteady-state conduction and convection heat transfer equation for heat transfer processes from a bulk gas to a single spherical limestone particle. In Equation 47, ρ (kg m^{-3}), C_p (J/kg K), k (kg m^{-1} K^{-1} s^{-3}), r (m), t (s), T (K) and Q_{rxn} (J) denote the density, heat capacity, conductive heat coefficient, radial location in the particle, time, temperature of the particle at location r, and the heat consumed/release due to chemical reaction. Radiation heat transfer by radiation is typically small compared to the convection and conduction heat transfer; was, therefore, not included in Equation 47 [Cengel, 2007]. Although limestone calcination is an endothermic reaction that acts as a heat sink, the heat consumed for decomposing limestone particles was neglected because the mass of limestone injected, and therefore the heat for thermal decomposition of the limestone, was small compared to the heat flux from the preheated SAP and the heat provided by burning the propane. α in Equation 48 represents the Fourier thermal diffusivity (m^2s^{-1}). The dependency of T to t and r in Equation 48 can be expressed as Equation 49, where f and g represent equations which are functions of r and t. Equation 50 is obtained when substituting Equation 49 in Equation 48, where λ is a separation constant. Equation 50 consists of two equations, Equation 51, more commonly known as Bessel Equation, and Equation 52. Equation 53 and Equation 54 are solutions of Equation 51, while Equation 55 and Equation 56 are solutions of Equation 52 for different values of λ. Upon substituting Equations 8 in Equation 49, Equation 57 is obtained, where A, B, C, and D are arbitrary coefficients which calculated using the initial and boundary conditions presented in Equation 58.

Equation 47:
$$\frac{\partial}{\partial r}\left(k\frac{\partial T}{\partial r}\right)+\frac{2\,k}{r}\left(\frac{\partial T}{\partial r}\right)=\rho Cp\frac{\partial T}{\partial t}+Q_{rxn}$$

Equation 48
$$\frac{\partial^2 T}{\partial r^2}+\frac{2}{r}\left(\frac{\partial T}{\partial r}\right)=\frac{\rho Cp}{k}\frac{\partial T}{\partial t}=\frac{1}{\alpha}\frac{\partial T}{\partial t}$$

Equation 49
$$T=f(r)\ g(t)$$

Equation 50 $$\frac{f''}{f} + \frac{2}{r}\frac{f'}{f} = \frac{g'}{\alpha g} = -\lambda$$

Equation 51 $$r^2 f''(r) + 2rf'(r) + \lambda r^2 f(r) = 0$$

Equation 52 $$g'(rt) + \alpha\lambda g(t) = 0$$

Equation 53 if $\sqrt{\lambda} \neq 0$ $$f(r) = \frac{1}{r}\sqrt{\frac{2}{\sqrt{\lambda}\pi}}\left(c_1 \sin\sqrt{\lambda}r + c_2 \cos\sqrt{\lambda}r\right)$$

Equation 54 if $\sqrt{\lambda} = 0$ $$f(r) = c_3 + c_4\frac{1}{r}$$

Equation 55 if $\sqrt{\lambda} \neq 0$ $$g(t) = c_5 e^{-\lambda\alpha t}$$

Equation 56 if $\sqrt{\lambda} = 0$ $$g(t) = c_6$$

Equation 57 $$T = \left(\frac{1}{r}\sqrt{\frac{2}{\sqrt{\lambda}\pi}}\right)\left(A \sin\sqrt{\lambda}r + B \cos\sqrt{\lambda}r\right) e^{-\lambda\alpha t} + \frac{C}{r} + D$$

The initial and boundary conditions for heat transfer process from the surrounding to the spherical limestone particle in SAP are described in Equation 58. From Equation 58b, the coefficient D in Equation 57 was found to be equal to T_1 (Equation 59). Coefficients B and C in Equation 57 have to be 0 for Equation 60 and Equation 58c to be valid. Zeroing B and C coefficients, Equation 57 and Equation 60 can be rewritten as Equation 62 and Equation 63. Substituting them in Equation 58d generates Equation 64 which upon rearranging results in Equation 65. Combining Equation 58a and Equation 62, the coefficient A is determined in Equation 66. Eventually, T in Equation 62 can be described as Equation 67 which can be used to calculate temperature T at any radial position and time in the limestone particle. Heisler charts in Figure 53 present solutions to Equation 22 in a graphical format [Heisler, 1947 and Geankoplis, 2003].

Initial and boundary conditions:

Equation 58: At $t = 0$ and $r > 0$, $T = T_o$ (a)

At $t = \infty$ and $r > 0$, $T = T_1$ (b)

At $t > 0$ and $r = 0$, $\frac{\partial T}{\partial r} = 0$

(c)

At $r = r_o$ $q = h\,(T - T_1)4\pi r^2 = -k\left(\frac{\partial T}{\partial r}\right)_{r=r_o} 4\pi r^2$ (d)

Equation 59 $D = T_1$

Equation 60 $\frac{\partial T}{\partial r} = \frac{1}{r^2}\sqrt{\frac{2}{\sqrt{\lambda}\pi}}e^{-\lambda\alpha t}\left[\left(A\sqrt{\lambda}r\cos\sqrt{\lambda}r - A\sin\sqrt{\lambda}r - B\sqrt{\lambda}r\sin\sqrt{\lambda}r - B\cos\sqrt{\lambda}r\right) - C\right]$

Equation 61 $B = C = 0$

Equation 62 $T = \left(\frac{1}{r}\sqrt{\frac{2}{\sqrt{\lambda}\pi}}\right)\left(A\sin\sqrt{\lambda}r\right)e^{-\lambda\alpha t} + T_1$

Equation 63 $\frac{\partial T}{\partial r} = \sqrt{\frac{2}{\sqrt{\lambda}\pi}}\left[\left(\frac{A\sqrt{\lambda}\cos\sqrt{\lambda}r}{r} - \frac{A\sin\sqrt{\lambda}r}{r^2}\right) - C\right]e^{-\lambda\alpha t}$

Equation 64 $h\left[\left(\frac{1}{r_o}\sqrt{\frac{2}{\sqrt{\lambda}\pi}}\right)\left(A\sin\sqrt{\lambda}r_o\right)e^{-\lambda\alpha t}\right] = -k\left(\sqrt{\frac{2}{\sqrt{\lambda}\pi}}\right)\left(\frac{A\sqrt{\lambda}\cos\sqrt{\lambda}r_o}{r_o} - \frac{A\sin\sqrt{\lambda}r_o}{{r_o}^2}\right)e^{-\lambda\alpha t}$

Equation 65 $\tan\sqrt{\lambda}r_o = \frac{\sqrt{\lambda}r_o k}{k - r_o h}$

Equation 66 $A = \frac{T_o - T_1}{\left(\frac{1}{r}\sqrt{\frac{2}{\sqrt{\lambda_n}\pi}}\right)\left(\sin\sqrt{\lambda_n}r\right)}$

Equation 67 $T = \left(\frac{1}{r}\sqrt{\frac{2}{\sqrt{\lambda}\pi}}\right)\left(\frac{T_o - T_1}{\left(\frac{1}{r}\sqrt{\frac{2}{\sqrt{\lambda_n}\pi}}\right)\left(\sin\sqrt{\lambda_n}r\right)}\sin\sqrt{\lambda}r\right)e^{-\lambda\alpha t} + T_1$

Heisler Charts (Figure 53) was used to determine the temperature gradient inside a limestone particle upon injection into the SAP reactor. In this chart, Bi, F_o, and θ^*_o are Biot number, dimensionless time and temperature expressions. Biot number represents a ratio of

convective to conductive heat transfer as expressed in Equation 68, where k_o, r_o, and h represent the heat conductivity (1.3W/m K) and radius of limestone particle (45 μm), and convective heat coefficient in the SAP reactor (W/m^2 K). F_o and α are described in Equation 69 and Equation 70, where ρ_o and Cp_o represent the density (2,700 kg/m^3) and heat capacity of limestone (840 J/kg K). θ_o^* is defined in Equation 71, where T_o, T_1, and T represent the initial temperature of the limestone particle (300 K), gas temperature in SAP, and temperature at the center of the limestone particle. Convective heat coefficient was calculated using the correlation for flow past a single sphere (Equation 72). In Equation 72, Re_p and Pr represent Reynolds number for limestone particle (Equation 73) and Prandtl number (Equation 74), where ρ, k, μ, and C_p represent the density, thermal conductivity, viscosity, heat capacity of the gas, while D_o represents the diameter of the limestone particle (80 μm). CHEMCAD was used to determine the properties of flue gas based on stoichiometric propane combustion. The properties of gas were evaluated at T_f which represents the average temperature between bulk gas and limestone particle temperature initially as defined in Equation 75.

Equation 68 $$\mathbf{Bi} = \frac{\mathbf{h.r_o}}{\mathbf{k_o}}$$

Equation 69 $$\mathbf{F_o} = \frac{\boldsymbol{\alpha}\,\mathbf{t}}{\mathbf{r_o}^2}$$

Equation 70 $$\boldsymbol{\alpha} = \frac{\mathbf{k_o}}{\boldsymbol{\rho_o}\,\mathbf{Cp_o}}$$

Equation 71 $$\boldsymbol{\theta_o}^* = \frac{\mathbf{T_1 - T}}{\mathbf{T_1 - T_o}}$$

Equation 72 $$\mathbf{Nu} = \frac{\mathbf{h\,D_o}}{\mathbf{K}} = \mathbf{2 + 0.6\,Re_p}^{\mathbf{0.5}}\,\mathbf{Pr}^{\mathbf{0.33}}$$

Equation 73 $$\mathbf{Re_p} = \frac{\boldsymbol{\rho}\,\mathbf{u}\,\mathbf{D_o}}{\boldsymbol{\mu}}$$

Equation 74 $$\mathbf{Pr} = \frac{\boldsymbol{\mu}.\mathbf{Cp}}{\mathbf{k}}$$

Equation 75 $$\mathbf{T_f} = \frac{\mathbf{T_1 + T_o}}{\mathbf{2}}$$

REFERENCES

Adolfsson, E, Nygren, M, and Hermansson, L. Decomposition mechanisms in aluminum oxide apatite systems." *Journal of American the Ceramic Society* 82, 2909-2912 (1999).

Ar, I. Calcination kinetics of high purity limestones. *Chemical Engineering Journal* 83, 131-137 (2001).

Avila, I, Crnkovic, P.M., Milioli, F. E., and Luo, K.H. Thermal decomposition kinetics of Brazilian limestones: effect of CO_2 partial pressure. *Environmental Technology* 1, 1-8 (2011).

Baker, E.H. The calcium oxide – carbon dioxide system in the pressure range 1 – 300 atmospheres. *Journal of the Chemical Society* 0, 464 – 470 (1962).

Benson, L.B., Smith, K. J., Roden, R. A., Loch, E., Potts, J. Control of Sulfur Dioxide and Sulfur Trioxide Using By-Product of a Magnesium-Enhanced Lime FGD System. paper presented at the Institute of Clean Air Company ICAC Forum 2003: Multi-Pollutant Emission Control & Strategies, Nashville, TN (2003).

Beruto, D. and Searcy, A.W. Use of the Langmuir method for kinetic studies of decomposition reactions: calcite ($CaCO_3$). *Journal of the Chemical Society Faraday Transactions 1* 70, 2145 (1974).

Biarnes, M. "Combustion." E-Instrument. Web. (accessed April, 2012). <http://www.e-inst.com/docs/E-Instruments-Combustion-Booklet-2009.pdf>.

Borgwardt, R.H. Kinetics of the reaction of sulfur dioxide with calcined limestone. *Environmental Science & Technology* 4, 59-63 (1970).

Borgwardt, R.H. and Harvey, R.D. Properties of carbonate rocks related to sulfur dioxide reactivity. *Environmental Science & Technology* 6, 350-360 (1972).

Borgwardt, R.H. Calcination kinetics and surface area of dispersed limestone particles. *American Institute of Chemical Engineers Journal* 31, 103-111 (1985).

Borgwardt, R.H. and Bruce, K.R. Effect of specific surface area on the reactivity of CaO with SO_2. *American Institute of Chemical Engineers Journal* 32, 239-246 (1986).

Borgwardt, R.H. Sintering of nascent calcium oxide. *Chemical Engineering Science* 44, 53-60 (1989).

Borgwardt, R.H. Calcium oxide sintering in atmospheres containing water and carbon dioxide. *Industrial & Engineering Chemistry Research* 28, 493-500 (1989).

Boynton, R. S. Chemistry and Technology of Lime and Limestone. John Wiley & Sons. ISBN 0-471-02771-5 (1980).

British Lime Association. "How a Kiln Works." Web. (accessed June, 2011). <http://www.britishlime.org/edu_kiln01.php>.

Campbell, F.R., Hills, A.W.D. and Paulin, A. Transport properties of porous lime and their influence on the decomposition of porous compacts of calcium carbonate. *Chemical Engineering and Science*, 25 929–942 (1970).

Campbell, J.H. Kinetics of Decomposition of Colorado Oil Shale: II. Carbonate Minerals. Lawrence Livermore National: Livermore, CA. UCRL-52089 2, 53 (1978).

Cengel, Y.A. Heat and Mass Transfer: A Practical Approach. McGraw-Hill. ISBN 0-071-52739-X (2007).

Chan, R. K., Murthi, K. S., and Harrison, D. Thermogravimetric analysis of Ontario limestones and dolomites. 11. reactivity of sulfur dioxide with calcined samples. *Canadian Journal of Chemical Engineering,* 48 2979 (1970).

Chang, R, Rostam-Abadi, M., and Chen, S. Apparatus and Method for Removal of Vapor Phase Contaminants from a Gas Stream by In-situ Activation of Carbon-based Sorbents. Electric Power Research Institute, Inc. (Palo Alto, CA), assignee. Patent 6,451,094 (2002).

Chang, R, Rostam-Abadi, M., and Sjostrom, S. Method for Removal of Vapor Phase Contaminants from a Gas Stream by In-situ Activation of Carbon-based Sorbents.

Electric Power Research Institute, Inc. (Palo Alto, CA), assignee. Patent 6,558,454 (2003).

Chang, R., Lu, Y., and Rostam-Abadi, M. Method and Apparatus for On-Site Production of Lime and Sorbents for Use in Removal of Gaseous Pollutants. Electric Power Research Institute, Inc. (Palo Alto, CA), assignee. Patent 20,110,223,088 (2011).

Chen, X. "Impacts of Fly Ash Composition and Flue Gas Components on Mercury Speciation." Diss. University of Pittsburgh. 2007. Web. (accessed March, 2012) <http://d-scholarship.pitt.edu/8590/1/ChenX_ETD_2007.pdf. >

Cheng, C. and Specht, E. Reaction rate coefficients in decomposition of lumpy limestone of different origin. *Thermochimica Acta* 449, 8-15 (2006).

Cooper, D. C. and Alley, F. C. Air Pollution Control: A Design Approach. 3rd ed. Waveland Press, Inc (2002).

Criado, J.M., Gonzalez, M., Tlek, J. M., and Ortega, A. The effect of the CO_2 pressure on the thermal decomposition kinetics of calcium carbonate. *Thermochimica Acta* 254, 121-127 (1995).

Daoudi, M. and Walters, J. K. The reaction of HCl gas with calcined commercial limestone Particles: the effect of particle size. *Journal of Chemical Engineering* 47, 11-16 (1991).

Energy Information Administration (EIA). US Coal Reserves: An Update by Heat and Sulfur Content. U.S. Department of Energy. Washington: DOE/EIA-0529(92) (1993).

Elder, J. P. and Reddy, V. B. The Kinetics of the Thermal Degradation of Calcium Carbonate. *Journal of Thermal Analysis* 31, 395-405 (1986).

Electric Power Research Institute (EPRI). "On-Site Sorbent Activation for Mercury Control at Coal-Fired Power Plants." Web. (accessed May, 2010). <http://mydocs.epri.com/docs/TI/1021633_Sorbent%20Activation_v3.pdf>.

Everson, R.C., Neomagus, H.W.J.P., and Njapha, D. Kinetic analysis of non-isothermal thermogravimetric analyser results using a new method for the evaluation of the temperature integral and multi-heating rates. *Fuel* 85, 418-422 (2006).

Feeley III, T.J., et al. An update on DoE's phase II and phase III mercury control technology R&D program. *Fuel Processing Technology* 90, 1388-1391 (2009).

Fluke. "Fluke 50 Series II Thermometers." Web. (accessed January, 2012). <http://www.fluke.com/fluke/usen/electrical-test-tools/thermometers/fluke-50-series-ii.htm?PID=56085>.

Fonseca, A.M., Órafäo, J.J., and Salcedo, R.L. A new approach to the kinetic modeling of the reaction of gaseous HCl with solid lime at low temperature. *Chem. Eng. Science* 58, 3499–3506 (2003).

Fonseca, A.M., Órafäo, J.J., and Salcedo, R.L. Kinetic modeling of the reaction of HCl and solid lime at low temperatures. *Ind. Eng. Chem. Res* 37, 4570–4576 (1998).

Fuertes, A. B., Alvarez, D., Rubiera, F., Pis, J. J., and Marban, G. Simultaneous calcination and sintering model for limestone particles decomposition. *Transactions of the Institution of Chemical Engineers*, 71A, 69–76 (1993).

Geankoplis, C. J. Transport Processes and Separation Process Principles: (Includes Unit Operations). 4th ed. New Delhi: Prentice Hall of India, 373-74 (2003).

German, R.M. and Munir, Z.A. Surface area reduction during isothermal sintering. *Journal of the American Ceramic Society* 59, 379–383 (1976).

GXT, Inc. "FERRET 16 Emissions Analyzer." Web. (Apr, 2012). <http://www.gxtauto.com/uploads/16-Flyer.pdf>.

Hartman, M., Pata. J., and Coughlin, R. W. Influence of porosity of calcium carbonates on their reactivity with sulfur dioxide. *Industrial & Engineering Chemistry Process Design and Development* 17, 411-419 (1978).

Hartman, M. and Trnka, O. Reactions between calcium oxide and flue gas containing sulfur dioxide at lower temperatures. *American Institute of Chemical Engineers Journal* 39, 615-624 (1993).

Heisler, M. P. Temperature charts for induction and constant temperature heating, *Trans. ASME* 69, 227–236, (1947).

Hills, A.W.D. The mechanism of the thermal decomposition of calcium carbonate. *Chemical Engineering Science* 23, 297-320 (1968).

Hoffmann, J., and Ratafia-Brown, J. Preliminary cost estimate of activated carbon injection for controlling mercury emissions from an un-scrubbed 500 MW coal-fired power plant. final report for DoE - National Energy Technology Laboratory - Innovations for Existing Plant Program. (2003).

HORIBA. "Compact Laser Diffraction Particle Size Analyzer LA-300." Web. (accessed June, 2011). <http://www.horiba.com/us/en/scientific/products/particle-characterization/particle-size-analysis/details/la-300-110/>.

Hsi, H.C., Rood, M.J., Rostam-Abadi, M., Chen, S., and Chang, R. Effects of sulfur impregnation temperature on the properties and mercury adsorption capacities of activated carbon fibers (ACFs). *Environmental Science & Technology* 35, 2785-2791 (2001).

Hu, N. and Scaroni, A.W. Calcination of pulverized limestone particles under furnace injection conditions. *Fuel* 75, 177-186 (1996).

Hyatt, E.P., Cutler, I.B., and Wadsworth, M.E. Calcium carbonate decomposition in carbon dioxide atmosphere. *Journal of American the Ceramic Society* 41, 70–74 (1958).

Ingraham, T.R. and Marier, P. Kinetic studies on the thermal decomposition of calcium carbonate. *Canadian Journal of Chemical Engineering* 41, 170–173 (1963).

Irabien, A., Cortabitarte, F., and Ortiz, M. I. Kinetics of Flue Gas Desulfurization at Low Temperatures: Nonideal Surface Adsorption Model. *Chemical Engineering and Science* 47, 1533 (1992).

Keener, S. and Kuang, S.J. Structural pore development model for calcination. *Chemical Engineering Communications* 117, 279-291 (1992).

Khinast, J., Brunner, C., Aichinger, G., and Staudinger, G. Reaction during Low Temperature Dry Flue Gas Desulfurization. paper presented at the 15th SO_2 Control Symposium (1995).

Khinast, J., Krammer, G., and Brunner, C. Decomposition of limestone: the influence of CO_2 and particle size on the reaction rate. *Chemical Engineering* 51, 623-634 (1996).

Kidde. "Carbon Monoxide Alarms and Combo Alarms AC Plug-in Operated : Model KN-COPP-3." Web. (accessed April, 2012). <http://www.kidde.com/utcfs/Templates/Pages/Template53/0,8062,pageId%3D4428%26siteId%3D384,00.html>.

Klingspor, J., Karlsson, H. T., and Bjerle, I. A kinetic study of the dry SO_2-limestone reaction at low temperature. *Chemical Engineering Communications* 22, 81-103 (1983).

Kocaefe, D., Karman, D., Steward, F. R. Comparison of the sulfation rates of calcium, magnesium and zinc oxides with SO_2 and SO_3. *Canadian Journal of Chemical Engineering* 63, 971-977 (1985).

Lee, S.F., Seo, Y.C., Jongsoo, J., and Lee, T.G. Removal of gas-phase elemental mercury by iodine- and chlorine-impregnated activated carbons. *Atmospheric Environment* 38, 4887-4893 (2004).

Lee S.H. and Park Y.O. Gas-phase mercury removal by carbon-based sorbents. *Fuel Processing Technology* 84, 197–206 (2003).

Likens, G. “Acid Rain". Encyclopedia of Earth. Web. (accessed December, 2010). <http://www.eoearth.org/article/Acid_rain?topic=49506>.

Liu, C. F. and Shih, S. M. Kinetics of the reaction of hydrated lime with SO_2 at low temperatures: effects of the presence of CO_2, O_2, and NO_x. *Industrial & Engineering Chemistry Research* 47 (2008).

Milne, C.R., Silcox, G.D., Pershing, D.W., and Kirchgessner, D.A. Calcination and sintering models for application to high-temperature, short-time sulfation of calcium-based sorbents. *Industrial & Engineering Chemistry Research* 29, 139-149 (1990).

Quantachrome. "Monosorb B.E.T Surface Area Analyzer." Web. (accessed May, 2011). <http://www.quantachrome.com/gassorption/monosorb.html>.

Morris, L. “Acid Gas Emission Control Measures.” Web. (accessed June, 2011). <http://www.pennenergy.com/index/power/display/9915040467/articles/power-engineering/volume-114/issue-10/features/acid-gas-emission-control-measures.html>.

Morrison, A. F. Data correlation for drag coefficient for sphere. Department of Chemical Engineering, Michigan Technological University, Houghton, MI. 2010. (accessed April, 2012). <www.chem.mtu.edu/~fmorriso/DataCorrelationForSphereDrag2010.pdf>

Oates, J. A. H. Lime and Limestone: Chemistry and Technology, Poduction and Uses. Weinheim: Wiley-VCH (1998).

Ohme, K., Schrader, R. and Müller, A. Kinetik der thermischen dissoziation von kalkstein und zementrohmehl im flugstaubreaktor. *Silikattechnik* 26, 403–407 (1975).

Powell, E. K. and Searcy, A. W. Surface areas and morphologies of CaO produced by decomposition of large $CaCO_3$ crystals in vacuum. *Communications of the American Ceramic Society* 42-44 (1982).

Rochelle, G. Reaction of Hydrated Lime with SO_2 in Humidified Flue Gas. paper presented at SO_2 Control Symposium EPA/EPRI, New Orleans, LA (1990).

Schenelle, K.B. and Brown, C.A. Air Pollution Control Technology Handbook. CRC Press LLC. Boca Raton, FL (2002).

Schenck. “AccuRate Dry Material Feeder." Web. (accessed March, 2012). <http://www.genemco.com/catalog/pdf/SNSL272accuratefeeder.pdf>.

SIGRIST. "Isokinetic Sample." *SIGRIST Process Photometer*. Web. (accessed April, 2012). <http://www.photometer.com/en/abc/show.html?q=Isokinetic%20sample>.

Silcox, G.D., Kramlich, J.C., and Pershing, D.W. A mathematical model for the flash calcination of dispersed calcium carbonate and calcium hydroxide particles. *Industrial & Engineering Chemistry Research* 28, 155-160 (1989).

Singh, N. B., and Singh, N. P. Formation of CaO from thermal decomposition of calcium carbonate in the presence of carboxylic acids. *Journal of Thermal Analysis and Calorimetry* 89, 159-62 (2007).

Sjostrom S., Wilson, C., Bustard, J., Spitznogle, G., Toole, A., O'Palko, A., Chang, R. Full-scale Evaluation of Carbon Injection for Mercury Control at a Unit Firing High Sulfur Coal. ADA-ES, Inc – American Electric Power Corporation – DoE – EPRI. paper presented at USEPA – DoE – EPRI Combined Power Plant Air Pollutant Control Symposium: The MEGA Symposium. Baltimore, Maryland (2006).

Smith, D. "SO_2 Controls: Cost of Scrubbers Down to $100/kW". Power Engineering. 2001. Web. (accessed April, 2012). <http://www.power-eng.com/articles/print/volume-105/issue-9/features/sosub2-sub-controls-cost-of-sosub2-sub-scrubbers-down-to-100-kw.html>

Thermo Scientific. "Thermo Scientific TGA VersaTherm Analyzer." Web. (accessed March, 2012). <http://www.reoterm.com.br/central/Analise_Termica/VersaTherm%20TGA.pdf>.

Thibault, J. D., Steward, F. R., and Ruthven, D. M. The kinetics of absorption of SO_3 in calcium and magnesium oxides." *Canadian Journal of Chemical Engineering* 60, 796-801 (1982).

Thompson, J.L. Prediction lime burning rate via new dynamic calcination theory. *Pit and Quarry* 5 (1979).

USEPA. "Mercury and Air Toxics Standards (MATS) for Power Plants." Web (accessed March, 2012a). <http://www.epa.gov/mats/basic.html>.

USEPA. "Air Pollution Control Technology Fact Sheet." Publication no. EPA-452/F-03-034. Web (accessed March, 2012b). <http://www.epa.gov/ttncatc1/dir1/ffdg.pdf>.

USEPA. "Health Effects of Mercury." Web (accessed March, 2012c). <http://www.epa.gov/hg/effects.htm>.

Wark, K., Warner, C.F., and Davis, W.T. Air Pollution: Its Origin and Control. Addison-Wesley. Menlo Park, CA (1998).

Yan, R., Chin, T., Liang, D. T., Laursen, K., Ong, W. Y., Yao, K., and Tay, J. H. Kinetic study of hydrated lime reaction with HCl. *Environmental Science & Technology* 37, 2556-2562 (2003).

Yang, J., Miranda. R., and Roy, C. Using the DTG curve fitting method to determine the apparent kinetic parameters of thermal decomposition of polymers. *Polymer Degradation and Stability* 73, 455-461 (2001).

Yu, H. D., Zhang, Z. Y., Win, K. Y., and Chan, J. Bioinspired fabrication of 3D hierarchical porous nanomicrostructures of calcium carbonate for bone regeneration. *Chemical Communications* 46, 6578-6580 (2010).

Zhuang, Y., Olson, E., and Galbreath, K. Mercury transformations in coal combustion flue gas. *Fuel Processing Technology* 65-66, 289-310 (2000).

Zhuang, Y., Martin, C., Pavlish, J., and Botha, F. Cobenefit of SO_3 reduction on mercury capture with activated carbon in coal flue gas. *Fuel* 90, 2998-3006 (2011).

Zhong, Q. and Bjerle, I. Calcination kinetics of limestone of nascent CaO. *Thermochimica Acta* 223, 109-120 (1993).